Master thesis : Tip leakage flow in high pressure turbines

Auteur : Liu, Yu
Promoteur(s) : Terrapon, Vincent
Faculté : Faculté des Sciences appliquées
Diplôme : Master en ingénieur civil en aérospatiale, à finalité spécialisée en "aerospace engineering"
Année académique : 2016-2017
URI/URL : http://hdl.handle.net/2268.2/3691

Faculty of Applied Sciences
University of Liège
Belgium

School of Energy and Power Engineering
Beihang University
P.R.China

MASTER THESIS

Numerical Investigation of Heat Transfer and Tip Leakage Flow in High Pressure Turbines

---

ULiège Supervisor : Prof. V. TERRAPON
Beihang Supervisor : Prof. Z.P. ZOU

Yu Min LIU

Master in Aerospace Engineering

Academic year 2016 - 2017

August 21, 2017

Foreword

The realization of this work which required four and half months of intensive labour was accomplished during my internship in the university of Beihang. Beside the large amount of simulations that were performed, a large range of tasks was covered. Notably, manipulation of CAD tools for modification of the blade geometry, generation of a well conditioned grid, definition of a well-posed configuration for the simulation and post-processing of the numerical results.

Meanwhile, lots of encounters were made, friendships were forged and great moments were shared. I was able to make most of this opportunity and I am very thankful to the people who made this fruitful experience possible.

That is the very reason why I want to dedicate the first part of this work to the people who have helped and supported me during my stay in Beihang university. From my perspective, it is a great opportunity and at the same time the least I can do to show my gratitude towards them.

Firstly, I am very thankful to Pr. Terrapon and Pr. Bechet for their recommendation and consecutively the opportunity they offered me to carry out my master thesis in a new environment.

Next, I want to thank Pr. Zou (邹正平老师）for welcoming me in his great research team.

Then, I want to show my gratitude to the Ph.D. assistant Shao (邵飞）for all the technical support he was able to offer during the realization of this work.

Lastly, I want to address special thanks to my parents for supporting me during the entire stay in China,

to my research colleagues and wonderful friends Li Chao （李超）, Cheng ZhengQu (程正渠）, Huang Lin (黄霖), He XiaoJuan (贺晓娟),

to my exceptional friends of the Beihang student international department Yu LingXiao (余凌霄）, Li XiaoDong (李晓东),

to my close friends Zhang JinFeng (多多), Yan BaoBao (燕宝宝）, Nora Folon, Argjin Gashi, Philippe Sadzot,

to the moon lady Sha Jing (沙静）.

"Le vent se lève, il faut tenter de vivre."

— P. Valéry

I will surely carry these precious memories until the end.

Abstract

In the framework of this master thesis, a numerical study has been carried out in order to investigate the effect of tip geometry on the tip leakage flow and heat transfer features in a unshrouded high pressure axial flow turbine stage designed by Erhard [10]. Four different tip profiles were considered, namely a default flat tip, a modified flat tip, a modified double squealer tip and a modified double thin squealer tip. The performances of the distinct tip profiles were compared to determine the improvement in terms of leakage mass flow rate and heat transfer. The computations were carried out on a single rotor blade with periodic boundary conditions. Grid independence study was performed in order to determine the adequate mesh to employ for the computations. Turbulence was modelled with the BSL-RSM model because it provides more advantages than its SST counterpart model. At the end, it was proven that adoption of a cavity can drastically enhance the aerothermal performances, that is, providing a decrease in the leakage loss and average heat transfer over the tip.

Contents

List of Figures

List of Tables

Nomenclature

A	Area [m^2]
$\mathbf{AVR}$	Axial velocity ratio (outlet/inlet) [-]
c	Reference true chord [m]
c_z	Axial chord [m]
C_f	Skin friction coefficient [-]
C_p	Pressure coefficient [-]
c_p	Isobaric specific heat capacity [J/kg.K]
c_v	Isochoric specific heat capacity [J/kg.K]
D	Reference diameter of the rotor [m]
E	Absolute error of a quantity of interest [-]
f	Random quantity of interest [-]
h	Enthalpy [J/kg]
h_c	Heat transfer coefficient [W/m^2.K]
I_t	Rothalpy [J/kg]
k	Fluid thermal conductivity [W/m.K]
k'	Turbulent kinetic energy [m^2/s^2]
k_t	Turbulent thermal conductivity [W/m.K]
L	Reference length [m]
$\dot{m}$	Mass flow rate [kg/s]
M	Mach number [-]
p	Pressure [Pa]
P_w	Output power [W]
q	Heat flux [W/m^2]
q_t	Turbulent heat flux [W/m^2]
Q	Heat [W]
R	=8.314, Ideal gas constant [J/mol.K]
R_c	Degree of reaction [-]
T	Temperature [K]
T_w	Torque [N.m]
u_i	Velocity vector in the absolute frame [m]
$\mathbf{U}$	Blade rotation speed (vector) [m/s]
U	Blade rotation speed (norm) [m/s]
$\mathbf{V}$	Absolute velocity (vector) [m/s]
V	Absolute velocity (norm) [m/s]
w_i	Velocity vector in the rotating frame [m]
$\mathbf{W}$	Relative velocity (vector) [m/s]
W	Relative velocity (norm) [m/s]

Y	Tip leakage loss [W]
y	Wall distance [m]
y^+	Non-dimensional wall distance [-]
n	Normal component to a surface [m]
x, y, z	Cartesian coordinates [m]
$\mathbf{e}_x$, $\mathbf{e}_y$, $\mathbf{e}_z$	Cartesian frame unit vectors [-]
z, θ, r	Cylindrical coordinates [m] and [rad]
$\mathbf{e}_z$, $\mathbf{e}_\theta$, $\mathbf{e}_r$	Cylindrical frame unit vectors [-]
α	Absolute flow angle [rad]
β	Relative flow angle [rad]
γ	=1.4, Ideal gas constant [-]
η_t	Isentropic efficiency [-]
ϕ	Flow coefficient [-]
ψ	Loading coefficient [-]
ρ	Density of the fluid [kg/m^3]
τ_{ij}	Shear stress tensor [N/m^2]
θ_T	Non-dimensional temperature [-]
μ	Dynamic viscosity of the fluid [Pa.s]
μ_t	Turbulent dynamic viscosity [Pa.s]
ν	Kinematic viscosity of the fluid [m^2/s]
Ω	Blade angular velocity [rad/s]
Ω_i	Blade angular velocity vector [rad/s]
ω'	Specific dissipation rate [rad/s]
Nu	Nusselt number [-]
Re	Reynolds number [-]
Pr	Prandtl number [-]
Pr_t	Turbulent Prandtl number [-]
St	Stanton number [-]

Subscript

$\perp$	Perpendicular
e	Free stream
l	Leakage
p	Pressure side
t	Total
s	Suction side
w	Wall
0, 1, 2, 3	Station indices, vane inlet, blade inlet, blade outlet, blade far outlet

A, B, C	Station indices, vane inlet, blade inlet, blade outlet
is	Isentropic
ad	Adiabatic
av	Average
ex	Exit of the gap
ng	Without gap
bsl	Baseline

Acronym

CFD	Computational fluid dynamics
SST	Shear stress model
BSL-RSM	Baseline Reynolds stress model

1 Introduction

Modern gas engines are designed to operate at extreme conditions in order to deliver the required thrust and power defined by the user. Consecutively, the understanding of internal flow within each component of the engine reveals to be crucial for the designer in charge. For this work, the interest is focused on the flow within a single high pressure turbine stage, more precisely on the performance of this turbine stage. All the necessary data about this turbine stage is found in the work of Erhard [10]. Now, the objective of this work is to carry out a performance analysis by the means of numerical simulation even though experiments are also required and provide a solution that can improve the performance of the turbine stage. Nevertheless, it has been proven that a great part of the loss encountered in turbine flows comes from the tip leakage flow. Consequently, the attention is mainly given to the tip leakage flow and alternatives will be formulated later on to prevent the tip leakage losses.

There are two different aspects about the tip leakage flow. First, if the flow that passes through the tip gap is not properly turned, then there will be reduction in output work. Second, the tip leakage vortex formed at the gap exit will inevitably mix with the main flow, that causes generation of entropy, that is, a loss within the blade passage but within the gap as well. Apart from these losses, the acceleration of the hot incoming flow at the entrance of the tip gap is followed by separation and re-attachment regions, that result in high heat transfer on the tip. In general, modern blades include cooling holes placed at the tip to prevent large heat transfer. The design of the cooling systems is beyond the scope of this work.

Since experimental results are not available for comparison in this context, one has to refer existent researches to carry out a qualitative comparison of the numerical results. For example, Bunker [12, 15] has provided methods to quantify losses and heat transfer related to tip clearance flow. Lee et al. [11] measured experimentally the mass flow rate and heat transfer on the blade tips using naphthalene technique. The purpose of its work is to determine the effects of clearance gap, Reynolds number and inlet turbulence intensity. Kwak, Han [21, 22] and Booth [18] have carried a similar experiment by using transient liquid crystal technique. In recent years, three dimensional numerical simulation for this type of flow has become more and more common. It implies that this numerical tool has become reliable and suitable for this complex flow. Yang et al. [23] have tested the numerical simulation for the study of tip leakage flow and heat transfer over a turbine blade for three different tip configurations. Yang et al. [39] have carried out similar numerical simulations but they have emphasized the effect of Coriolis forces on the tip leakage flow. Bunker et al. [14] have numerically investigated the impact of the squealer tip profile on the tip leakage flow and heat transfer distribution. Mumic et al. [42] have conducted an investigation over the aerothermal performance of the flat and cavity tip profiles for three different clearances. Regardless of both tip profiles, the averaged heat transfer over the tip and the leakage mass flow rate increased with the clearance. Additionally, the average heat transfer for the cavity tip profile is lower than that of the flat tip profile.

The numerical investigation conducted for this work will be based on the procedure adopted by these research papers. The default laboratory turbine blade is implemented in the computational domain and the optimal operating condition is assigned to the simulation. Once analysis of the flow and heat transfer mechanisms have thoroughly been reviewed and understood, improvement of aerothermal performance will successively be proposed. The improvement includes an alternative flat tip profile, a double squealer tip profile and a double thin squealer tip profile.

2 Axial Turbine Flow

In many modern applications that require propulsion or energy conversion systems, turbomachinery devices remain the main trend that can fulfill these specific requirements. By all means, different types of turbomachines have been developed throughout the years and have been classified according to their function and to the path taken by the flow throughout the device.

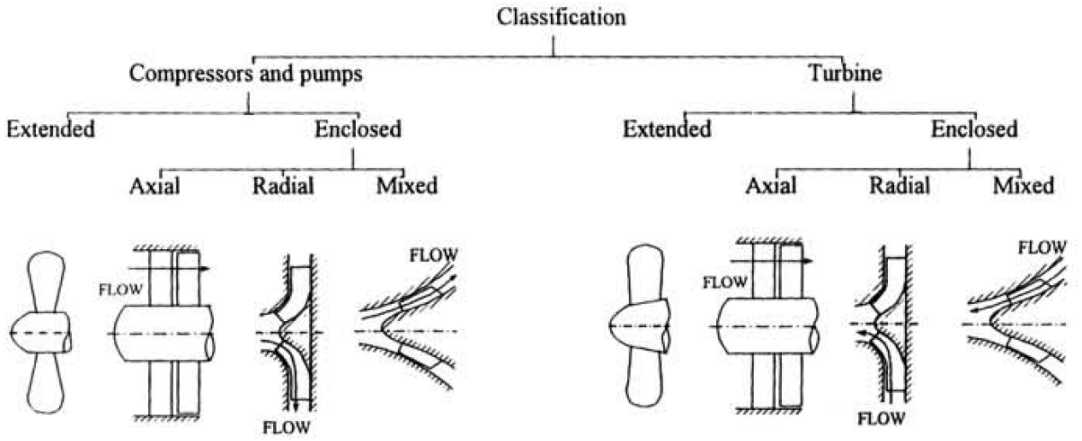

Figure 1: Classification of turbomachinery devices.

The main topic of this study mainly covers the high pressure stage of the turbine (work-producing turbomachine) that could be found within a typical turbo fan engine depicted in Figure 2. Thus, the purpose of the concerned part involves work extraction from the moving fluid that has adopted an axial flow pattern.

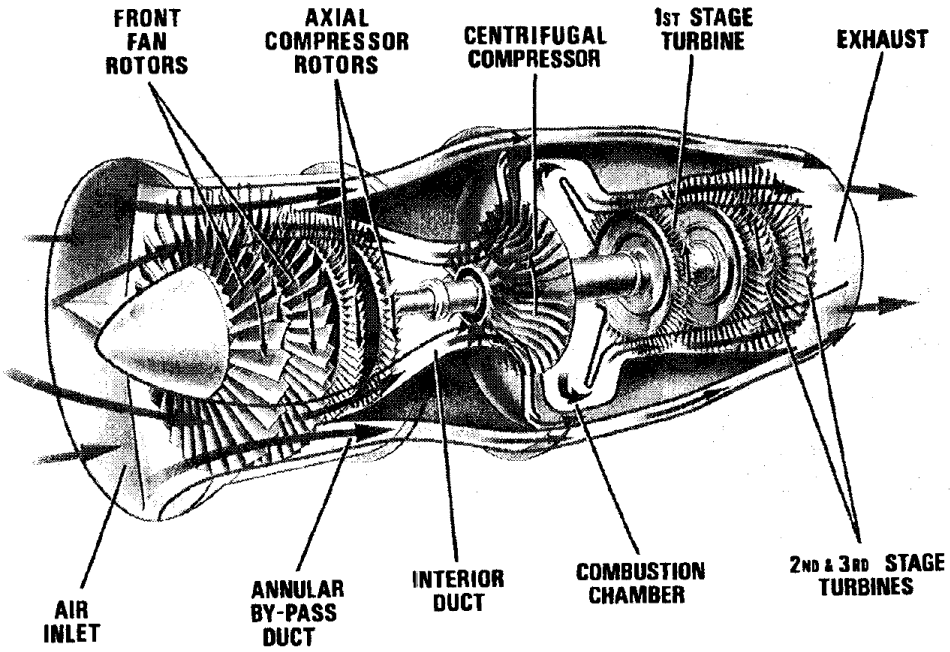

Figure 2: Layout of the turbo fan engine Williams F107. Courtesy of Williams International, Inc.

Before engaging the numerical simulation, it is necessary to present the physics of the flow in a turbine stage and the mathematical methods used to retrieve and measure the aerothermal properties of interest beforehand.

2.1 Overview of the flow mechanism

The purpose of the turbine is to sustain the energy consumption of the engine as a whole and to extract the energy from the working fluid by the means of the rotating motion of a rotor. A single turbine stage comprises respectively a stator and a rotor, each of these components serves a distinct purpose. The stator's utility is to guide the flow smoothly and readjusts the flow incident angle with respect to the rotor to allow an enhanced fluid/solid energy exchange. This is achieved by expanding the flow, that is, decreasing the static pressure (e.g. temperature, enthalpy and density) and accelerating the flow throughout the stator row whereas total quantities remain ideally constant. Additionally, this ideal situation with a favorable pressure gradient guarantees attachment of the boundary layer along the entire blade chord. Next comes the rotor's utility, as mentioned previously, it extracts mechanical work from the fluid by the intermediary of its rotating motion. Thus, the flow across the rotor row undergoes again an expansion and the main total quantities h_t, T_t, p_t and their corresponding static quantities h, T, p decrease. All this process can be further enhanced by adopting a slightly convergent-divergent nozzle shape duct.

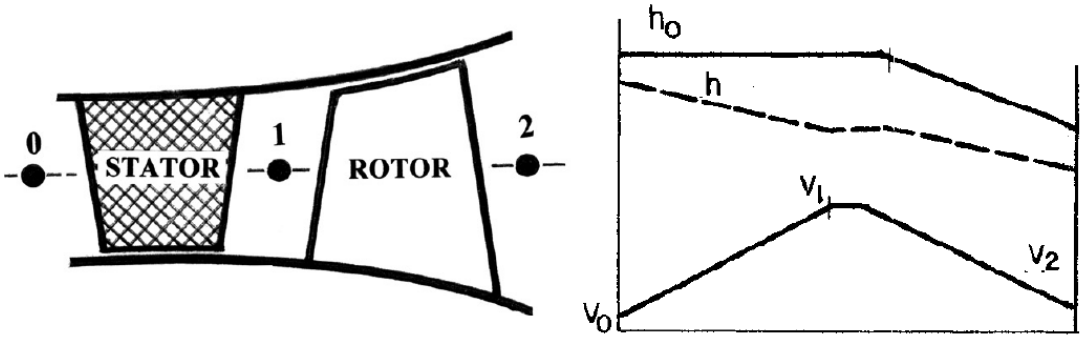

Figure 3: Variation of enthalpy across a turbine stage (h_0, h, V, the total and static enthalpies and the velocity).

Overall, a change of state is described from the thermodynamic point of view and its quantification is carried out with 1D turbomachinery performance analysis. This latter includes these following assumptions :

- The flow properties upstream and downstream of the blade row are directly correlated.
- In the same way, the upstream and downstream flows are uniform.
- The flow is assumed to be inviscid and steady with respect to the blades.
- The flow properties are circumferentially uniform.

By judging the nature of these assumptions, it is clear that this approach consists of a global assessment of the turbomachinery flow.

2.2 Velocity triangle

The first crucial concept to include in the performance analysis is the velocity triangle related to turbomachines. It is used to determine the flow velocity vector at the inlet and outlet of a specific row. In fact, the absolute velocity can be related to the relative velocity and the rotating blade velocity by the relationship

$$\mathbf{V} = \mathbf{W} + \mathbf{U}. \tag{2.1}$$

Note that the stator with its non-rotating component $\mathbf{U} = \mathbf{0}$ yields an equality between the absolute velocity and the relative velocity at any location on the vane.

This particular flow requires a blend of an absolute frame and a rotating frame attached to the body, and both employ respectively Cartesian coordinates (x, y, z with $\mathbf{e}_x$, $\mathbf{e}_y$, $\mathbf{e}_z$) and cylindrical coordinates (z, θ, r with $\mathbf{e}_z$, $\mathbf{e}_\theta$, $\mathbf{e}_r$).

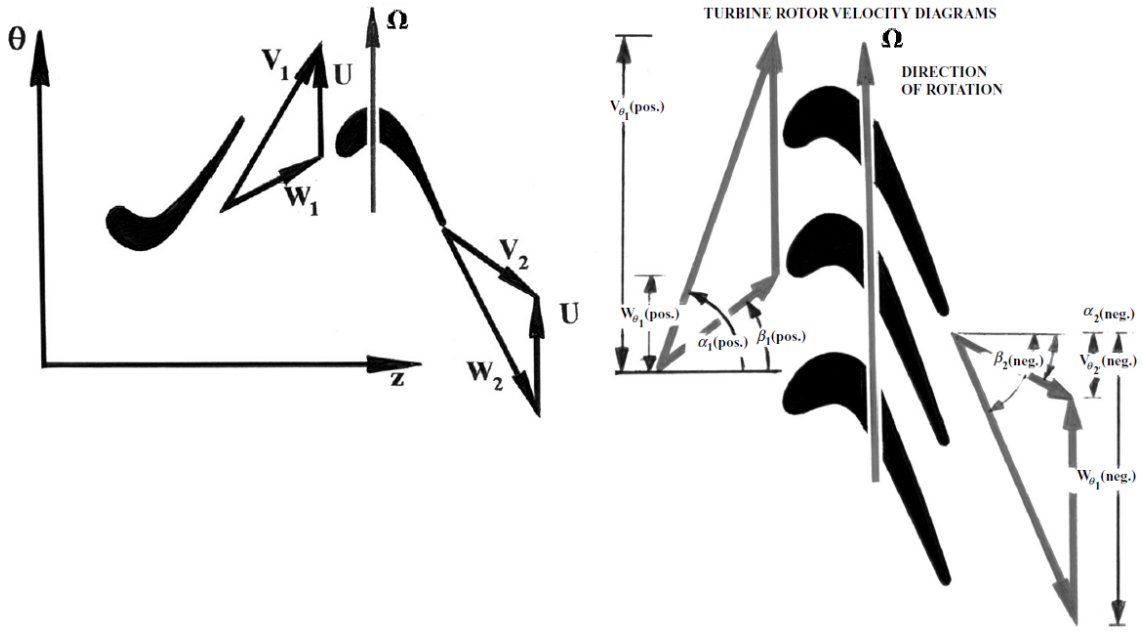

Figure 4: Local velocity triangles at inlet and outlet of the rotor row in the meridional plane with the sign conventions for the flow angles.

Note that the relative velocity vector $\mathbf{W}$ is highly dependent on the local shape of the blade-to-blade passage. Then, the blade velocity can be expressed as

$$\mathbf{U} = r\Omega\mathbf{e}_\theta.$$

For an axial turbomachine, $\mathbf{U}$ does not vary along the blade (in the streamwise direction) since the local radial coordinate r remains constant. These relations state the fact that the velocity triangle varies and the velocity magnitude increases along the rotating blade in the spanwise/radial direction. Consequently, the blade tip is more likely to reach a transonic/supersonic regime whereas the flow at the hub remains subsonic.

2.3 Turbomachinery variables

Energy transfer takes place at the level of the rotor row. In fact, output shaft power is extracted from the fluid which steadily applies a torque on the rotating blade. By recalling the Euler equation for axial turbomachinery, it is possible to relate the power output to the flow velocity components presented previously.

$$-P_w = \dot{m}U(V_{\theta 2} - V_{\theta 1}). \tag{2.2}$$

The present velocity components are measured at midspan of the blade element to estimate the power in an averaged sense. For the turbine, $V_{\theta 2}$ is smaller in magnitude than $V_{\theta 1}$, therefore the Equation 2.2 remains positive by sign convention adopted in this work. Additionally, by considering a basic control volume that envelops the rotating blade element, the energy equation applied to this control volume is written

$$\dot{m}(h_{t2} - h_{t1}) = Q - P_w. \tag{2.3}$$

Note that body forces are neglected in the energy balance for both inviscid and viscous flow. In normal circumstances, work associated to shear forces should be included in the energy equation

as well. However, if the control volume is extended to the inner and outer walls of the rotor row, where the no-slip boundary conditions are applied ($\mathbf{V} = \mathbf{0}$), then the Equation 2.3 is accurate for this performance analysis. Therefore, it should be recognized that this relation is also valid for viscous (including the associated losses) and compressible flows. By combining the Equations 2.2 and 2.3 and by dividing the terms by the mass rate, one can write

$$h_{t2} - h_{t1} = Q/\dot{m} + U(V_{\theta 2} - V_{\theta 1}). \tag{2.4}$$

For the efficiency definition that will be mentioned later on, it can be useful to drop the heat term $Q/\dot{m}$ by assuming an adiabatic flow to obtain

$$P_w/\dot{m} = h_{t1} - h_{t2} = U(V_{\theta 1} - V_{\theta 2}), \tag{2.5}$$

which shows that the total enthalpy drop is directly proportional to the change in tangential velocity and blade speed. The purpose of the efficiency concept is to compare the performance of the actual turbomachine to an ideal one which operates in isentropic condition. In the case of the single turbine stage, the total-to-total isentropic efficiency is defined as the ratio of total enthalpies

$$\eta_t = \frac{h_{t0} - h_{t2}}{h_{t0} - h_{t2is}} \leq 1. \tag{2.6}$$

If the temperature variation is not too large, the specific heat capacity can be assumed as constant between the inlet and outlet of the turbine stage. Then by applying the isentropic relationship that links the total temperature to the total pressure. One obtains an alternative form of the isentropic efficiency

$$\eta_t = \frac{1 - T_{t2}/T_{t0}}{1 - (p_{t2}/p_{t0})^{(\gamma-1)/\gamma}}, \tag{2.7}$$

which can be used to characterize the pressure drop with respect to the temperature drop across the turbine stage

$$\frac{p_{t2}}{p_{t0}} = \left[1 - \frac{T_{t0} - T_{t2}}{\eta_t T_{t0}}\right]^{\gamma/(\gamma-1)} = \left[1 - \frac{\Delta T_t}{\eta_t T_{t0}}\right]^{\gamma/(\gamma-1)}. \tag{2.8}$$

Alternatively, the isentropic efficiency can be approximated by referring to the inlet and outlet stations

$$\eta_t = \frac{h_1 - h_2}{h_1 - h_2 + T_2(s_2 - s_1)}. \tag{2.9}$$

If the flow inside the actual turbine stage is assumed to be adiabatic (especially for the guide vane), then one gets $T_{t1} = T_{t0}$, thus it is possible to relate Equations 2.5 and 2.7 to acquire

$$\frac{P_w}{\dot{m}} = c_p T_{t0} \eta_t \left[1 - \left(\frac{p_{t2}}{p_{t0}}\right)^{(\gamma-1)/\gamma}\right]. \tag{2.10}$$

The power transmitted to the rotor is therefore directly proportional to the inlet total temperature, the isentropic efficiency and the pressure drop across the rotor row.

In the case where the exhaust kinetic energy $V_2^2/2$ is seen as a loss that must be minimized, a similar measure to the total-to-total efficiency shown in Equation 2.7 is proposed and that is the total-to-static isentropic efficiency based on the exit static variables

$$\eta_{ts} = \frac{h_{t0} - h_{t2}}{h_{t0} - h_{2is}} \quad \text{or} \quad \eta_{ts} = \frac{1 - T_{t2}/T_{t0}}{1 - (p_2/p_{t0})^{(\gamma-1)/\gamma}}. \tag{2.11}$$

Now, it is necessary to investigate and summarize the main factors that condition the pressure drop or efficiency mentioned above. The dimensional analysis yields the following relationship

$$\frac{p_{t2}}{p_{t0}} \quad \text{or} \quad \frac{\Delta T_t}{T_{t0}} \quad \text{or} \quad \eta_t = f\left(\frac{\dot{m}\sqrt{RT_{t0}}}{p_{t0}D^2}, \frac{\Omega D}{\sqrt{\gamma RT_{t0}}}, \gamma, \frac{\Omega D^2}{\nu}\right). \tag{2.12}$$

The pressure drop is a function of in total four variables. Namely, the mass flow parameter, non-dimensional speed of the rotating blades, the ratio of specific heats of the gas and the Reynolds number. Note that in this case, the third term is dropped since γ of the perfect gas is assumed to be constant.
The compressibility effect is included in the two first variables since it is regulated by the local speed of sound which appears in both mass flow parameter and blade speed. In general, the most important non-dimensional variables that can considerably influence the pressure change or efficiency of the turbomachine are the mass flow parameter and the blade speed, as shown in Equation 2.5, whereas the Reynolds number has to vary its order of magnitude by 10 to be significantly effective. This dimensional analysis proves that the turbomachinery flow is in fact very sensitive to the boundary conditions and device's working regime. Consequently, quantitative comparison and valid reproduction of the flows strictly require the similar theoretical or experimental setup.

Further simplification can be brought, by considering a subsonic flow without shock wave, to Equation 2.12. Dividing the temperature ratio $\Delta T_t/T_{t0}$ by the squared second term $(\Omega D/\sqrt{\gamma RT_{t0}})^2$ and the first term $\dot{m}\sqrt{RT_{t0}}/p_{t0}D^2$ by again the second term $(\Omega D/\sqrt{\gamma RT_{t0}})$, one gets

$$\frac{\gamma R\Delta T_t}{\Omega^2 D^2} = f\left(\frac{\dot{m}RT_{t0}\sqrt{\gamma}}{p_{t0}\Omega D^3}, \frac{\Omega D}{\sqrt{\gamma RT_{t0}}}, \frac{\Omega D^2}{\nu}\right). \tag{2.13}$$

Then, dividing the temperature ratio and the first term by $\gamma - 1$ and $\sqrt{\gamma}$ respectively and applying the perfect gas law, one gets

$$c_p\frac{\Delta T_t}{\Omega^2 D^2} = f\left(\frac{\dot{m}}{\rho_{t0}\Omega D^3}, \frac{\Omega D}{\sqrt{\gamma RT_{t0}}}, \frac{\Omega D^2}{\nu}\right). \tag{2.14}$$

If compressibility and viscous effects controlled by the second and third terms are neglected, the loading coefficient can be consequently retrieved under the form

$$\psi = c_p\frac{\Delta T_t}{U^2} = f\left(\frac{\rho_{t0}V_z D^2}{\rho_{t0}\Omega D^3}\right) = f\left(\frac{V_z}{\Omega D\pi}\right) = f(\phi). \tag{2.15}$$

In the same manner, the loading coefficient ψ reflects the pressure/temperature change across the turbomachine and the flow coefficient ϕ reflects the effect of the mass flow and blade speed. According to Figure 4, the sign convention shows that U, $V_{\theta 1}$, $W_{\theta 1}$, α_1 and β_1 are positive whereas $V_{\theta 2}$, $W_{\theta 2}$, α_2 and β_2 are negative. The alternative loading coefficient in terms of the components of the velocity triangle for an adiabatic flow is written as

$$\psi = c_p\frac{T_{t1} - T_{t2}}{U^2} = c_p\frac{\Delta T_t}{U^2} = \left(\frac{V_{z1}}{U}\tan\alpha_1 - \frac{V_{z2}}{U}\tan\alpha_2\right). \tag{2.16}$$

Geometrically, there is the general relation $(V_z/U)\tan\alpha = (V_z/U)\tan\beta + 1$ from the velocity triangle at any location and with the flow coefficient $\phi = V_{z1}/U$, one has

$$\psi = [\phi(\tan\alpha_1 - \text{AVR}\tan\beta_2) - 1]. \tag{2.17}$$

Along with the Mach number based on the properties at the inlet of the rotor row

$$M_b = U/\sqrt{\gamma RT_1}, \quad M_{z1} = V_{z1}/\sqrt{\gamma RT_1}, \quad M_1 = W_1/\sqrt{\gamma RT_1}.$$

It is now possible to re-express the temperature drop from Equation 2.5 in terms of the components of the velocity triangle and the rotor inlet Mach number

$$\frac{T_{t2}}{T_{t1}} = 1 - \frac{(\gamma-1)M_b^2}{1+\frac{\gamma-1}{2}M_1^2}\left(\frac{M_{z1}}{M_b}(\tan\alpha_1 - \text{AVR}\tan\beta_2) - 1\right). \tag{2.18}$$

In the same way, Equation 2.8 can be rewritten under the form

$$\frac{p_{t2}}{p_{t1}} = \left[1 - \frac{(\gamma-1)M_b^2}{\eta_t\left(1+\frac{\gamma-1}{2}M_1^2\right)}\left(\frac{M_{z1}}{M_b}(\tan\alpha_1 - \text{AVR}\tan\beta_2) - 1\right)\right]^{\gamma/\gamma-1}. \tag{2.19}$$

Unlike the previous relationship, additional dependence on the inlet and outlet flow angles are clearly depicted in this equation. This consequently shows that higher turning angles (absolute angle difference $\alpha_1 - \alpha_2$ or relative angle difference $\beta_1 - \beta_2$) can actually produce larger temperature/pressure drop, thus resulting in a higher work output. In the same vein, if the angles α_1, β_2 and blade speed U were held constant, higher mass flow (the absolute Mach number M_{z1}) results in larger temperature/pressure drop. Alternatively, if the angles α_1, β_2 and mass flow $\dot{m}$ were fixed, higher blade rotating speed produces again larger temperature/pressure drop.

The last concept to introduce is the degree of reaction which is defined as a ratio of the static enthalpy across the turbine stage

$$R_c = \frac{h_1 - h_2}{h_1 - h_3}. \tag{2.20}$$

Again, it is possible to express this equation with the components of the velocity triangle presented above. For an adiabatic flow where relative total enthalpy remains constant, each term becomes

$$h_1 - h_2 = \frac{W_2^2 - W_1^2}{2}, \qquad h_1 - h_3 = h_{t1} - h_{t2} = U(V_{\theta 1} - V_{\theta 2}).$$

Hence, the degree of reaction of the turbine stage as a function of the relative flow angles within the rotor row is expressed as

$$R_c = \frac{V_z}{2U}(\tan\beta_2 + \tan\beta_1). \tag{2.21}$$

The degree of reaction classifies the type of turbine stage according to their specific features.

For the subsequent analysis, the quantities of interest will be adimensionalised. First, the pressure coefficient is given as

$$C_p = \frac{p - p_2}{\frac{1}{2}\rho_2 V_2^2}. \tag{2.22}$$

The temperature ratio is given by

$$\theta_T = \frac{T}{T_1}. \tag{2.23}$$

The following density ρ/ρ_1 and total pressure ratio p_t/p_{t1} are defined in the same way.

2.4 Mach number effect

According to Equations 2.18 and 2.19, another alternative that allows an enhanced temperature/pressure drop and work output, is to increase the rotating speed, the absolute inlet Mach number or the mass flow rate. However, the inlet Mach number can be increased indefinitely since chocking $M = 1$ will occur within the row passage. The chocking condition basically indicates that the amount of mass flow rate has reached a maximum and sonic state is observed at a specific throat area, thus the former is generally sought at designed operating condition to optimize the work output. Nevertheless, sonic state may induce generation of shock waves which must be avoided from the performance point of view. In fact, total pressure loss is observed across the shock wave region although this latter does no work and ensures constant total temperature/enthalpy for this adiabatic flow. With the 1D isentropic relation (shock-free) derived from the continuity equation for a chocked rotor row with $M = 1$ at A^*

$$\frac{A}{A^*} = \frac{S\cos\beta_1}{A^*} = \frac{1}{M_1}\left[\frac{2}{\gamma+1}\left(1+\frac{\gamma-1}{2}M_1^2\right)\right]^{(\gamma+1)/2(\gamma-1)} . \tag{2.24}$$

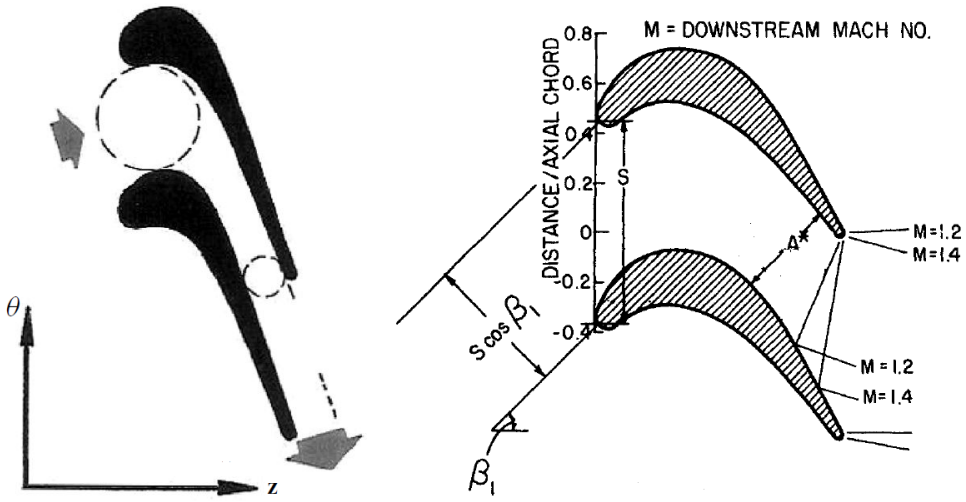

Figure 5: Effect of the Mach number within a rotor row passage in the blade to blade view.

The Equation 2.24 is used to determine the appropriate inlet relative Mach number M_1 for which choking condition occurs by setting the relative inlet flow angle β_1 and the chocked throat area A^*. In most designs, the passage between two neighbour rotor blades can be seen as a convergent duct depicted in Figure 5 and the sonic state is preferably sought near the trailing edge to avoid major mechanical energy loss caused by possible presence of aft shock waves on the suction side. Consequently, the throat area is progressively reduced as one moves towards the trailing edge. Additionally, the increase of the effective area ratio in Equation 2.24 results in a reduction of the inlet Mach number. Taking into account the consideration made above which is high inlet Mach number is needed to increase work output. A trade off between these two competing factors must be drawn and thus the flow must include a small supersonic region and weak shock waves to minimize the related losses. If the inlet Mach number happens to grow significantly, then the chocked throat area will retreat towards the leading edge, resulting in an extension of the aft supersonic region.

The most important parameter that conditions the features of the shock waves is the pressure at the exit of the rotor row. As mentioned above, the shaped adopted by the rotor passage behaves as a convergent nozzle that decreases the pressure and simultaneously accelerates the flow. The variation of the exit pressure of the rotor row leads to three possible scenarios.

- Under-expansion : The flow is subsonic at the inlet and outlet. A supersonic region and shock waves are formed inside the rotor passage. If the exit pressure is greater than the pressure reached

at the end of the rotor passage, a shock wave is generated within the passage to re-adjust the flow pressure with respect to the exit pressure. Now, if one decreases slightly the exit pressure, then the location of the shock wave will move downstream and the reachable Mach number before the shock will rise by a small amount as depicted in Figure 5. Additionally, reflection of the wave on the adjacent blade trailing edge is observed and this particular phenomenon can be interpreted as a perturbation that alters the properties of the flow even further downstream.

- Design-Expansion : The flow is subsonic at the inlet and supersonic at the outlet. Shock waves are absent in this ideal configuration since exit pressure is equal to the pressure reached at the end of the rotor passage.
- Over-expansion : The flow is subsonic at the inlet and supersonic at the outlet. Shock waves are again absent but expansion waves are formed at the trailing edge in this case. The flow mechanism is similar to the under-expansion. The exit pressure is lower than the pressure at the end of the rotor passage, this latter has to re-adjust the flow pressure with respect to the exit pressure, thus emanating expansion waves on the suction side instead.

The second scenario is, in practice, not attainable for the blade as a whole since the velocity triangle varies along the span. Consecutively, the inlet Mach number can not remain uniform in the spanwise direction, resulting in an under-expansion in most cases.

2.5 Tip leakage flow

Physically, this type of flow is mainly initiated by the presence of clearance between the blade tip and the shroud that envelops the whole rotor row. To carry out the analysis of the tip leakage flow, one has to determine its nature and magnitude beforehand.

Firstly, the leakage flow is driven by static pressure difference from both sides of the rotating blade. This situation is analogous to the 3D induced flow occurring at the wingtip of an aircraft during flight, except that in this case the body itself has adopted a rotating motion. The overall relative tip leakage velocity is basically made of two contributions, namely the free-stream velocity that ignores the presence of the gap and the tip leakage velocity that is perpendicular to the streamwise direction. Consecutively, the interaction of the main and tip leakage flows provokes a flow discontinuity since their flow angles differ. As a result, the leakage flow tends to roll up, forming the leakage vortex gradually washed downstream as depicted on the bottom side of Figure 6.

Then, the magnitude of tip leakage flow corresponds in this context to the mass flow rate across the gap. There are two crucial factors that controls the tip leakage flow, namely the clearance height and the blade loading (local static pressure difference of both sides of the blade). The first factor conditions the net amount of cross area perpendicular to the tip leakage velocity, it comes that the leakage mass flow rate is directly proportional to the gap height. Taking into account the fluid viscosity along with a diminution of the gap height, both wall boundary layers and separation region alter significantly the tip leakage velocity profile and reduce the net cross area, thereby limiting the mass flow rate to a minimum in the gap region as shown on the upper side of Figure 6. In practice, such configuration must be avoided although it is convenient from the performance viewpoint. To avoid any contact between the blade tip and the shroud at operating condition, a precise gap height has to be set despite the following increase of tip leakage mass flow rate. As cited above, the flow is driven by static pressure difference or more precisely, the tip leakage velocity is directly correlated to the pressure difference. To prove this statement, one can consider a inviscid and incompressible flow, the estimated tip leakage velocity is derived from the Bernouilli equation

$$V_{\perp} = \sqrt{\frac{2(p_p - p_s)}{\rho}}. \tag{2.25}$$

Hence, the mass flow rate increases in the same manner as for the blade loading.

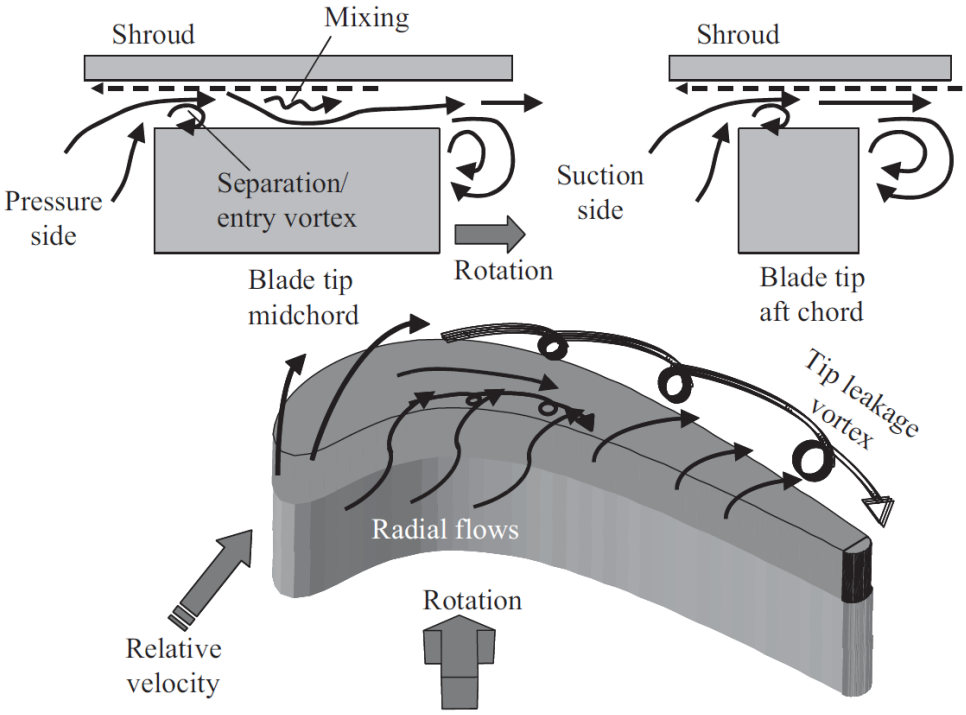

Figure 6: Nature of the tip leakage flow.

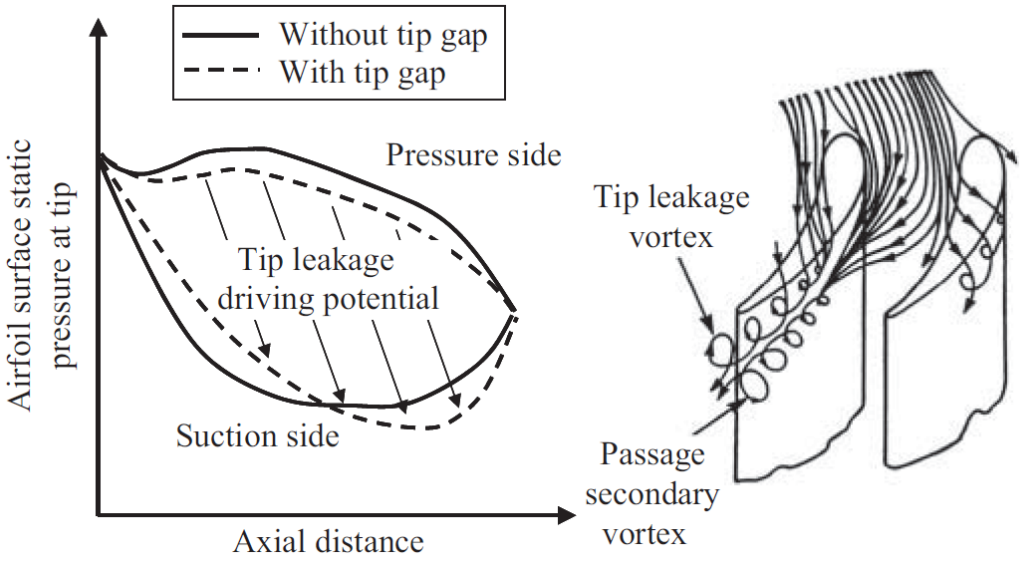

Figure 7: Influence of the tip leakage flow on the static pressure distribution around the blade tip.

Next, the considerations mentioned above are only valid for an ideal situation since complications arise from the possible interaction of the tip leakage flow with other secondary flows as shown in Figure 7 and 8, they include scraping vortex, passage vortex, corner separation, shock waves, etc... For example, the mechanism of tip leakage vortex formation can be prevented by early diffusion caused by high level of turbulence or/and large separation zone. Figure 7 effectively depicts the alteration of the static pressure brought by the flow on both sides of the blade. As mentioned earlier, the tip leakage flow magnitude depends on the blade loading which is strengthened in the aft chord region. Consequently, enhanced tip leakage will be observed in the same region whereas the leading

edge will remain relatively calm. Nevertheless, tip leakage flow can be beneficial in presence of corner separation region. In fact, the separation region also constitutes a aerodynamic loss and the antagonist flow interaction can effectively diminish the extent of the region.

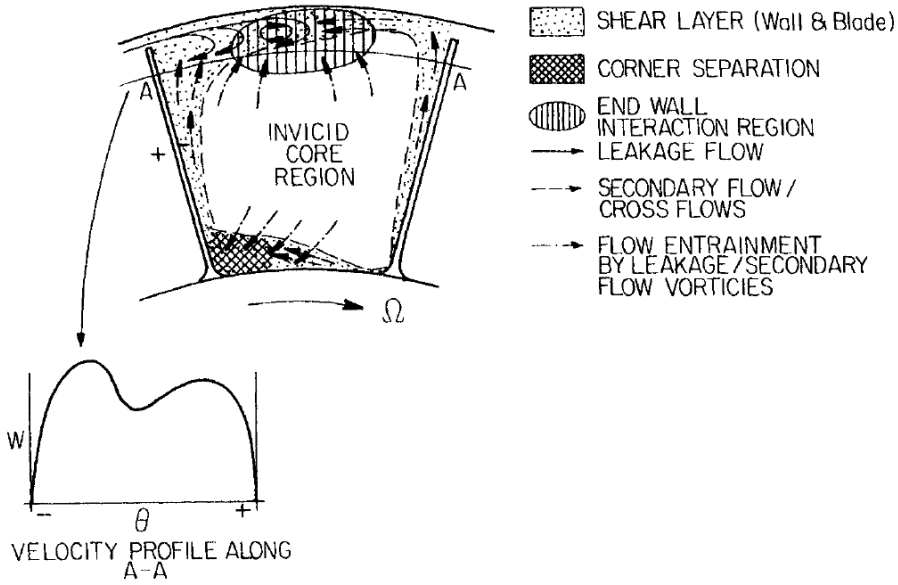

Figure 8: Interaction of the tip leakage jet with secondary flows at aft chord

To understand and visualize the tip leakage in more details, one can refer to the work of Lee et al. [11]. The purpose of their experiment is to study and measure the heat/mass transfer through a flat tip gap for different clearances (0.68%, 1.36%, 2.04% and 2.72% of the span). Flow visualization and heat transfer/mass flow measurement are made possible by employing respectively the high-resolution oil film method and the naphthalene sublimation technique.

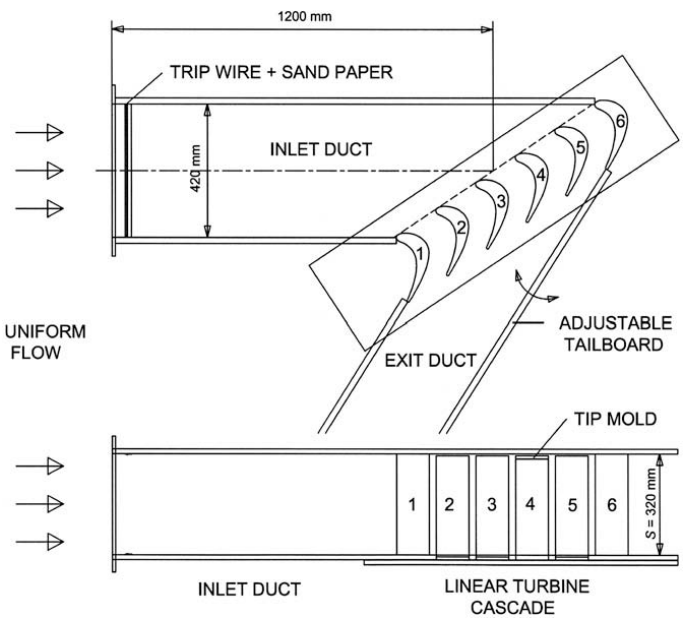

(a) Cascade wind tunnel

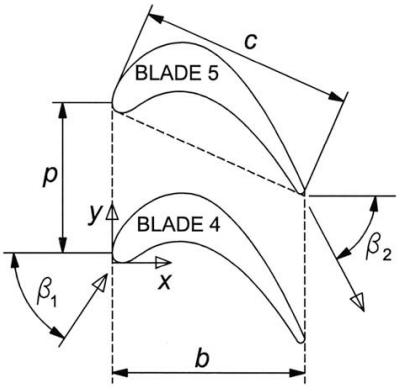

Number of blades	6
Chord length (c)	217.8 mm
Axial chord (b)	196.0 mm
Pitch (p)	151.6 mm
Span (s)	320.0 mm
Blade inlet angle (β_1)	56.4 deg
Blade outlet angle (β_2)	-62.6 deg

(b) Blade geometry.

Figure 9: Overview and data of the cascade presented in Lee et al. [11].

The boundary conditions set at the entrance of the cascade are described as follow : The inlet ambient air is blown at velocity of 15 m/s and the Reynolds number based on this inlet velocity and the blade chord is 2.09×10^5. The measured inlet turbulence intensity is 0.3%.

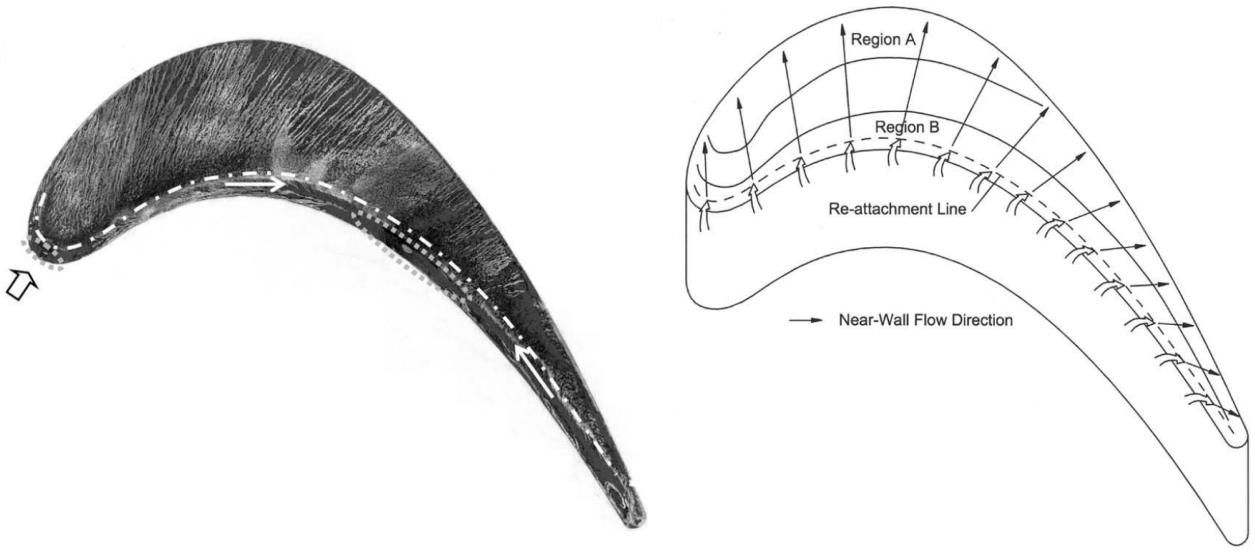

(a) Surface oil pattern. (b) Flow model.

Figure 10: Overall flow visualization and concept over the entire flat tip for tip clearance 1.36%. Courtesy of Lee et al. [11].

Two major flows were distinguished as an outcome of their study. Namely tip-gap vortices and flow separation/re-attachment over the pressure side tip edge.

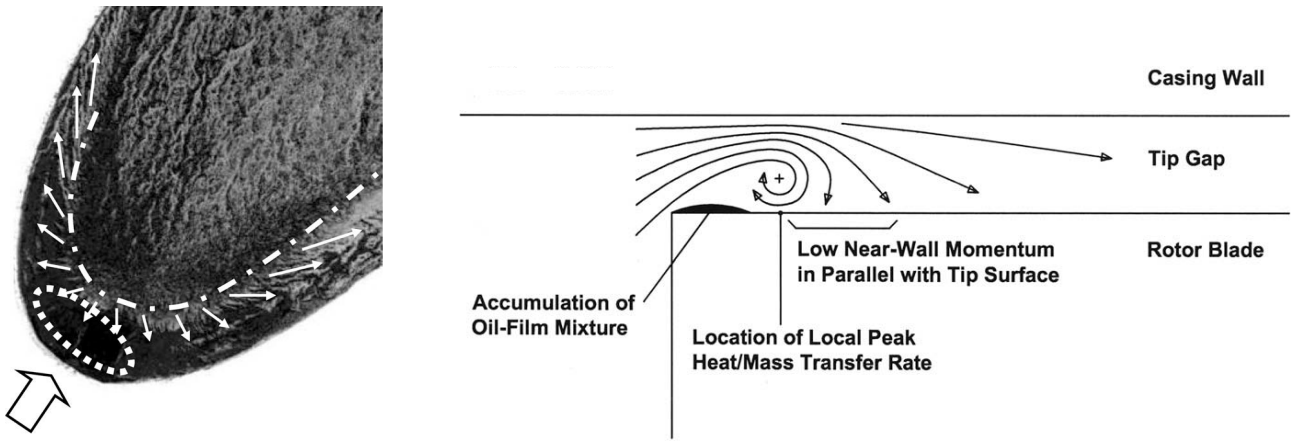

(a) Surface oil pattern. (b) Flow sketch in the stagnation plane.

Figure 11: Identification of the pair of tip-gap vortices at the leading edge for tip clearance 1.36%. Courtesy of Lee et al. [11].

Firstly, the tip-gap vortices is observed at the leading edge and thus a focus on this area is required. Figure 11a depicts the oil pattern drawn by the flow on the leading edge. The C-shape dashed line marks the location of local heat and mass flow rate peak. The dark area located above the dashed line indicates low interaction between the wall (especially the surface oil) and the incoming flow, the latter possesses low near wall momentum in this region. On the opposite, the bright area located below the dashed line is able to exhibit the flow direction, this is only possible by the means of strong flow-wall interaction. These features suggest a flow separation and consecutively a rolling-up at the gap entry as shown in Figure 11b. This essentially constitutes the formation mechanism of

tip-gap vortices of which the center is assumed to be located along the dashed line. At the leading edge, the impingement of the flow produces a horseshoe vortex that eventually separates into a pair of opposite direction vortices. Additionally, the elliptic region underlined by the dotted line results from the reversed flow of the entry separation at the leading edge since accumulation of oil mixture is observed. In sum, the areas that surround the tip-gap vortex (front and rear in Figure 11b) within the recirculation zone are characterized by low near wall flow momentum. Conceptually, the re-attachment point must evidently be located a bit above the dashed line in Figure 11a or a bit after the underlined low near wall flow momentum area in Figure 11b. However, their study assumes that the dashed line can represent approximatively the re-attachment as well, meaning the recirculation zone at rear of the tip-gap vortex (see Figure 11b) can be neglected.

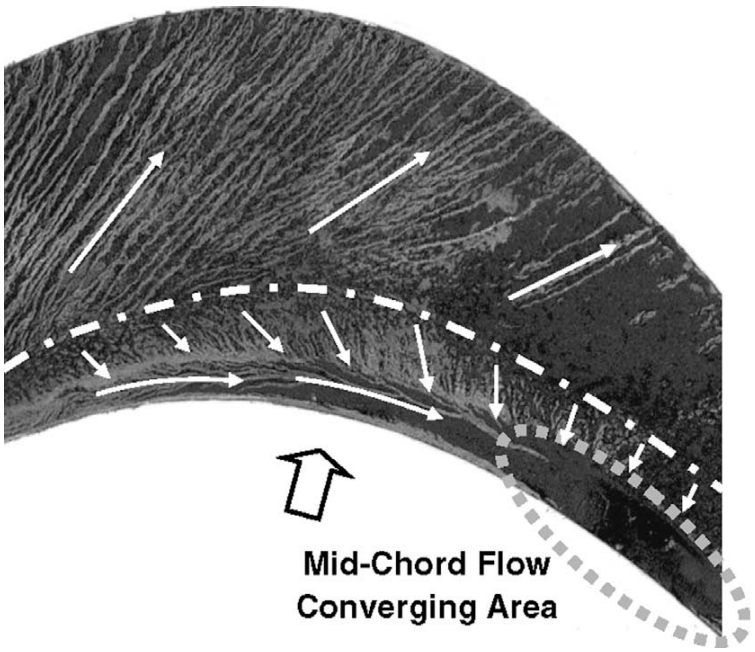

Figure 12: Identification of the re-attachment phenomenon in the mid-chord region for tip clearance 1.36%. Courtesy of Lee et al. [11].

Now, Figure 12 focuses on the mid-chord region. The dashed line still represents heat and mass flow rate peak location and re-attachment as in Figure 11a. The arrows above the dashed line indicates the direction of the tip leakage flow evidently driven by the blade loading. However, below the dashed line, presence of reverse flow within the separation bubble pushes the oil mixture towards a converging area in which oil mixture accumulation is again observed near the mid-chord pressure side edge. This is due to the strong concave curvature of the high turning blade that deviates considerably the flow. In conclusion, the development of the boundary layers specific to tip leakage flow is delayed because of the entry flow separation on the pressure side edge. The reverse flow region inside the separation bubble and re-attachment line comprise large wall velocity gradient that can effectively enhance heat transfer and mass flow rate. The author has divided the tip into two regions in order to highlight spatial distribution of the heat transfer and mass flow rate. The regions A and B shown in Figure 10 characterize respectively areas of low and high heat/mass transfer.

Lastly, the most important features of the tip leakage are gathered here.

- The tip leakage flow is three dimensional and spreads inward in the spanwise direction (about 10-30% of the span from the tip in most cases). Additionally, the dissipation and mixing of the tip leakage flow with the main flow introduce an substantial aerodynamic loss that typically vary between 2-4%.
- Effective energy conversion is absent in tip leakage flow. It implies that the energy content

transported by the tip leakage flow remains relatively high. Consequently, the gap region and its surrounding are exposed to higher gas exhaust temperature, again rendering the blade tip susceptible to additional thermal loading.

2.6 Turbomachinery flow losses

Turbomachinery flows are generally complex due to the interactions between secondary flows and the main flow. The latter oftenly results in aerodynamic losses that can be classified hereby.

- Profile losses : These are related to the viscosity of the fluid. Presence of wall boundary layers (including separation regions) and mixing layers contributes to mechanical energy dissipation (laminar and turbulent) into heat. Entropy increase and relative total pressure drop will inevitably reduce the work output and concurrently the stage efficiency. Since the flow is three-dimensional, the losses will depend on additional parameters, such as the radial pressure distribution, blade twist, aspect ratio, curvature, rotating speed, etc...
- Shock losses : As explained in the upper section, decrease of relative stagnation pressure is observed across a shock wave for an adiabatic flow. Again, mechanical energy is dissipated by viscosity in the very thin layer formed by the shock wave. In response to the increase of the entry velocity magnitude along the span (from hub to tip), the nature/location of the shock is gradually modified (e.g. leading edge, passage and trailing edge shocks). Additionally, there exists an interaction between the shock wave and the boundary layer. The sudden static pressure rise thickens the boundary layer across the shock and may cause early flow separation by inducing an adverse pressure flow.

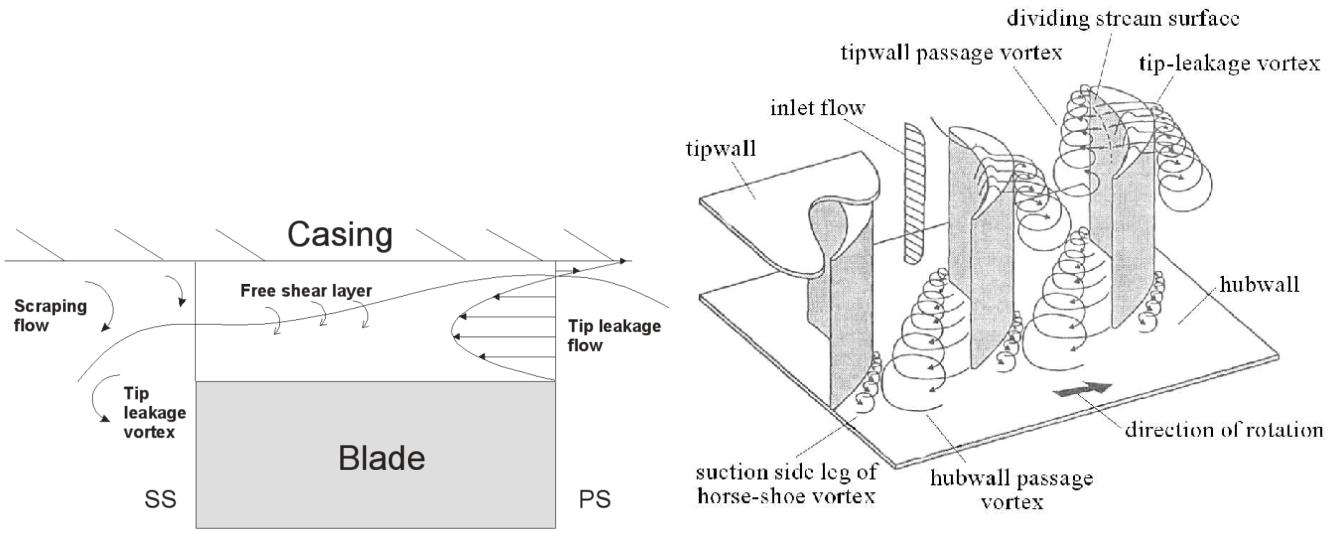

(a) Scraping vortex.

(b) Passage vortex.

Figure 13: Formation mechanism of the scraping and passage vortices at tip-wall.

- Secondary flow and End-wall losses : They mainly concern all sort of vortices present in the flow and their possible interaction with the wall boundary layers or/and mixing layers. In general, these two loss sources are intertwined. For example, the corner separation arises from the presence of adverse pressure gradient right after the leakage flow leaves the gap from the suction side edge. On the other hand, the scraping vortex results from the relative rotating motion between the blade and the casing as shown in Figure 13a. Furthermore, the passage vortex generated by the presence of the rotating blades is depicted in Figure 13b. The cited vortices are superposed to the tip leakage vortex in most cases, adding to more performance inefficiency as shown in Figure 14.

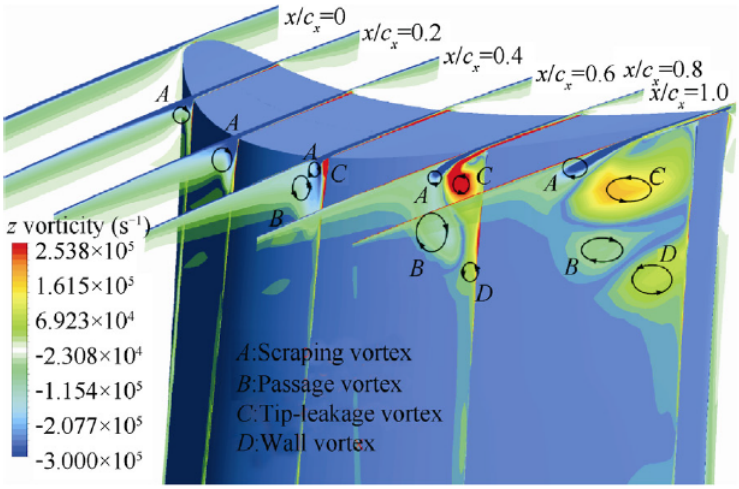

Figure 14: Superposition of different vortices on the suction side. Courtesy of Wei et al. [19].

Several parameters intervene for these types of loss, such as the Reynolds number, the loading coefficient, the flow angles, the blade camber, etc...

- Clearance losses : They are essentially caused by the existence of a gap between the casing and blade. As mentioned before, the clearance increase reduces the work output and efficiency. Figure 15 exhibits the sensitivity of the stage efficiency with respect to the tip clearance for different tip profiles and the ratio can substantially vary between 1:1 and 2:1. On the other hand, the tip leakage flow depends as well on parameters like Reynolds number, rotating speed, tip profile, flow angles, etc...

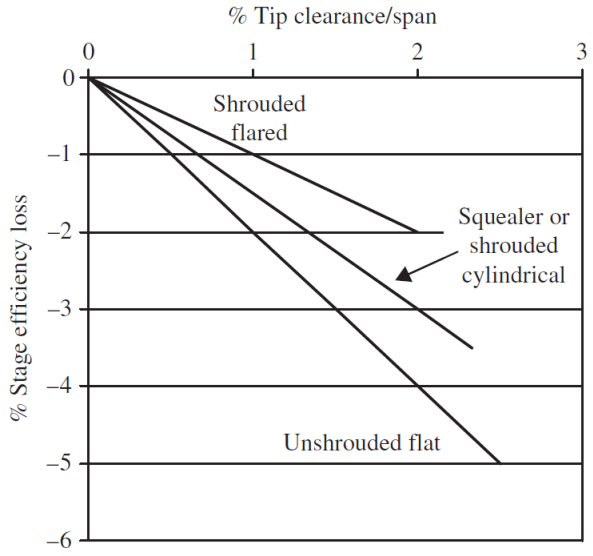

Figure 15: Effect of clearance on stage efficiency for different tip profile. Courtesy of Bindon [17].

In general, correlations and empirical formulas exist for the estimation of each loss component but only for simplified cases (e.g. inviscid, 2D, incompressible flows). Whenever a real 3D flow is considered as a whole, crucial dependence of the loss component on the stage configuration and operating conditions is conceded and the approach based on empirical correlations obtained by dimensional analysis is no longer valid. Thereby, this complex turbomachinery flow has to be treated by qualitative comparison to similar existent studies. As a matter of fact, Figure 16 summarizes all the loss components for different types of experimental turbine stage. The results show that the losses that occur in stator account for about 25% of the entire stage losses. Of the remaining 75% rotor losses,

the tip clearance loss constitutes roughly one third of the total loss, which is considerable. Therefore, improvement should be brought to the stage design in order to minimize the clearance loss whenever possible.

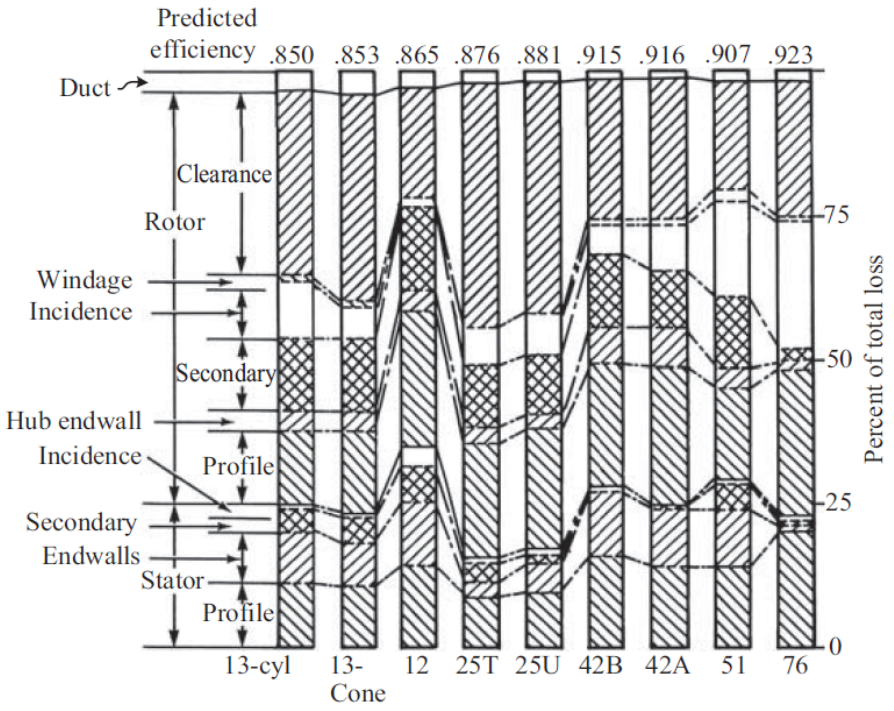

Figure 16: Summary of the losses for different single stage. Courtesy of Booth [18].

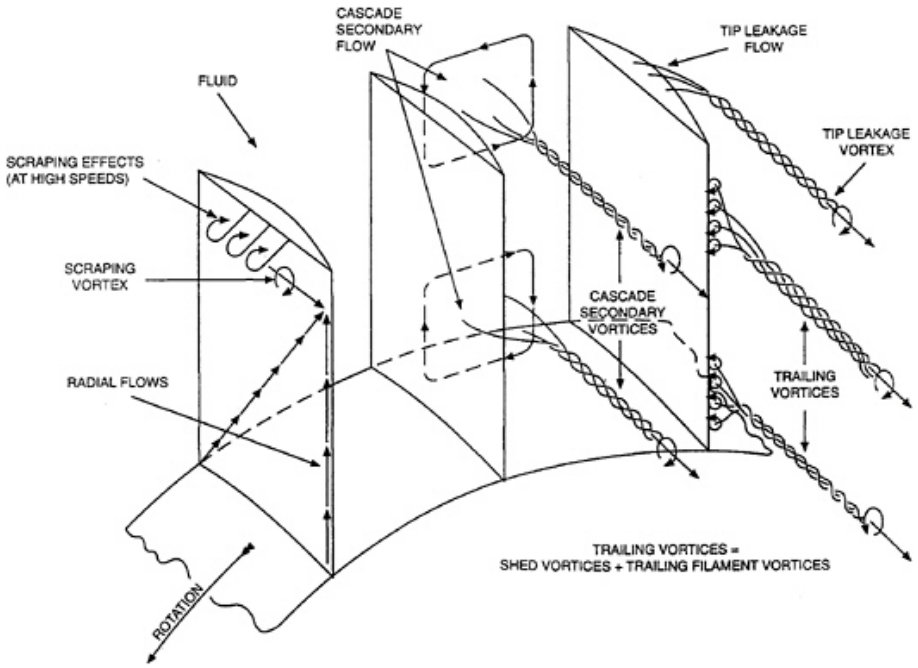

Figure 17: Main vortices contributing to aerodynamic losses in a turbine stage flow

2.7 Heat transfer

The first high pressure stage is usually exposed to hot incoming air during operation, heat transfer between the working fluid and the turbine components is inevitable. The main focus of this study is

the fluid-solid interaction, thus the targeted heat transfer phenomenon takes place at the interface of the two media. Theoretically, the most crucial elements that intervene in this type of heat transfer are the blade wall boundary layer and free-stream flow total temperature (absolute or relative). The first element acts as a buffer zone confined between the free-stream and the blade wall and provides additional insulation to the body. In fact, fluid-solid interface heat transfer occurs within the viscous layer (laminar sublayer of the boundary layer) in which weak conduction (small temperature gradient) and convection (low velocity) mechanisms concurrently take place. Conclusively, the wall boundary layer plays a key role in fluid-solid heat transfer. Nevertheless, the interface heat transfer is driven by the temperature difference as formulated though Newton's cooling law

$$q = h_c(T_{ad} - T_w) = k\left(\frac{\partial T}{\partial n}\right)_w. \tag{2.26}$$

Note that the dominant heat exchange phenomenon for this type of flow is forced convection. Transition to turbulent regime brings supplementary fluctuations to the velocity and temperature fields. The associated turbulent heat transfer is assumed to be dependent on the wall temperature gradient in the same way as the laminar one, thus

$$q_t = c_p k_t \frac{\partial T}{\partial n}. \tag{2.27}$$

Hence the total heat flux can be written as a sum

$$q = c_p\left(\frac{\mu}{Pr} + \frac{\mu_t}{Pr_t}\right)\frac{\partial T}{\partial n}. \tag{2.28}$$

It must be emphasized that the Prandtl numbers Pr and Pr_t are respectively a physical property of the fluid and a property of the flow field. The features of the new turbulent parameters will thoroughly be discussed at the description section of turbulence modelling. In practice, it is possible to have a first guess on the adiabatic wall or recovery temperature T_{ad} as a function of the Prandtl number, the free-stream Mach number and temperature

$$T_{ad} = T_e\left(1 + r_h\left(\frac{\gamma - 1}{2}\right)M_e^2\right). \tag{2.29}$$

Where the parameter r_h is equal to $r_h = \sqrt{Pr}$ for laminar flow and $r_h = Pr^{1/3}$ for turbulent flow. However, this method may encounter a major drawback especially in complex flows as this one. In fact, the free-stream properties can not remain uniform in the direction normal to the wall and are subjected to fluctuations and flows interaction, making them impractical for use. To remediate this issue, an approach based on the temperatures T_w and T_{ad} is proposed instead in the following sections. Alternatively, the non-dimensional measure of the heat transfer characterized by the wall temperature gradient, corresponds to the Nusselt number

$$Nu_L = \frac{h_c L}{k} = \frac{L}{T_{ad} - T_w}\left(\frac{\partial T}{\partial n}\right)_w.$$

Strong interaction between the velocity and temperature fields must be acknowledged. For example, large temperature difference can condition fluid density variation which in turn inevitably affects the velocity field. On the other hand, these two properties can also share some common features. The momentum and energy transport equations introduced later on are similar ; the thickness of the thermal and velocity boundary layers are equal if $Pr = 1$.

It is possible to demonstrate the velocity-temperature coupling through the Nusselt number for this study and consecutively the insulation feature of the boundary layer, by considering a simpler flow. This latter consists of a 2D incompressible flow over a flat plate, which has the aim in this context to

provide an insight to the nature of the physical process in turbomachinery flows. Firstly, the similarity or the relationship between the velocity and temperature fields can be depicted in the ideal conditions ($Pr = 1$ and laminar flow)

$$\frac{k}{\rho c_p (T_{ad} - T_w)} \left(\frac{\partial T}{\partial n}\right)_w = \frac{\mu}{\rho} \left(\frac{\partial u}{\partial n}\right)_w . \tag{2.30}$$

By introducing the non-dimensional heat flux measure Stanton number specific to this idealized flow

$$St = \frac{q}{\rho c_p V_e (T_{ad} - T_w)} = \frac{k}{\rho c_p V_e (T_{ad} - T_w)} \left(\frac{\partial T}{\partial n}\right)_w = \frac{C_f}{2}. \tag{2.31}$$

By performing some substitutions, the important result eventually shows that the wall heat flux (temperature gradient) actually depends on the skin friction coefficient (velocity gradient). By recalling the Nusselt number and by omitting the condition $Pr = 1$, one can exploit the analytical solution of the flow over a flat plate undergoing forced convection

$$C_f = \frac{0.664}{\sqrt{Re_x}}, \qquad StPr^{2/3} = \frac{C_f}{2}.$$

Hence for the laminar flow

$$Nu_x = \frac{qx}{k(T_{ad} - T_w)} = StRe_x Pr = 0.332 Re_x^{1/2} Pr^{1/3} = \frac{C_f}{2} Pr^{1/3} Re_x. \tag{2.32}$$

In the same manner for the turbulent flow

$$C_f = \frac{0.058}{Re_x^{1/5}}, \qquad StPr^{2/3} = \frac{C_f}{2}.$$

$$Nu_x = 0.029 Re_x^{4/5} Pr^{1/3}. \tag{2.33}$$

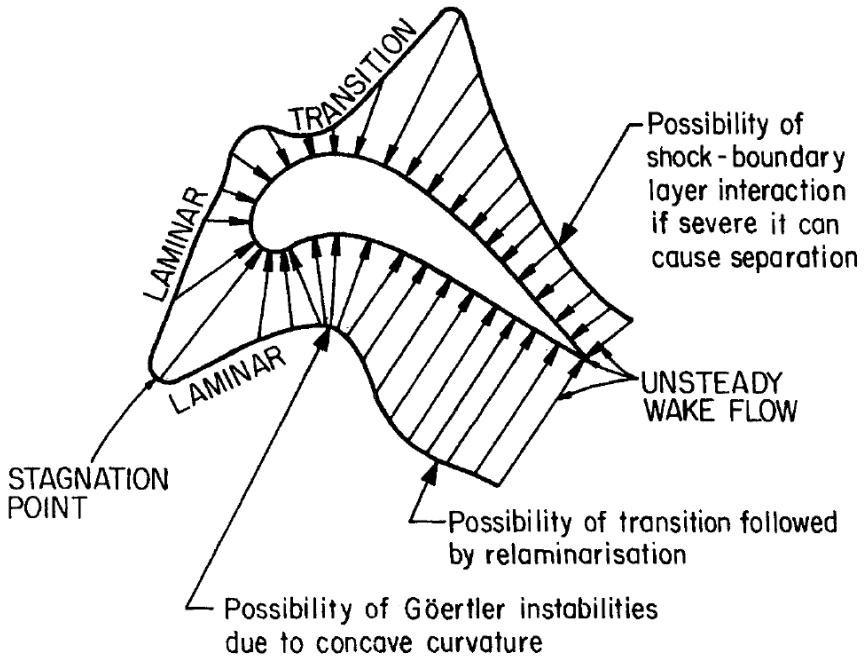

Figure 18: Variation of wall heat flux around the turbine blade.

In summary, for either laminar or turbulent flow, the Nusselt equation for forced convection can be expressed as function of the Reynolds and Prandtl numbers

$$Nu_x = ARe_x^m Pr^n. \tag{2.34}$$

Where A, m and n are constants in this context. Large temperature and velocity gradients are observed in thin boundary layers and at singular re-attachment points that follow a separation region, therefore large heat transfer will also be observed in these areas according to Equation 2.32. By referring to Equation 2.28, the presence of turbulence (in most cases μ_t/Pr_t is greater than μ/Pr) increases heat transfer, it comes that turbulent boundary layers are less insulative than same thickness laminar boundary layers. On the opposite, the temperature gradient tends to be smaller in the thick boundary layer and flow recirculation region which bring an effective insulation effect to the wall. In conclusion, the heat transfer rate highly depends on the local wall velocity and temperature gradients. By applying these results to turbomachinary flows, maximum heat transfer on the turbine blade usually occurs near the stagnation point and near the leading edge as depicted in Figure 18.

Again, it is possible to refer to an experimental study in order to understand and visualize the tip heat transfer mechanism in more details. The chosen work comes from Bunker [16] and studies the impact of different tip profiles and clearances on the aerodynamic efficiency of a industrial turbine stage. The default boundary conditions for this experiment are : The inlet Mach number is equal to 0.4, the total-to-static pressure ratio (inlet to outlet) is fixed at 1.43 with exhaust ambient pressure, the tip clearance is set at 1% of the blade span.

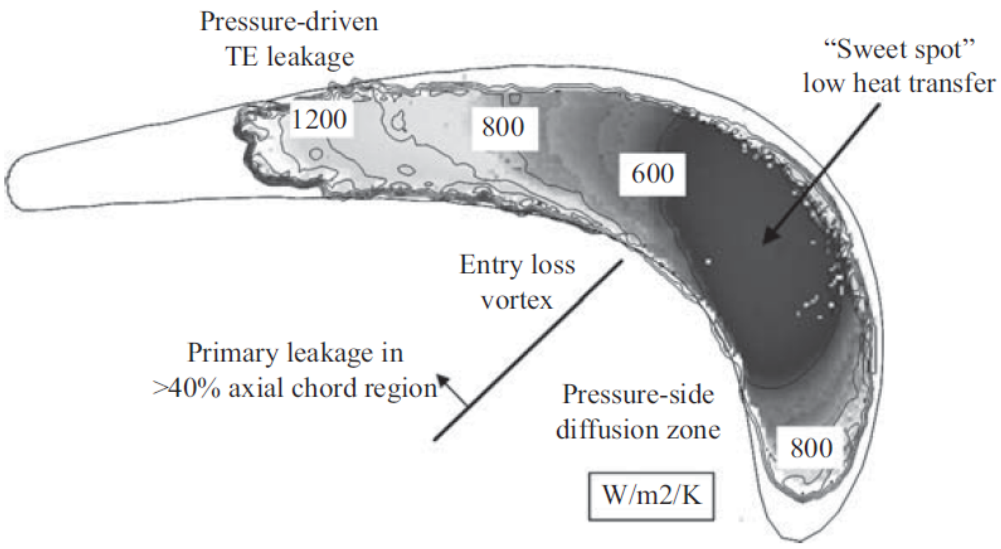

Figure 19: Distribution of heat transfer coefficient over the flat plate for tip clearance 1%. Courtesy of Bunker [15].

Figure 19 depicts an intriguing feature. It is the existence of a sweet spot in which heat transfer is at the lowest with respect to other surrounding regions. This can be explained by invoking the total-to-static pressure ratio diagram from Figure 20. The author has particularly measured the total pressure (eventually divided by the static pressure at the suction side edge) at the pressure side edge, camberline and suction side edge (named respectively P/S, Meanline and S/S) for different tip clearances. The identified sweet spot is characterized by low pressure ratio (i.e. blade loading), which means that tip leakage in this region is weaken. On the contrary, the region that covers the mid-chord to trailing edge is highlighted by large pressure ratio, which means that tip leakage is strengthened. These features imply that tip leakage vortex is likely to take form at mid-chord and extends to the trailing edge. In sum, this study has proven the dependence of heat transfer on blade loading. Nevertheless, the high heat transfer, near the pressure side edge and leading edge, due to flow re-attachment is still noticeable and obey approximatively the zonal repartition depicted in Figure 10. Simultaneously, this implies that flow re-attachment at the leading edge is the main cause that contributes to high heat transfer since blade loading is poor in this region according to Figure 20. Thereby, the results of Bunker et

al. [15] and Lee et al. [11] agree qualitatively although their experimental setup fundamentally differ.

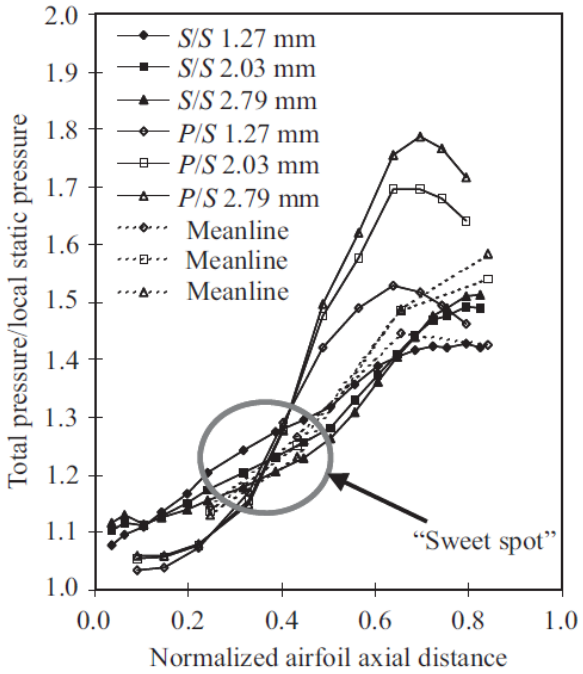

Figure 20: Total-to-static pressure ratio along the axial chord for different tip clearances. Courtesy of Bunker [15].

2.8 Review of the transonic test turbine facility

The turbine stage adopted in this study is taken from the Institute for Thermal Turbomachinery and Machine Dynamics (TTM) and more precisely from the doctoral thesis of Erhard [10]. The objective of his work is the design of a new transonic turbine stage which is able to operate efficiently between 7000 and 11500 RPM and deliver a power up to 2.75 MW. For consistency, a brief review of the features and capabilities of the test turbine facility is carried in this section.

The facility possesses the following basic components :

- Two inlet lines (from the inlet filter and the supply pipe) that can work in series or in parallel.
- A compressor station that drives the main flow and a brake compressor that provides additional mass flow if needed.
- A mixer that combines the flow from the two inlet lines.
- The test turbine stage of interest.
- An nozzle shape exhaust line.

The assembly can work at different operating conditions defined by the user. For example, the mass flow input can vary from 2.5 kg/s to 16 kg/s with a pressure of 2.9 bar if the inlets operate in parallel. Nevertheless, for safety reasons and considering the limitation of the material exposed to high temperature, the total pressure and temperature at the inlet are strictly limited under 4.7 bar and 458 K respectively. The main features of the geometry of the turbine stage, used to build the computational domain later on, in the meridional path :

- The stage inlet diameters vary from 360 mm to 620 mm.

- The test section inserts maximum diameter is 800 mm.
- The test section length is set at 406 mm.

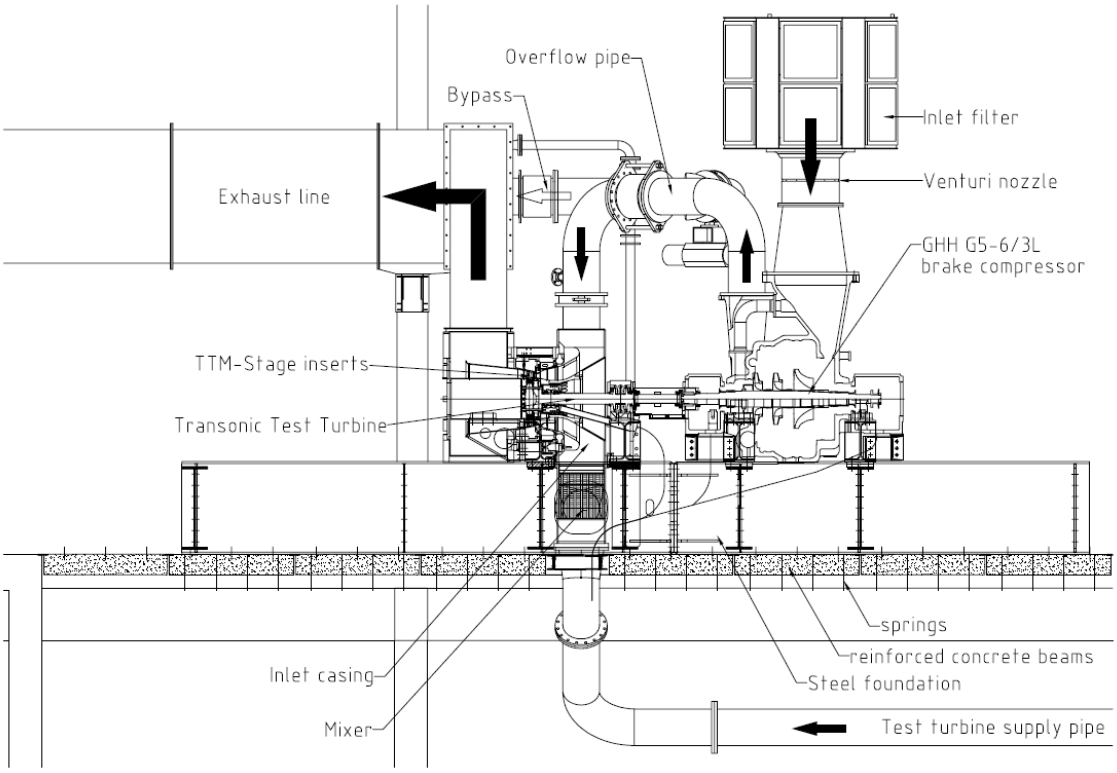

Figure 21: Front view of the test turbine facility. Courtesy of Erhard [10].

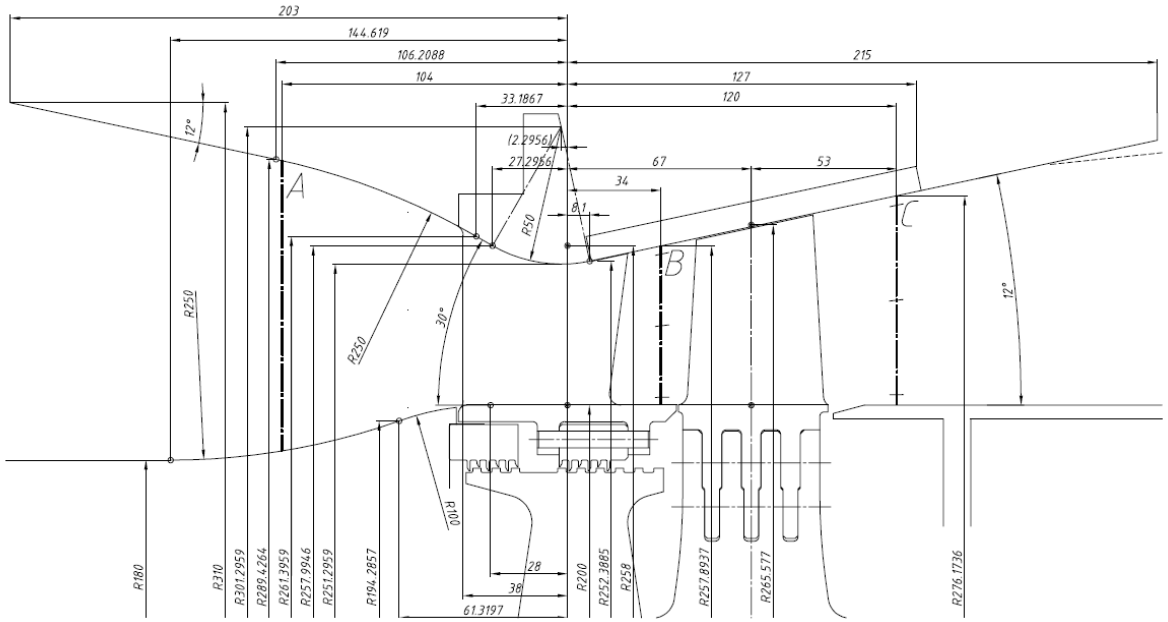

Figure 22: Sketch of the turbine stage with measurements in [mm]. Courtesy of Erhard [10].

The locations A, B, C depicted in Figure 22 indicate the stations on which flow properties are estimated with the 1D performance analysis. For this design, the stator row and the rotor row include in total 24 guide vanes and 36 blades respectively.

Another important aspect to emphasize about the design of this turbine stage is the rotor tip clearance. This latter must take into account several constraints (e.g. flow unsteadiness, centrifugal forces, thermal expansion, etc...) that result in a variation of the tip clearance due to deformation of the rotating blades during operation. The presence of steady pre-stress in the structure requires an initial cold clearance of 0.5 mm at ambient temperature and at 0 RPM. However, because of the thermal expansion and the elastic centrifugal blade tip elongation observed at 454.4 K and 11000 RPM, additional clearance enlargement of 0.3 mm is considered for the steady regime. Additionally, unsteadiness (e.g. stress or heat) requires an extra clearance consideration of 0.2 mm. Hereby, the tip clearance is eventually fixed at $\tau = 1$ mm which is equivalent to 1.43 % clearance/span. The geometric features of the guide vanes and blades are gathered below.

	Vane	Blade
Airfoil count	24	36
True chord [mm]	78.9	55.9
Axial chord [mm]	56.1	46.8
Pitch [mm]	60	41.6
Pitch to chord ratio [-]	0.76	0.74
Airfoil span [mm]	55.2	69.8
Aspect ratio [-]	0.7	1.25
Turning angle [°]	70	107
Exit Swirl [°]	70	15
Zweifel's coefficient (tip) [-]	0.67	0.94

Table 1: Geometry of the guide vanes and blades of the turbine stage. Courtesy of Erhard [10].

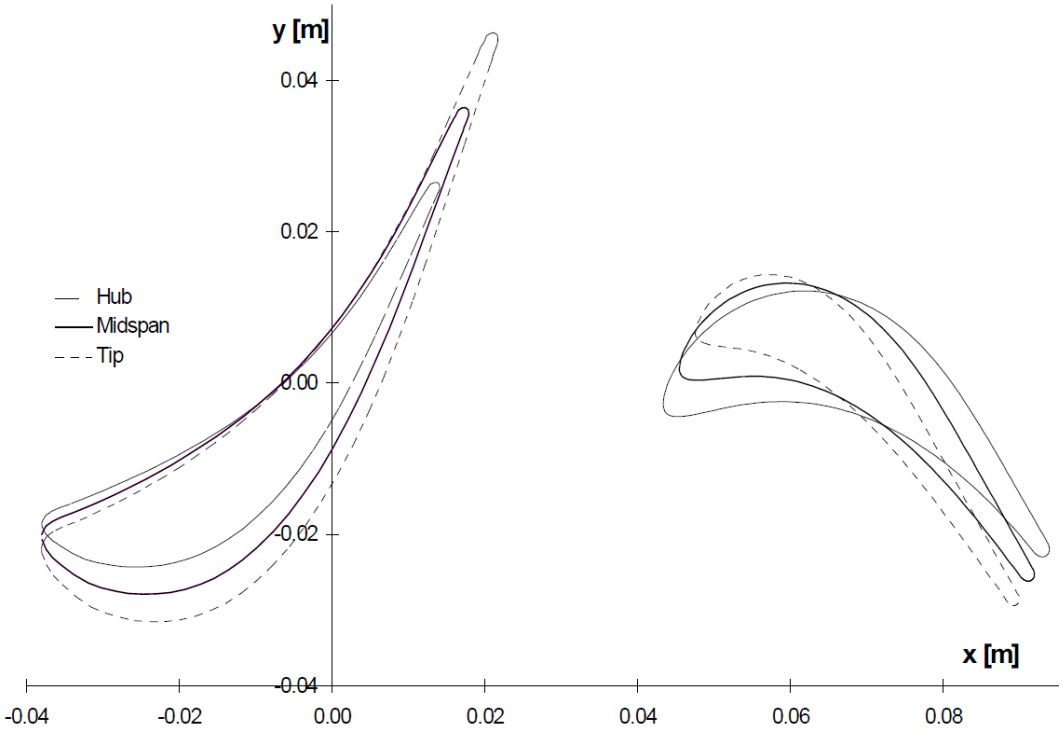

Figure 23: Hub, midspan, tip sections of TTM stage. Courtesy of Erhard [10].

Curiously, the author of this work did not lead any experiment for the final design of the TTM. Instead, a less costly alternative was opted and included a 3D full Euler simulation, a full Navier-Stokes simulation and several quasi-3D Navier-Stokes simulations. Since a real 3D flow simulation

constitutes the main focus of our study, the interest is brought to the results obtained by his 3D full Navier-Stokes simulation.

The setting of the simulation is described as follow : Structured multi-block grids are generated to cover the computational domain which only accounts a portion of the turbine stage (one vane and one blade). The vane and blade profiles represented by Bezier surfaces are enveloped by O-type grids. To improve accuracy of the computed results, the dimensionless wall distance of the first cell on the blade wall is set to 1. Overall, the most appropriate grid employed in the aerodynamic investigation comprises 524000 cells in total.

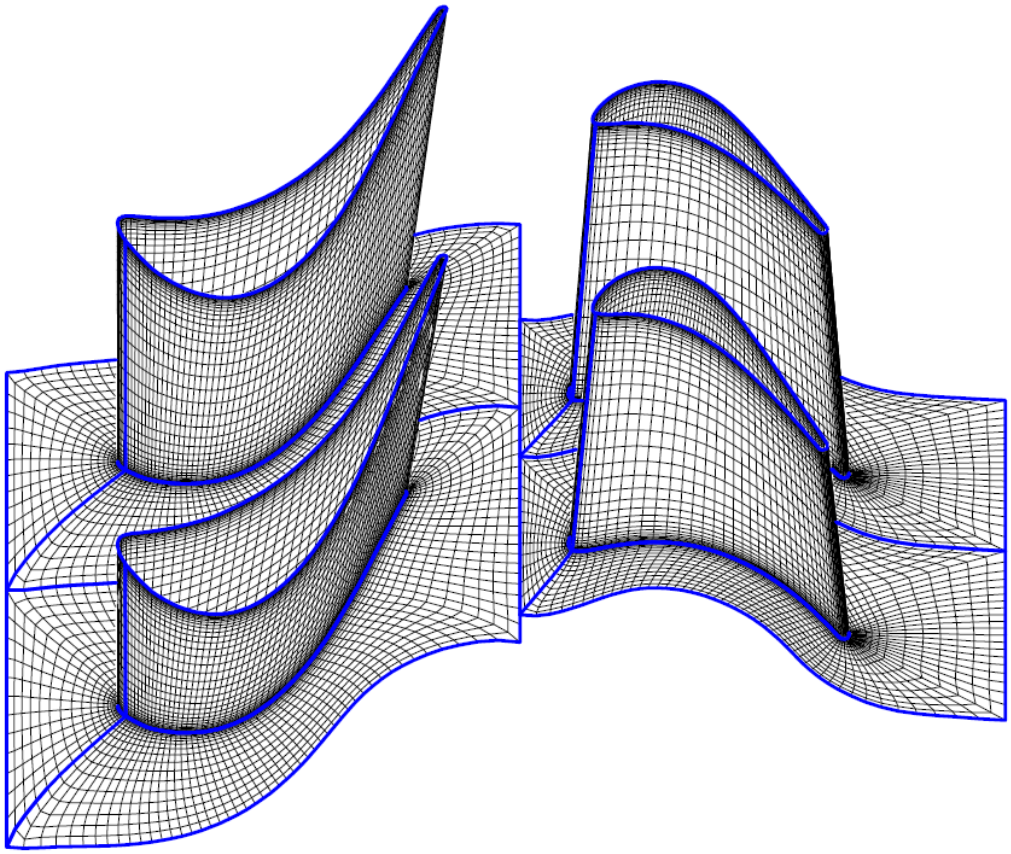

Figure 24: Structured O-type mesh for 3D full Navier-Stokes simulation. Courtesy of Erhard [10].

Now, a steady RANS simulation was run by considering a SA turbulence model coupled with a Newton-Raphson relaxation technique. The optimal configuration tested by Erhard [10] comprises the following boundary conditions and outputs.

Boundary Conditions		Outputs	
$p_{t,A}$ [bar]	3.439	Ω [RPM]	11000
$T_{t,A}$ [K]	454.4	P_w [MW]	1.9
p_C [bar]	1.102	$\dot{m}_t$ [kg/s]	18.24

Table 2: Boundary conditions and outputs of the optimal configuration tested in Erhard [10].

More importantly, the measured Reynolds number for the rotating blade is based on the exhaust velocity and its axial chord in this context and is equal to 1.6×10^6. These boundary conditions will be re-exploited in our CFD simulation described in the following sections.

3 CFD Simulation

This section is dedicated to the CFD simulation and the analysis of its results. It should be emphasized that the main focus of this work is to provide numerical results that are eventually expected to be compared to experimental results obtained from the same operating conditions. For such aim, this part will include the following sections :

1) Blade profiles and Mesh : This section presents the blade profiles involved in this study and the grid that constitutes the computational domain. Basically, the purpose of this section is to deliver an optimal mesh arrangement based on theoretical arguments and computational cost trade off, that can significantly enhance the numerical results.
2) Computational setup : The well-posedness of the problem is crucial for the numerical simulation. At the same time, aerothermal phenomenon that occurs during the optimal operating conditions of the turbine stage, must subsequently be investigated. This section mainly provides the procedure that allows the retrieval of the heat transfer coefficient and presents the computational schemes and algorithms set in the employed solver.
3) Grid independence study : For any CFD analysis, it must come along with a grid independence study which quantifies the spatial error induced by spatial discretization of the problem. For such aim, three different grids were considered and the issued numerical results were compared by the means of the Richardson extrapolation method. At the end, the study delivers the most adequate grid for the simulation.
4) Turbulence model : The choice of the turbulence models is critical for any CFD simulation that involves turbulent flow. Two turbulence models were retained. Notably, the well-used SST model and the rarely-used BSL-RSM model. Their mathematical foundations are revised in order to provide a better understanding of their implication on the reliability of the numerical results. Obviously, advantages and shortcomings are highlighted to justify the choice of the turbulence model.
5) Flow and heat transfer over flat tip blade : Aerothermal analysis is carried out on the results provided by the default flat tip blade. Methodically, the procedure adopted in the analysis is described as follow : Firstly, since the flow regime varies along the span, it would be wise to determine the area affected by possible shock waves. Then comes the aerodynamic investigation that includes many features of the tip leakage flow (e.g. streamlines, blade loading, mass flow rate, etc...). Next, there is the identification of areas on the blade that are exposed to high heat transfer. Lastly, an estimation of the loss related to tip leakage flow is formulated. To get a first insight of the geometrical effect on the flow, a modified blade profile is also considered for this section and comparison of the results is consecutively performed.
6) Flow and heat transfer over double squealer tip blade : Since the purpose of this work is to deliver an improvement on the tip leakage flow. The most classical solution adopted in modern gas turbine engines, consists of including a cavity on the blade tip. For such aim, the previously defined mesh is modified beforehand. Again, to determine the advantages and changes over the tip leakage flow, brought by this tip configuration, the analysis procedure detailed in the previous section is re-employed.

3.1 Turbine blade profiles

Two types of blade profile have been considered in this study in order to assess the impact of geometrical variation on the flow features around the blade tip. The first profile comes obviously from the TTM turbine stage thoroughly described by Erhard [10]. The second profile consists of a slight modification of the former design near the tip. In fact, an inclination of 60 degrees is brought to the mid-chord pressure side rim as it reaches smoothly 0 near both ends.

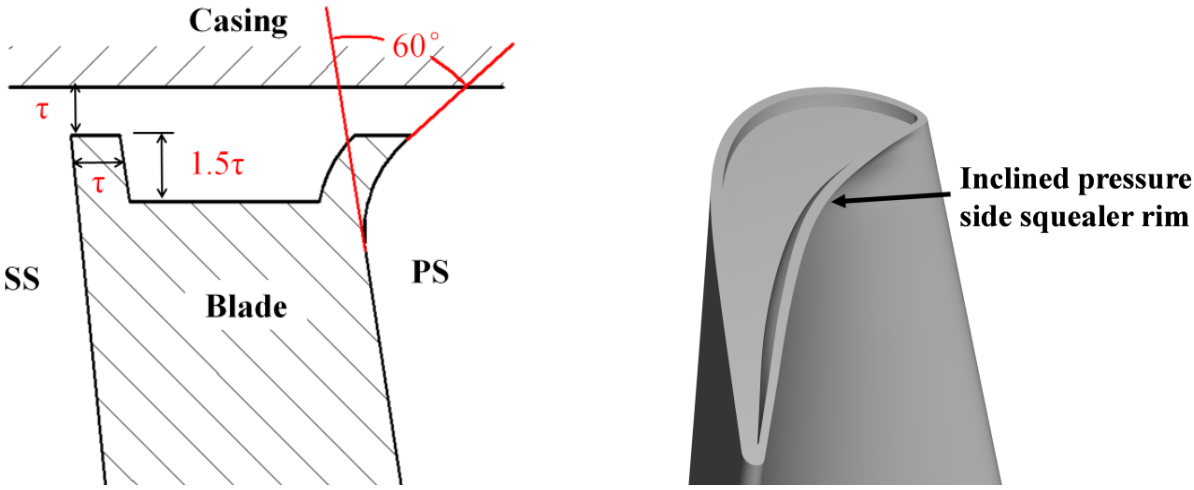

(a) Plane cut at mid-chord. (b) Overall 3D view.

Figure 25: Geometry of the modified design (with cavity included) near the blade tip.

The data related to the geometry of the blade profile were provided as sets of points defining specific cross sections in the spanwise direction. The second profile required an extra manipulation by the means of CAD tools which provided in the same idea the needed sets of points. In either case, the sets of points are interpolated in the spanwise direction to generate the Bezier surfaces shown in Figure 27.

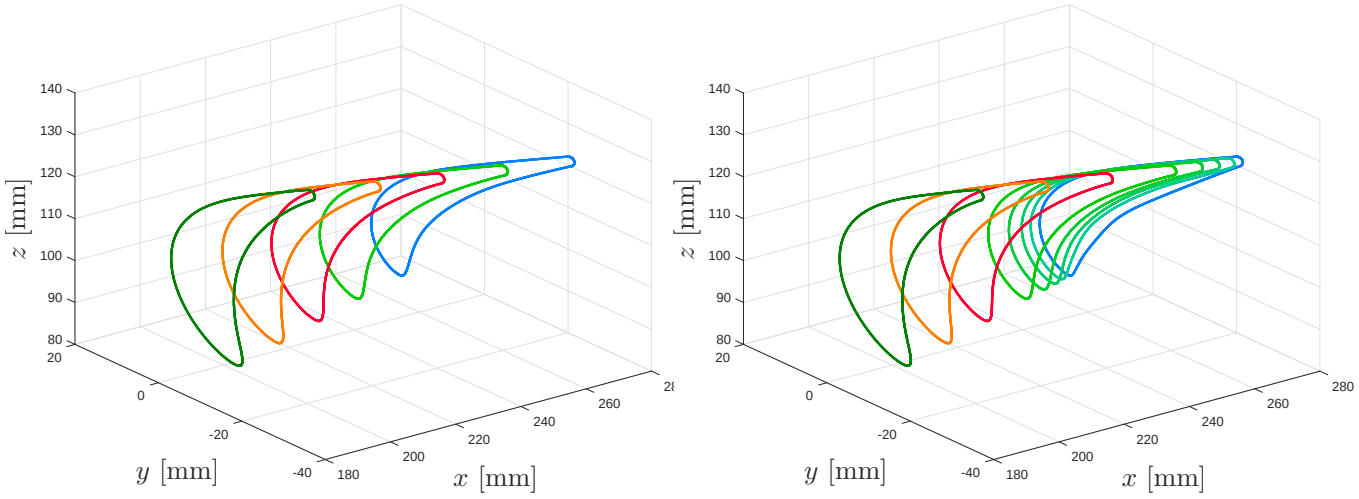

(a) Original. (b) Modified.

Figure 26: Cross sections (with the space coordinates) used to generate the blade surface. Blue line : Tip section. Dark green line : Hub section.

Note that three additional sections have been considered for the modified blade in order to enhance the accuracy of the surface interpolation that must feature the curvature on the pressure side rim as shown in Figure 25a.

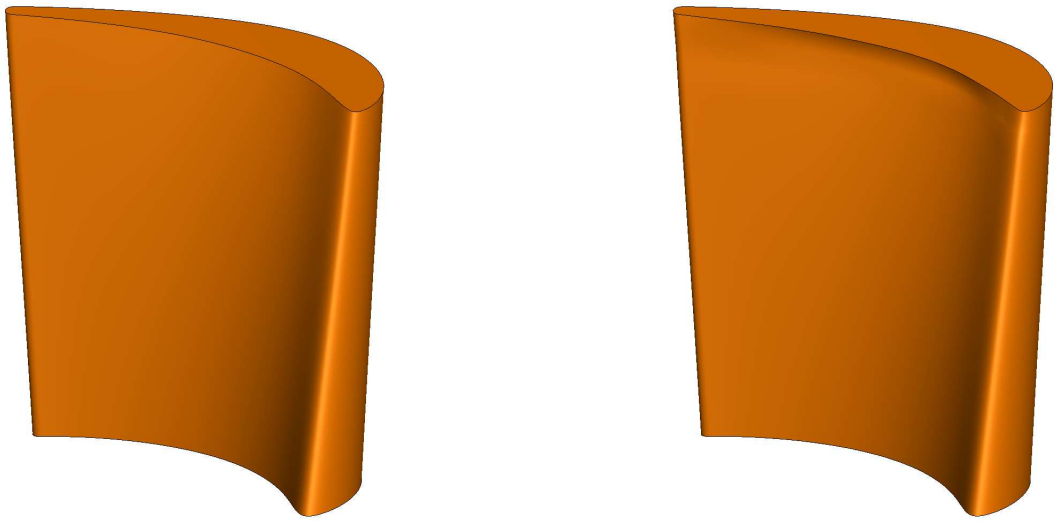

(a) Original. (b) Modified.

Figure 27: Bezier surfaces of the blade profiles.

3.2 Mesh

Once the blade surface has been generated and imported into the commercial grid generator NUMECA AutoGrid5^{TM}. One needs to define the volume of control that reflects the features of the real turbine stage depicted in Figure 22 and that is conveniently bounded by the stations A and C. Thus, these boundaries constitute respectively the inlet and outlet of the computational domain. Additionally, the stator and rotor subdomains are separated by an interface prescribed by the plane B.

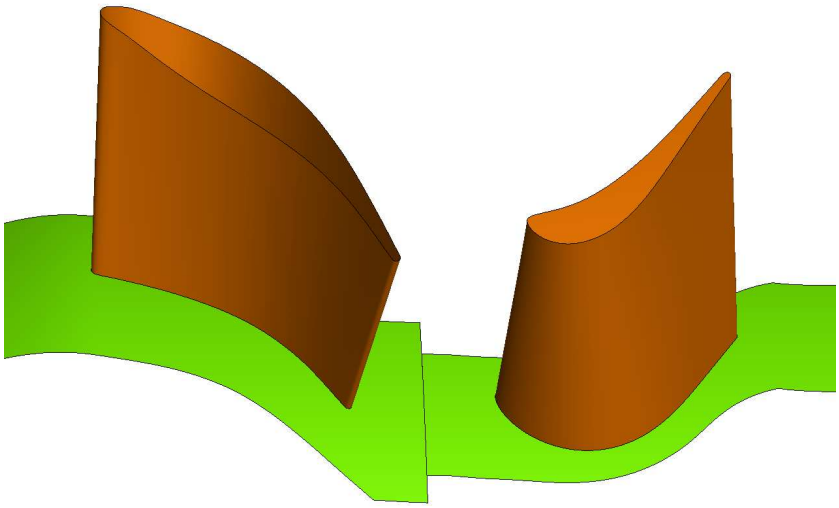

Figure 28: Overall 3D view of the computational domain or control volume.

To reduce considerably the computational cost and to be able to study the local flow, the approach employed by Erhard [10] has been re-exploited, which consists of considering only a portion (one vane and one blade) of the turbine stage as depicted in Figure 28.

The mesh generation requires the prescription of the wall distance y (the width of the first cell close to the blade wall) beforehand. Its estimation is driven by the Blasius equation for turbulent flows

$$y = 6 \left(\frac{V_{ref}}{\nu} \right)^{-\frac{7}{8}} \left(\frac{c}{2} \right)^{\frac{1}{8}} y^{+}. \tag{3.1}$$

Where V_{ref} corresponds rotor row exhaust velocity in this context. The key parameter to fix now is the dimensionless wall distance y^{+}. Menter [27] suggested a y^{+} that ranges between 1 and 5 (which constitutes the low Reynolds number approach) in order to capture the flow in the viscous sub-layer from the aerodynamic point of view. Nevertheless, additional thermal effects imposes further restriction to $y^{+} < 1$. Hence, the most adequate y^{+} is set to 0.7 (equivalently $y = 0.7$ mm) though other values have been tested in the grid refinement study that will be presented later on. By judging the objective of this study, it would be appropriate to apply the low Reynolds approach to the rotor row and allocate most of the computational resources to the blade tip region. On the other hand, the less demanding wall function approach, which employs the log law and which only requires a y^{+} of about 200 (equivalently $y = 200$ mm), is applied to the stator row and to the rotor hub region. Overall, these manipulations allow a better distribution of computational resources and simultaneously improve the results accuracy in the region of interest that is the blade tip region.

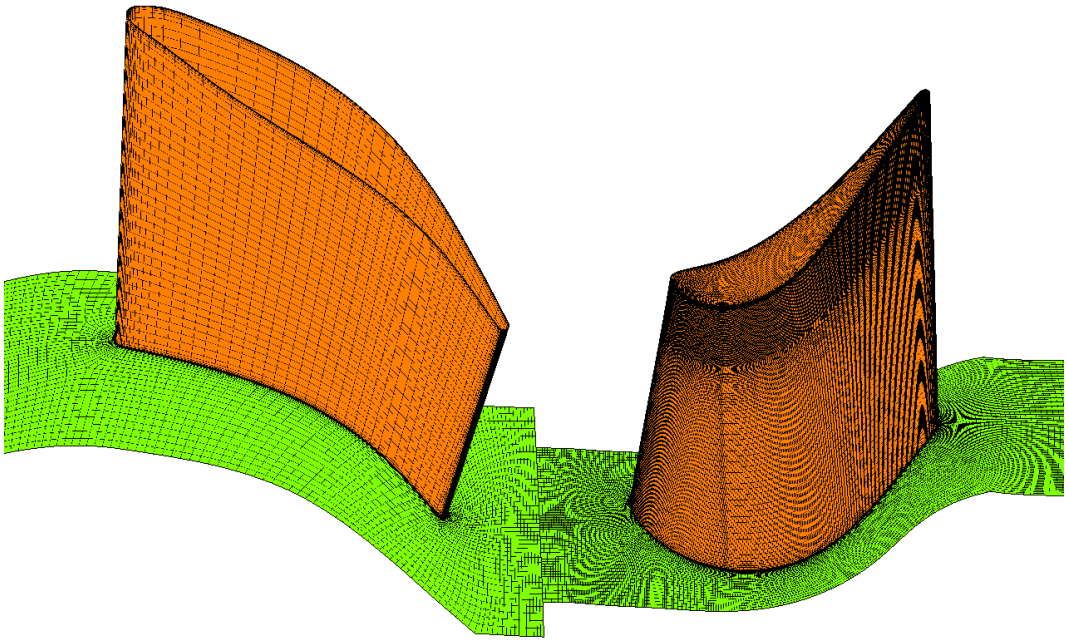

Figure 29: Structured O4H topology used for computational domain.

The mesh configuration, adopted during the mesh generation process, is a O4H topology (four H blocks and one O block). The O block envelops the blade and is simultaneously surrounded by the

four other H blocks as depicted in Figure 30. According to practice guidelines for turbomachinery (with heat transfer predictions included), it is recommended to include 25 cell layers in the skin block, maintain appropriate orthogonality and aspect ratio of the cells close to the walls and set an constant cell expansion ratio of about 1.25 in order to ensure an adequate accuracy of the computed results.

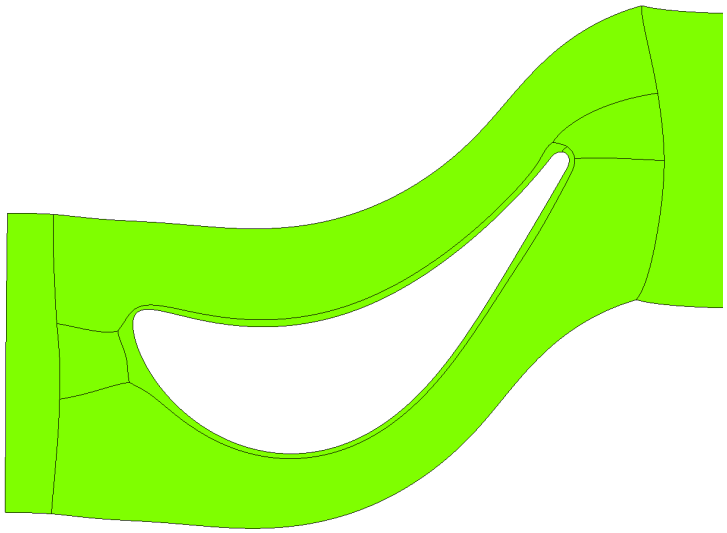

Figure 30: Blade-to-blade view of the structured O4H topology around the blade.

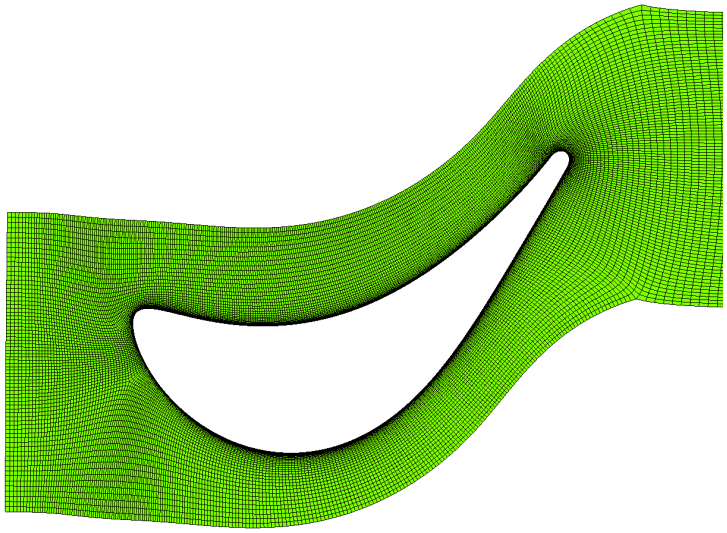

Figure 31: Blade-to-blade view of the structured mesh around the blade.

The mesh generation process carried out in AutoGrid5^{TM} essentially consists of two main steps :

- Setting of the cell distribution in the spanwise/radial direction.
- Definition of a mesh topology around the cross section of the vane/blade, projected in the blade-to-blade plane.

3.3 Computational setup

As already mentioned in the previous section, boundary conditions for the inlet, outlet of the domain and rotational speed of the rotor have been prescribed (by referring to Table 2). Additionally, an inlet turbulence of 5% has been set to agree with the setup found in Erhard [10]. The surfaces on the circumferential sides of the domain are set as rotational periodicity boundary conditions in order to simulate the effect of the multiple blades arrangement. Eventually, no slip boundary conditions are applied to the casing, vane/blade wall. It must be acknowledged that inlet temperature profile is assumed to be spatially uniform although it is not true for a real flow and could considerably affect the nature of the flow. The working fluid which is obviously air is treated as an ideal gas. Note that the initial condition, set at the beginning of each simulation, has a unique purpose to ensure fast convergence to the steady solution and therefore contains the results of the previous simulation.

Since heat transfer prediction is also considered in this study, the wall heat transfer coefficient has to be retrieved at the end of the simulation. By taking into account the considerations made previously, the heat transfer coefficient from Equation 2.26 is given by

$$h_c = \frac{q}{T_{ad} - T_w}. \tag{3.2}$$

For such aim, two different simulations based on the Equation 3.2 are consecutively performed. For the first simulation that omits heat exchange, adiabatic condition (where the heat flux $q_{ad} = 0$) is applied to the walls in order to retrieve the adiabatic temperature field T_{ad} of the parts of interest (blade wall and shroud of the rotor row). For the second simulation, the wall temperature field T_w, imposed to the same parts of interest, is defined as

$$T_w = T_{ad} - 20.$$

Therefore, the denominator of Equation 3.2 is fixed at any location in space and the heat flux q obtained with the second simulation can consequently be retrieved to compute the heat transfer coefficient. Note that slight variations of this approach have thoroughly been used by Han et al. [23] and Krishnababu [28] as well.

Overall, the described simulations are carried out by the means of the commercial CFD software tool ANSYS CFX-12.0 which is a solver based on the FEM. Moreover, since the flow is assumed to be steady, only steady state solutions are considered in this study. The main task of the CFD tool is to solve the compressible RANS equations coupled with the time marching method. Additionally, to improve shock-boundary layer interaction in transonic flow, velocity-pressure coupling is considered by the means of the Rhie Chow algorithm. The spatial and temporal discretizations employ a second order upwind scheme and a second order Euler backward scheme respectively, in order to acquire second order accuracy solution.

For the sake of completeness, the differential form of the compressible Navier-Stokes equations are introduced beforehand in Cartesian coordinates or in stationary frame.
The continuity equation

$$\partial_t \rho + \partial_i \left(\rho u_i\right) = 0. \tag{3.3}$$

By considering a Newtonian fluid and the Stokes hypothesis for the constitutive equation, the stress can directly be related to the fluid viscosity

$$\lambda = -\frac{2}{3}\mu, \qquad \tau_{ij} = \mu\left(\partial_i u_j + \partial_j u_i\right) + \lambda\left(\partial_k u_k\right)\delta_{ij}.$$

The momentum equation

$$\rho\partial_t u_i + \rho u_i \partial_j u_j = -\partial_i p + \mu\left(\partial_{jj} u_i + \frac{1}{3}\partial_i(\partial_k u_k)\right) \tag{3.4}$$

Gravitational forces are usually neglected in turbomachinery flow, thus pressure and shear are the main stresses to consider for this case.
The energy equation in terms of static quantities

$$\rho D_t h = D_t p + k\partial_{ii} T + (\partial_j u_i)\tau_{ij}. \tag{3.5}$$

$D_t p$ and $(\partial_j u_i)\tau_{ij}$ represent respectively the rate of work done by pressure and shear stresses and $k\partial_{ii} T$ characterizes heat transfer by steady conduction within the fluid. Alternatively, it is useful to consider the total quantities for this flow case.
Thus the energy equation in terms of total quantities

$$\rho\partial_t h_t + \rho u_i \partial_i h_t = \partial_t p + k\partial_{ii} T + \partial_i(\tau_{ij} u_j). \tag{3.6}$$

The set of equations have to be completed by the equation of state for an ideal gas

$$p = \rho R T, \tag{3.7}$$

and the constant pressure specific heat capacity equation

$$h = c_p T \quad \text{or} \quad h_t = c_p T_t. \tag{3.8}$$

There are in total 6 equations (Equations 3.3 - 3.8) for 6 unknowns (ρ, p, T, u_i). Hence closure of the system is achieved. In practice, these equations can be solved directly for laminar flows only. However, for real flows that include turbulence, direct resolution can become cumbersome. Therefore, a less demanding averaging approach applied to these equations is proposed below.

Alternatively, the differential form of the compressible Navier-Stokes equations expressed in cylindrical coordinates or in rotating frame are equally important since they are used to determine the additional forces caused by the rotation motion. By re-exploiting the velocity triangle, a relation analogous to Equation 2.1 is obtained

$$u_i = w_i + \epsilon_{ijk}\Omega_j r_k. \tag{3.9}$$

Where the absolute velocity can again be related to the relative and entrainment velocities.
The continuity equation

$$\partial\rho + \partial_i(\rho w_i) = 0. \tag{3.10}$$

The continuity equation is invariant to the entrainment velocity and is written as a function of the relative velocity instead.
In the rotating frame, the stress tensor can be re-expressed as a function of the relative velocity as well

$$\tau_{ij} = \mu\left(\partial_i w_j + \partial_j w_i\right) + \lambda\left(\partial_k w_k\right)\delta_{ij}.$$

The momentum equation

$$\rho\partial_t w_i + \rho w_i \partial_j w_j = -\partial_i p + \mu\left(\partial_{jj} w_i + \frac{1}{3}\partial_i(\partial_k w_k)\right) - \rho\epsilon_{ijk}\Omega_j(\epsilon_{klm}\Omega_l r_m) - 2\rho\epsilon_{ijk}\Omega_j w_k. \tag{3.11}$$

The two last terms represent respectively the centrifugal and Coriolis forces.
The energy equation

$$\rho D_t I_t = \partial_t p + k\partial_{ii} T + \partial_i(\tau_{ij} w_j). \tag{3.12}$$

With the rothalpy which includes the total enthalpy and measures the total energy content in a steadily rotating frame

$$I_t = h + \frac{w_i^2}{2} - \frac{u_i^2}{2}.$$

Unlike the momentum equation, the Coriolis and centrifugal forces does not contribute to the energy balance of the flow. Overall, the presence of these two forces does not fundamentally alter the equations since they are seen as additional forces to consider. Moreover, this clear distinction associated to the frames suggests that use of relative quantities is more appropriate for the study of the flow mechanism and interaction in the rotor row.

As mentioned above, solving directly these equations, which is equivalent to performing a DNS, would consume a drastic amount of computational effort and time. Consequently, a less CPU resources consuming alternative is adopted instead. The approach consists of a statistical representation of turbulence by defining the average properties of the flow of interest. The main variables that undergo modelling are ρ, p, T, u_i and are decomposed into the averaged and fluctuating components

$$u_i = \overline{u}_i + u_i', \qquad p = \overline{p} + p', \qquad T = \overline{T} + T', \qquad \rho = \overline{\rho} + \rho'.$$

For compressible flow, a fluctuation associated to the density exists and leads to Favre-averaged Navier-Stokes equations used in the solver. However, its consideration severely complicates the averaging process of the equations highlighted hereby, thus the density fluctuation ρ' is handily assumed to be negligible. The averaging procedure introduces additional unknowns containing products of fluctuating quantities during the computation, which implies that additional equations have to be envisaged to achieve closure of the modelled system. For the steady simulation, the time averaged or Reynolds averaged quantities are defined as

$$\overline{u}_i = \frac{1}{\Delta t}\int_t^{t+\Delta t} u_i d\tau$$

The Reynolds averaged continuity equation

$$\partial_t \rho + \partial_i \rho \overline{u}_i = 0. \tag{3.13}$$

The Reynolds averaged momentum equation for the mean flow

$$\partial_t \rho \overline{u}_i + \partial_j(\rho \overline{u}_i \overline{u}_j) = -\partial_i \overline{p} + \partial_j(\overline{\tau}_{ij} - \rho\overline{u_i' u_j'}). \tag{3.14}$$

Where the averaged stress tensor is written as

$$\overline{\tau}_{ij} = \mu\left(\partial_i \overline{u}_j + \partial_j \overline{u}_i\right) + \lambda\left(\partial_k \overline{u}_k\right)\delta_{ij}.$$

The Reynolds stress $\rho\overline{u_i' u_j'}$ analogous to viscous stress arises from the nonlinear convective term and shows that velocity fluctuations is responsible for enhanced flow mixing in a turbulent regime.
The Reynolds averaged energy equation for the mean flow

$$\partial_t \rho \overline{h}_t + \partial_i(\rho \overline{u}_i \overline{h}_t) = \partial_t \overline{p} + k\partial_{ii}\overline{T} - \partial_i(\rho\overline{u_i' h'}) + \partial_j[\overline{u}_i(\overline{\tau}_{ij} - \rho\overline{u_i' u_j'})]. \tag{3.15}$$

Where the averaged total enthalpy and turbulent kinetic energy are defined as

$$\overline{h}_t = \overline{h} + \frac{1}{2}\overline{u}_i^2 + k', \qquad k' = \frac{1}{2}\overline{(u_i')^2}.$$

In the same order of idea, an additional turbulent heat flux $\rho\overline{u_i' h'}$ results from the averaging procedure and is analogous to the molecular heat flux observed in laminar flow. The last term $\partial_j[\overline{u}_i(\overline{\tau}_{ij} - \rho\overline{u_i' u_j'})]$ represents the work rate due to viscosity (molecular and turbulent). Again, there are in total 6 equations (Equations 3.13 - 3.15), along with the equations of state, for 15 unknowns (ρ, $\overline{p}$, $\overline{T}$, $\overline{u}_i$, $\overline{u_i' u_j'}$, $\overline{u_i' h'}$). Closure of the problem is not achieved and consequently further modelling is required. The turbulence models considered in this study will be analysed and compared in the subsequent section.

3.4 Grid independence study

For any type of CFD simulation, the assessment of the numerical error introduced by spatial discretization plays an important role since it conditions the accuracy and convergence of the solution. In order to quantify the numerical error, three meshes (from coarse to refined) have been defined and the varying parameter retained for the grid independence study is the dimensionless wall distance y^+ adjacent to the rotor blade wall. At the end of the simulations, two variables, namely the total tip leakage mass flow rate $\dot{m}_l$ and the area-averaged wall heat transfer coefficient $h_{c,av}$, are retrieved for further analysis. Note that the default turbulence model used in this study is the SST model since the latter is the most commonly employed for turbomachinery flow. The advantages and drawbacks of this model will be discussed in the next section.

	Mesh 1	Mesh 2	Mesh 3
Wall distance y^+ [-]	1.15	0.9	0.7
Number of elements (10^6)	7.49	8.08	8.67
Area-averaged heat transfer coefficient $h_{c,av}$ [W/m^{2}K] (10^3)	1.273	1.2703	1.2683
Total leakage mass flow rate $\dot{m}_l$ [kg/s] (10^{-2})	1.539	1.526	1.517

Table 3: Resolution and results of the meshes retained for grid independence study.

Small variation of the retained quantities effectively shows that grid resolution plays an important role in the numerical computation. Nonetheless, convergence of these quantities still needs to be proven in order to determine the adequate mesh resolution that ensures a good comprise between computational resources and accuracy of the solution.

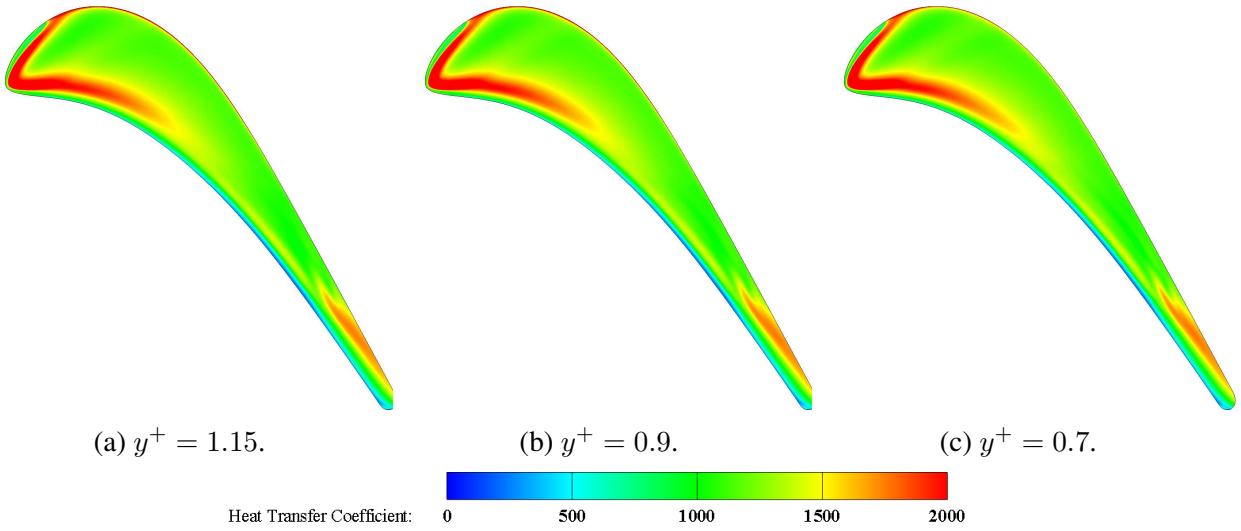

(a) $y^+ = 1.15$. (b) $y^+ = 0.9$. (c) $y^+ = 0.7$.

Figure 32: Heat transfer coefficient h_c over the blade tip for different grid resolution.

Clear distinction is qualitatively not noticeable from the contours exhibited by Figure 32. Though, heat transfer properties are supposed to be more sensitive to grid resolution. On the other hand, the aerodynamic properties distribution along the blade chord shows little local variations which are highlighted in Figure 33. These features gathered together suggest that the tested grids are well conditioned and induce slight numerical errors.

The method employed to estimate the spatial error is based on the Richardson extrapolation from Roache et al. [31]. Note that this method has notably been used for the same purpose by the authors Yang [39] and Zhou [40].

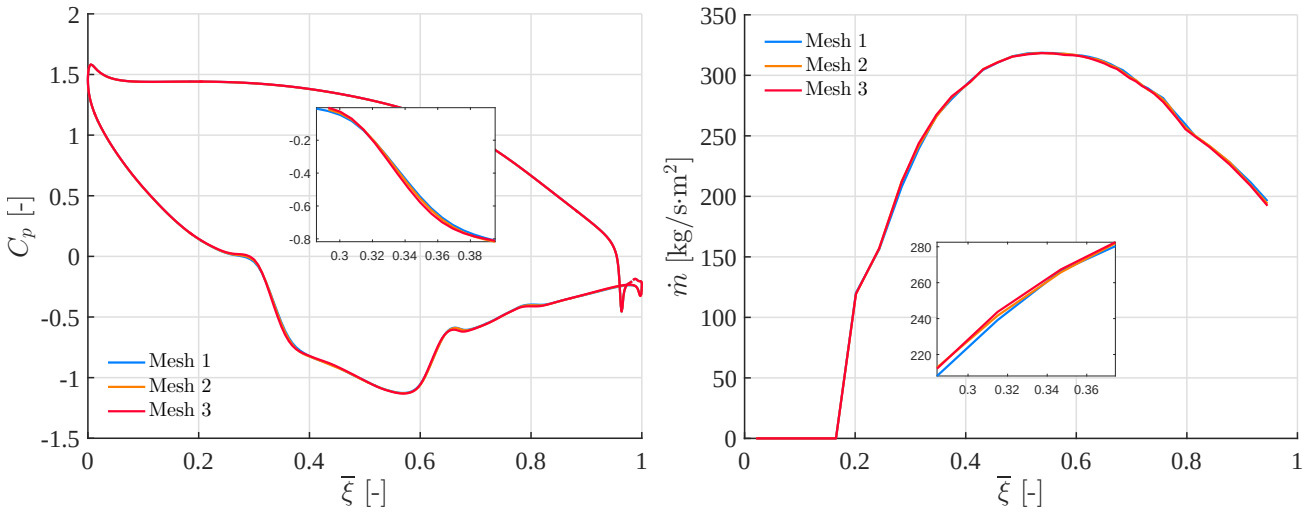

(a) Pressure coefficient distribution at 95% span.

(b) Tip leakage mass flow rate per area.

Figure 33: Streamwise distribution of the aerodynamic properties for different grid resolution.

Firstly, the procedure requires a theoretical order of convergence of the different grids, which is given by

$$p_o = \ln\left(\frac{f_1 - f_2}{f_2 - f_3}\right) / \ln r_o. \tag{3.16}$$

Where the constant grid refinement ratio is estimated to

$$r_o = y_1^+ / y_2^+ \cong y_2^+ / y_3^+ \cong 1.28.$$

Note that the order of spatial convergence can not be greater than 2, it means that second order accuracy is the most ideal situation that could occur for this study. The variables f_1, f_2 and f_3 represent the variables of interest ($\dot{m}_{l,av}$ or $h_{c,av}$) from different grids. The greatest advantage of the Richardson extrapolation is that it can provide a hypothetical exact value of the quantity of interest for a zero grid spacing, which is obtained via the expression

$$f_0 \cong f_3 + \frac{f_3 - f_2}{r_o^{p_o} - 1}. \tag{3.17}$$

Nevertheless, this relation is only valid if the variables were in the asymptotic range of convergence (close to the exact solution f_0). Therefore, a grid convergence index is adopted to determine the relative error and whether or not the solution converges with a safety factor $F_S = 1.25$

$$\text{GCI}_{12} = F_S \left|\frac{f_1 - f_2}{f_2}\right| / (r_o^{p_o} - 1) \qquad \text{and} \qquad \text{GCI}_{23} = F_S \left|\frac{f_2 - f_3}{f_3}\right| / (r_o^{p_o} - 1) \tag{3.18}$$

They both have to verify the following relation

$$\iota_{\text{GCI}} = \frac{\text{GCI}_{12}}{r_o^{p_o} \text{GCI}_{23}} \tag{3.19}$$

If the parameter is equal to approximatively 1, then one can state that the variables are located within the asymptotic range of convergence.

According to the results gathered in Table 4, one can state that both quantities exhibit different degree of sensitivity with respect to the grid resolution. In fact, the slightly greater order of convergence of $\dot{m}_l$ allows theoretically a faster convergence. However, the correspondent relative error is approximatively three times the one obtained with $h_{c,av}$. Consequently, it implies that further grid refinement can significantly reduce the numerical error related to the leakage mass flow rate, whereas only small changes are noticeable for the heat transfer coefficient. In sum, the solutions of the grids are located within the asymptotic range of convergence.

Quantities of interest	$h_{c,av}$	$\dot{m}_l$
Order of convergence p_o [-]	1.22	1.49
Exact solution f_0 [W/m^{2}K](10^3) or [kg/s](10^{-2})	1.2626	1.497
Constant parameter C_{GC} [-]	8.8076	0.00034
Grid convergence indice GCI_{12} [%]	0.756	2.395
Grid convergence indice GCI_{23} [%]	0.5609	1.668
Grid convergence parameter ι_{GCI} [-]	0.9974	0.994

Table 4: Results of the Richardson extrapolation method for grid independence study.

Now, with the previous data, the absolute error can be plotted graphically with

$$E_{\text{GC}} = f(y^+) - f_0 = C_{\text{GC}}(y^+)^{p_o}, \quad \text{or} \quad \ln(E_{\text{GC}}) = \ln(C_{\text{GC}}) + p_o \ln(y^+). \tag{3.20}$$

Where the slope of the straight segments reflects the order of convergence of the respective quantities.

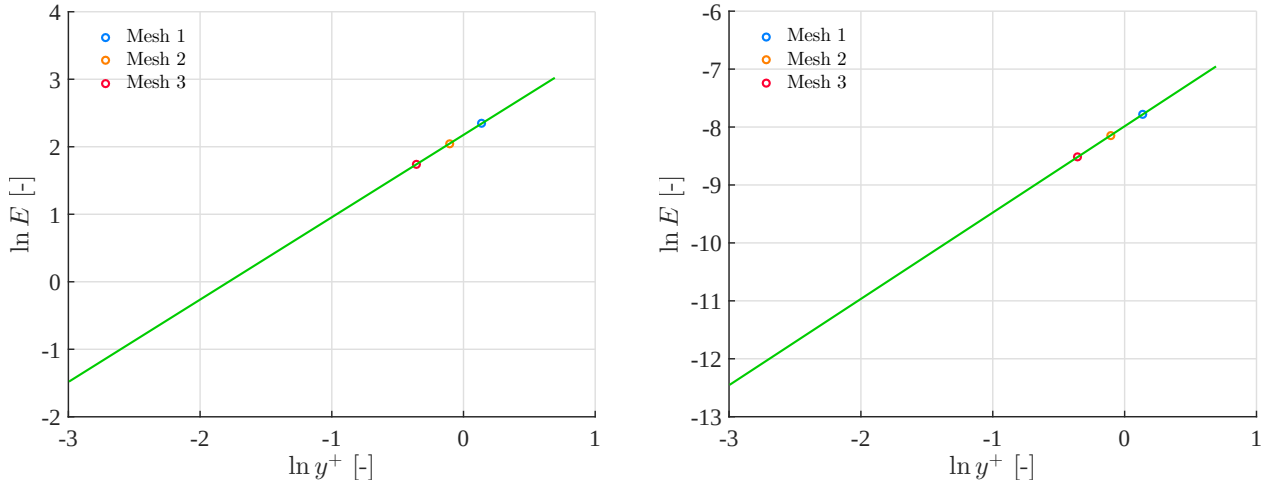

(a) Area-averaged heat transfer coefficient.

(b) Total tip leakage mass flow rate.

Figure 34: Logarithmic plots of the absolute error of the quantities of interest.

Finally, one has proven that improvement given to the third mesh yields the most accurate results in this grid convergence study. On the other hand, this mesh arrangement also constitutes a satisfactory trade off between computational effort and quality of the solution. Therefore, the third mesh will be retained for the rest of the study.

Nevertheless, it is also at this stage of this study that the major drawbacks of the Richardson extrapolation method is outlined. Unlike the authors cited above, that have also applied this method for only one quantity of interest. Two quantities have essentially been retained to assess its reliability. As a result, the grid resolutions differ with respect to the analysed quantity. For example, the most striking difference comes from the order of convergence of the grids. Moreover, it should be emphasized that the method assumes spatial convergence of the grids beforehand, otherwise it would fall apart if an unexpected value is encountered. Fortunately, the retained grids were well conditioned from the start, so failure of the method was avoided. Conclusively, the Richardson extrapolation method is able to deliver satisfactory results only if the problem is well-posed from the beginning. Otherwise its sensitivity to numerical values of the solution provided by the tested grids may cause significant inconsistencies and also exhibit a lack of robustness.

3.5 Turbulence model

Two turbulence models, that provide additional equations to complete the RANS equations closure problem mentioned earlier, are retained for this study, namely the SST and the BSL-RSM models. Authors like Kline et al [33], Marvin [34] and Lakshminarayana [35] have thoroughly reviewed the state of art of turbulence modelling and computation for several flow cases including turbomachinery flow. The first model, designated as a two equation turbulence model, is evidently based on the Boussinesq isotropic eddy viscosity assumption written as

$$-\rho\overline{u_i'u_j'} = \mu_t(\partial_i\overline{u}_j + \partial_j\overline{u}_i) - \frac{2}{3}\delta_{ij}(\rho k' + \mu_t\partial_k\overline{u}_k). \tag{3.21}$$

Note that there are no mathematical foundations that can validate the relationship between the Reynolds stress tensor and the averaged strain rate by the means of an isotropic eddy viscosity. Nevertheless, this hypothesis assumes that the turbulent fluctuations contribute to the momentum and heat diffusion in a way analogous to the molecular diffusion, although it should be emphasized that eddy viscosity is actually a property of the flow and on the counterpart molecular viscosity is a property of the fluid. Analogously, the isotropic eddy diffusivity assumption for the Reynolds heat flux is written as

$$-\rho\overline{u_i'h'} = \frac{\mu_t}{Pr_t}\partial_i\overline{h}. \tag{3.22}$$

This expression results from the consideration made in Equation 2.27. As one knows, the coupling of the momentum and heat transfer for turbulent flows requires the definition of the eddy viscosity and the turbulent Prandtl number

$$\mu_t = \rho\frac{k'}{\omega'}, \qquad Pr_t = c_p\frac{\mu_t}{k_t}.$$

μ_t is clearly defined as a scalar and is deliberately expressed as a function of the turbulent kinetic energy and specific dissipation rate in this context. The turbulent Prandtl number Pr_t introduces the eddy thermal conductivity k_t which is used in the same order of idea as the eddy viscosity. Unlike the molecular Prandtl number Pr, its turbulent counterpart is held constant and at the same time, an assumption has to be made on the nature of velocity-temperature fields coupling in turbulent flows. Again, if one assumes an ideal condition where $Pr_t = 1$ (not usually met), this implies a same mixing length for both momentum and energy transfers. Note that the physical interpretation of Pr_t through its definition highly depends on the validity of the isotropic eddy viscosity concept for this 3D flow. In the worst case where the concept is not applicable, the turbulent Prandtl number could become meaningless. Durbin [4] suggests a $Pr_t = 0.9$ for boundary layer flow, a $Pr_t = 0.7$ for free shear layer flow and $Pr_t = 0.85$ for generalized flows. According to the dimensional analysis, the eddy viscosity relies on to the properties of anisotropic large eddies which carry most of the produced turbulent kinetic energy and is characterised by the time scale $T_l = k'/\epsilon'$, although every length scale should basically be retained for turbulent diffusion. Additionally, the formulation suggests that energy production and dissipation are of the same order of magnitude at high Reynolds number. The conclusion actually raises a disagreement over the interpretation of the isotropic eddy viscosity and incontestably of the Boussinesq assumption which ultimately results in isotropic turbulent flow.

The substitution of Equations 3.21 and 3.22 in the RANS Equations 3.14 and 3.15 for the mean flow yields

$$\partial_t\rho\overline{u}_i + \partial_j(\rho\overline{u}_i\overline{u}_j) = -\partial_i p_m + \partial_j[\mu_m(\partial_j\overline{u}_i + \partial_i\overline{u}_j)], \tag{3.23}$$

$$\partial_t\rho\overline{h}_t + \partial_i(\rho\overline{u}_i\overline{h}_t) = \partial_t\overline{p} + k\partial_{ii}\overline{T} + \partial_i\left(\frac{\mu_t}{Pr_t}\partial_i\overline{h}\right) + \partial_j\left[\overline{u}_i\left(\overline{\tau}_{ij} + \mu_t(\partial_i\overline{u}_j + \partial_j\overline{u}_i) - \frac{2}{3}\delta_{ij}(\rho k' + \mu_t\partial_k\overline{u}_k)\right)\right]. \tag{3.24}$$

Where the modified viscosity and pressure are defined as

$$\mu_m = \mu + \mu_t, \qquad p_m = \overline{p} + \frac{2}{3}\rho k' + \frac{2}{3}\mu_m \partial_k \overline{u}_k.$$

Authors like Krishnababu [29] and Lavagnoli [30] recommended the SST model as a standard turbulence model for turbomachinery flow. The SST model can in fact deliver a fair solution accuracy from the engineering perspective but may still lack capabilities to predict some essential features of the 3D complex flow. The latter includes the rotating motion of the flow (redistribution of energy) or the effect of the curvature (shape of the blade) according to Lakshminarayana [8]. These constitute the very reason why the BSL-RSM model is also retained for this study.

Until this step, this turbulence model has provided 9 additional equations but has concurrently introduced 2 additional unknowns, namely k' and ω'. To complete the system, two transport equations related to these unknowns have to be taken into account. It should be acknowledged that the SST model is an improvement of the $k-\omega$ model formulated by Wilcox [32]. Though the $k-\omega$ model is suitable for boundary layer flows, its main shortcoming results from its sensitivity to free-stream conditions, notably its strong dependence on the inlet BC. On the other hand, the counterpart $k-\epsilon$ model does not exhibit this shortcoming but fails in the near wall region. Thus, the enhancement brought by the SST model is a blending approach that covers the drawbacks and highlights the advantages of both models as formulated by Menter [37]. Additionally, another shortcomings of the two equation model are the overestimation of the turbulent kinetic energy production at stagnation points and the inability to predict correctly flow separation, the most effective correction to this issue is the establishment of a limiter in the transport equations. From the mathematical perspective, the enhancements are brought under the form of blending functions affected to different terms of the transport equations and they can be interpreted as switches that allow smooth transition from one model to the other in the region of interest. Firstly, the transport equations for $k-\omega$ model are respectively

$$\partial_t \rho k' + \partial_i(\rho \overline{u}_i k') = \partial_i \left[\left(\mu + \frac{\mu_t}{\sigma_{k1'}} \right) \partial_i k' \right] + P_{k'} - \beta_{k'} \rho k' \omega'. \tag{3.25}$$

Where the production rate of turbulent kinetic energy is defined as

$$P_{k'} = \mu_t(\partial_j \overline{u}_i + \partial_i \overline{u}_j)\partial_j \overline{u}_i - \frac{2}{3}\partial_k \overline{u}_k(3\mu_t \partial_k \overline{u}_k + \rho k').$$

Note that the values of the empirical constants that will appear subsequently can be found in the CFX solver theory guide. The terms at the RHS of Equation 3.25 represents respectively diffusion, production and dissipation of the turbulent kinetic energy. The diffusion $\partial_i \left[\left(\mu + \frac{\mu_t}{\sigma_{k1'}} \right) \partial_i k' \right]$ is caused by pressure and velocity fluctuations and viscous stresses, the production P'_k involves energy transfer from the mean flow to turbulence, the term $\beta_{k'} \rho k' \omega'$ is responsible for the dissipation of the turbulent kinetic energy by viscosity that normally occurs at small scales.

$$\partial_t \rho \omega' + \partial_i(\rho \overline{u}_i \omega') = \partial_i \left[\left(\mu + \frac{\mu_t}{\sigma_{\omega 1'}} \right) \partial_i \omega' \right] + \alpha_{\omega 1'} \frac{\omega'}{k'} P_{k'} - \beta_{\omega 1'} \rho \omega'^2. \tag{3.26}$$

In the same order of idea, the terms on the RHS represents respectively the diffusion, production and viscous destruction. Then, the transformed transport equations for $k-\epsilon$ model with the specific dissipation rate are

$$\partial_t \rho k' + \partial_i(\rho \overline{u}_i k') = \partial_i \left[\left(\mu + \frac{\mu_t}{\sigma_{k2'}} \right) \partial_i k' \right] + P_{k'} - \beta_{k'} \rho k' \omega', \tag{3.27}$$

$$\partial_t \rho \omega' + \partial_i(\rho \overline{u}_i \omega') = \partial_i \left[\left(\mu + \frac{\mu_t}{\sigma_{\omega 2'}} \right) \partial_i \omega' \right] + \alpha_{\omega 2'} \frac{\omega'}{k'} P_{k'} - \beta_{\omega 2'} \rho \omega'^2 + 2\rho \frac{1}{\sigma_{\omega 2' \omega'}} \partial_i k' \partial_i \omega'. \tag{3.28}$$

Equations 3.25 and 3.26 are multiplied by the function F_{bsl} whereas Equations 3.27 and 3.28 are multiplied by the difference $1 - F_{bsl}$. Eventually, their sum yields the transport equations of the SST model

$$\partial_t \rho k' + \partial_i(\rho \overline{u}_i k') = \partial_i \left[\left(\mu + \frac{\mu_t}{\sigma_{k3'}} \right) \partial_i k' \right] + P_{k'} - \beta_{k'} \rho k' \omega', \tag{3.29}$$

$$\partial_t \rho \omega' + \partial_i(\rho \overline{u}_i \omega') = \partial_i \left[\left(\mu + \frac{\mu_t}{\sigma_{\omega 3'}} \right) \partial_i \omega' \right] + \alpha_{\omega 3'} \frac{\omega'}{k'} P_{k'} - \beta_{\omega 3'} \rho \omega'^2 + (1 - F_{bsl}) 2\rho \frac{1}{\sigma_{\omega 2' \omega'}} \partial_i k' \partial_i \omega'. \tag{3.30}$$

The constants present in Equations 3.29 and 3.30 are defined as a linear combination, e.g.

$$\sigma_{k3'} = F_{bsl} \sigma_{k1'} + (1 - F_{bsl}) \sigma_{k2'}.$$

In the near wall region (e.g. boundary layer), the $k - \omega$ model is recovered since $F_{bsl} = 1$; in the far field region, the $k - \epsilon$ model is activated with $F_{bsl} = 0$. Nonetheless, the eddy viscosity modified by the SST model limiter, the turbulent kinetic energy production limiter and the invariant measure of the averaged strain rate, all formulated by Menter [38], are given by

$$\mu_t = \rho \frac{a_t k'}{\max(a_t \omega', S_m F_{sst})}, \qquad P_k = \min(P_k, C_{lim} \rho \epsilon'), \qquad S_m = \sqrt{2 \overline{S}_{ij} \overline{S}_{ij}}.$$

In the same vein, $F_{sst} = 1$ in the inner boundary layer and $F_{sst} = 0$ elsewhere. With the two additional transport equations, the closure problem is therefore complete. The last feature of the two equation model to mention is the values adopted by the empirical parameters from Equations 3.29 and 3.30. Theoretically, the values are determined by the means of measurements carried out on canonical flows (e.g. 2D shear flow, planar jet, etc...) and can eventually be modified according to the user's requirements. This implies that there is a large degree of freedom associated to the setting of these parameters and that the two equation model is actually very flexible. In fact, many research centres (e.g. NASA, ESA, etc...) possess charts that can provide the most adequate values to implement in the CFD solver and acquire simulation results that agrees perfectly with the experimental results for a specific flow. Unfortunately, these data are not available to the public and the standard empirical constants found in the commercial solver CFX are supposed to suit a large set of flows.

According to the discussion led above about the foundations of the isotropic eddy viscosity, it has become evident that this assumption might be too crude especially for turbomachinery flows, as mentioned by Rodi [36]. Therefore, the alternative is to treat the RANS equations with less restrictive assumptions, which is the purpose of the RSM. This model has aroused growing interests in the domain of turbomachinery flow in these recent years since it treats the complex flow in a more complete manner. The procedure abandons the Boussinesq assumption of Equation 3.21 and affects a transport equation for each independent component of the Reynolds stress tensors only. The compressible RANS equations can be rewritten in this case as

$$\partial_t \rho \overline{u}_i + \partial_j(\rho \overline{u}_i \overline{u}_j) = -\partial_i p_m + \partial_j[\mu(\partial_j \overline{u}_i + \partial_i \overline{u}_j)] - \partial_j(\rho \overline{u'_i u'_j}), \tag{3.31}$$

$$\partial_t \rho \overline{h}_t + \partial_i(\rho \overline{u}_i \overline{h}_t) = \partial_t \overline{p} + k \partial_{ii} \overline{T} + \partial_i \left(\frac{\mu_t}{Pr_t} \partial_i \overline{h} \right) + \partial_j \left[\overline{u}_i (\overline{\tau}_{ij} - \rho \overline{u'_i u'_j}) \right]. \tag{3.32}$$

With the modified pressure that omits any turbulence contribution

$$p_m = p + \frac{2}{3} \mu \partial_k \overline{u}_k.$$

It should be emphasized that the RSM does not bring any modification to the Reynolds heat flux, so the latter still employs the isotropic eddy diffusivity assumption although anisotropic features are

added by the means of viscous work term. The transport equation for each individual component of the Reynolds stress tensor is given by

$$\partial_t \rho\overline{u_i' u_j'} + \partial_k(\overline{u}_k \rho\overline{u_i' u_j'}) = P_{ij} - \frac{2}{3}\beta_{k'}\rho k'\omega'\delta_{ij} + D_{ij} + \partial_k\left[\left(\mu + \frac{\mu_t}{\sigma_{k1'}}\right)\partial_k\overline{u_i' u_j'}\right]. \tag{3.33}$$

Note that the isotropic eddy viscosity is re-employed in Equations 3.32 and 3.33 and is still defined as a scalar. The production terms and the trace are defined as

$$P_{ij} = -\rho\overline{u_i' u_k'}\partial_k\overline{u}_j - \rho\overline{u_j' u_k'}\partial_k\overline{u}_i, \qquad E_{ij} = -\rho\overline{u_i' u_k'}\partial_j\overline{u}_k - \rho\overline{u_j' u_k'}\partial_i\overline{u}_k, \qquad P = \frac{1}{2}P_{kk}.$$

Which are included in the redistribution term or pressure strain correlation modelled as

$$D_{ij} = \beta_{k'}C_1\rho\omega'\left(-\overline{u_i' u_j'} + \frac{2}{3}k\delta_{ij}\right) - \hat{a}\left(P_{ij} - \frac{2}{3}P\delta_{ij}\right) - \hat{b}\left(E_{ij} - \frac{2}{3}P\delta_{ij}\right) - \hat{c}\rho k'\left(\overline{S}_{ij} - \frac{1}{3}\overline{S}_{kk}\delta_{ij}\right).$$

This term is made of the so-called slow and rapid contributions. Slow terms omit any velocity gradients whereas their counterparts, the rapid terms involve velocity gradients. Their distinction initially arises from their respective purpose. Consecutively, rapid terms cause instantaneous changes whereas the slow terms affects the mean flow in the long run. Nonetheless, it is possible to isolate the slow terms, the velocity gradients are set to 0 and all the production terms and averaged strain terms are dropped. This manipulation implies that the anisotropic turbulent flow is not fuelled anymore and starts to decay progressively, leaving the return-to-isotropy term

$$D_{ij} = \beta_{k'}C_1\rho\omega'\left(-\overline{u_i' u_j'} + \frac{2}{3}k\delta_{ij}\right).$$

This corresponds to the linear relaxation of the anisotropic tensor that slowly drives $\overline{u_i' u_j'}$ towards $\frac{2}{3}k\delta_{ij}$ or equivalently the dacaying anisotropic turbulence towards isotropic turbulence. Such phenomenon brought by the slow term is experimentally verified according to Townsend [6]. Note that the empirical constant C_1 conditions the decay rate of turbulence, the more greater it becomes, the more decay is hasten. For more details about the mathematical foundations and interpretation of the pressure strain correlation modelling, the reader can refer to Durbin [4].

Now, if the RSM equations were expressed in the rotating frame, then it is possible to include the redistribution effect of Coriolis forces in the transport equation for $\rho\overline{w_i' w_j'}$

$$G_{ij} = \rho\Omega_k(\overline{\tau}_{jm}\epsilon_{ikm} + \overline{\tau}_{im}\epsilon_{jkm}).$$

Since each component of the Reynolds stress is calculated by the means Equation 3.33, the turbulent kinetic energy k' can directly be obtained whereas the specific dissipation rate ω' requires one additional equation to reach closure of the problem. In the same manner as for the SST model, a blending approach is used for the transport equation of the specific dissipation rate

$$\partial_t\rho\omega' + \partial_i(\rho\overline{u}_i\omega') = \partial_i\left[\left(\mu + \frac{\mu_t}{\sigma_{\omega 4'}}\right)\partial_i\omega'\right] + \alpha_{\omega 4'}\frac{\omega'}{k'}P_{k'} - \beta_{\omega 4'}\rho\omega'^2 + (1 - F_{bsl})2\rho\frac{1}{\sigma_{\omega 3'}\omega'}\partial_i k'\partial_i\omega'. \tag{3.34}$$

Until this step, it is clear that considerable efforts were put into modelling of the Reynolds stress tensor in order to improve the flow prediction but the RSM has in the same time inherited the same drawback as the two equation model by retaining a dissipation rate expressed in the form shown in Equation 3.34. In fact, this form still provides a specific length scale for the turbulence.

Hereby, the RSM has provided in total 7 equations to complete the closure problem. Inevitably,

this model requires supplementary computational effort put into the resolution of the Reynolds stress transport equations although it is proven to be conceptually superior to the two equations model. Note that the recurrent presence of empirical constants proves that the RSM works in the same order of idea as the two equation model. In other words, the solution provided by these models will highly depend on the manner the constants are defined, which makes the RSM flexible and simultaneously adaptable for the same reason.

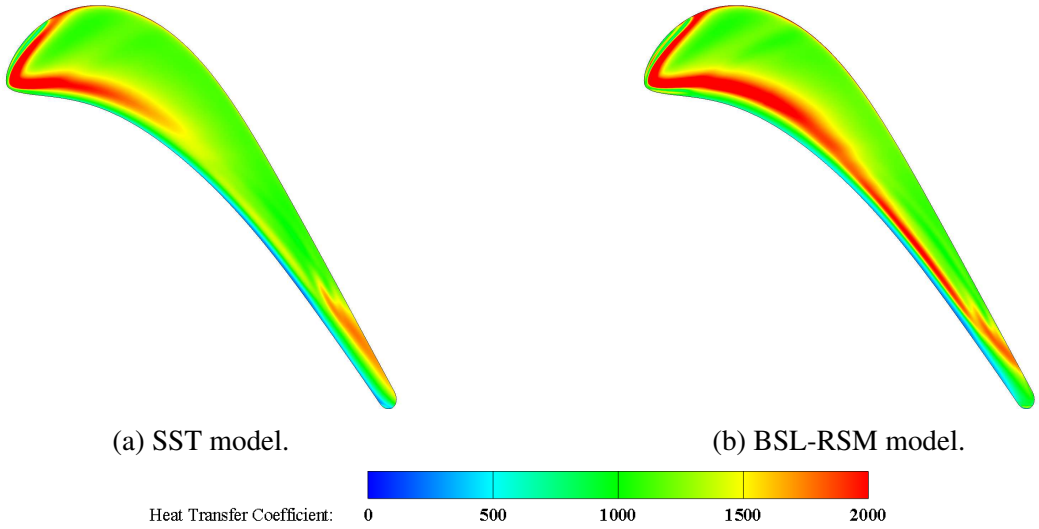

(a) SST model. (b) BSL-RSM model.

Figure 35: Heat transfer coefficient h_c over the blade tip for different turbulence models.

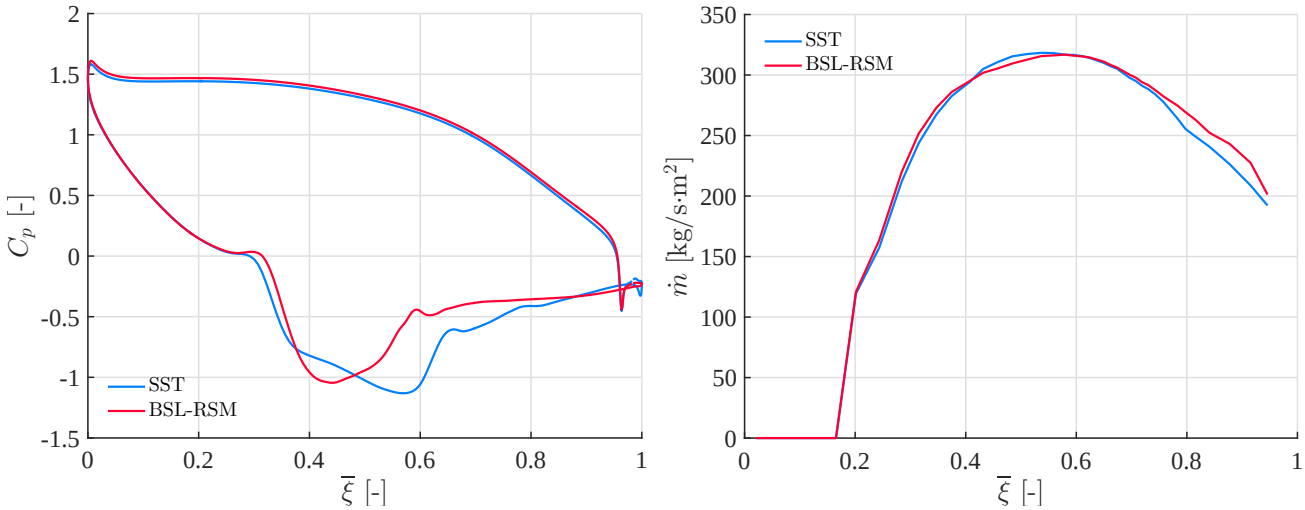

(a) Pressure coefficient distribution at 95% span. (b) Tip leakage mass flow rate per area.

Figure 36: Streamwise distribution of the aerodynamic properties for different turbulence models.

The most striking feature highlighted in the heat transfer coefficient contours depicted in Figure 35 comes from the heat transfer rate in the aft chord re-attachment region next to the pressure side edge. Unlike the result provided by the SST model, the BSL-RSM model predicts much larger heat transfer in this region. Nevertheless, they show agreement at the leading edge, which means that the computed re-attachment length at least in this region is identical for both models. Moreover, the retrieved aerodynamic properties from Figure 36 also present considerable differences. Notably, significant blade loading is maintained in the range from 40% to 80% of the chord in the streamwise direction for the SST model, whereas a maximum is briefly reached at 40% of the chord for the BSL-RSM model. Additionally, the leakage mass flow rate of both models notably differ from 70% chord until

the trailing edge. The SST model predicts less leakage mass flow rate, which is quite curious since the same model indicates large blade loading that is obviously supposed to drive large mass flow rate in the same region. This feature will especially affect the tip leakage vortex formation. In fact, the low pressure region designated as aerodynamic loss in the performance analysis and depicted in Figure 37, marks approximatively the diameter of the tip leakage vortex. Because of the reduced leakage mass flow rate of the SST model in the aft chord region, the width of the tip leakage vortex predicted by the same model is apparently smaller.

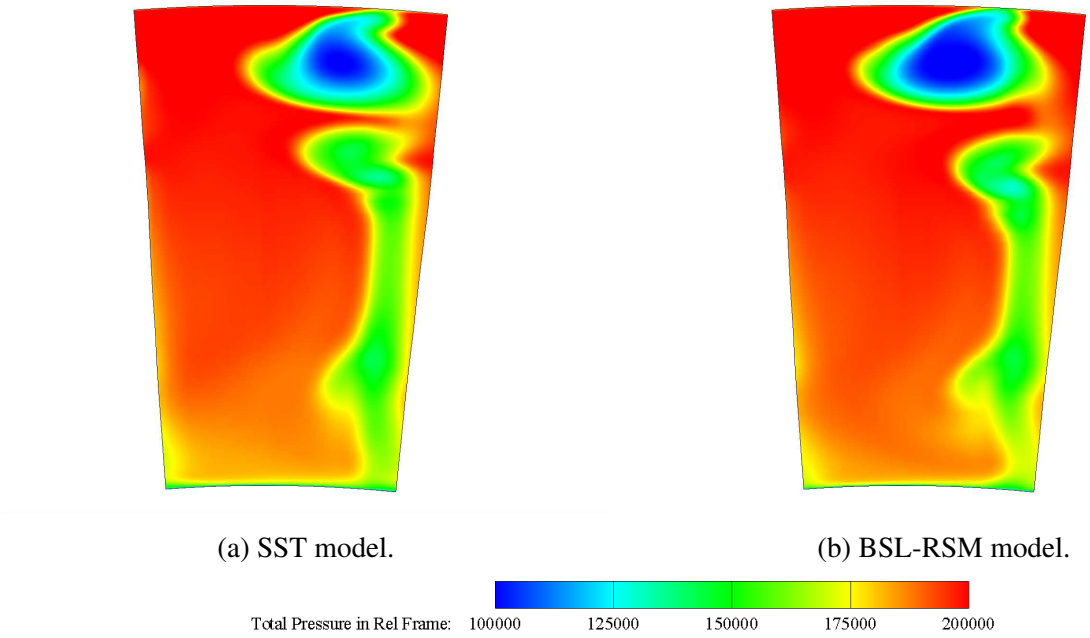

(a) SST model. (b) BSL-RSM model.

Figure 37: Total relative pressure contour at station C (blade row outlet) for different turbulence models.

It should be emphasized that the heat transfer coefficient distribution over the blade tip, predicted by the BSL-RSM model in Figure 35 concurs qualitatively well with the experimental results and model proposed by Lee et al. [11] (see Figure 10). In conclusion, the mathematical foundations and the qualitative analysis highlight the fact that Reynolds stress model is able to offer more advantages than its two equations model counterpart for this turbomachinery flow. Thereby, the BSL-RSM is reasonably adopted as the default turbulence model in the subsequent section.

3.6 Flow and heat transfer over flat tip blade

The first subject treated in this section is the convergence of the numerical solution. The latter is achieved by the intermediary of computational iterations and when the residuals related to several quantities (e.g. mass, momentum, Reynolds stress) become quasi-constant over a large range of iterations. For this case, 500 iterations were needed to acquire the steady solution. Meanwhile, the root-mean-square measure of the residuals that conditions the accuracy of the solution, is monitored as well. The mass flow rate and heat transfer residual are of the order 10^{-6} and the momentum and Reynolds stress residuals are of the order 10^{-5}.

The second subject to investigate is the presence of shock waves. Their identification is performed by the means of pressure/density contours depicted in Figure 38. The sudden variation underlined on the suction side of the blade reflects the feature of a shock wave, that is, the considerable increase of density/pressure across a narrow separation line that corresponds to the thin shock layer. Moreover, the near tip region is exposed to supersonic flow, thus the shock wave should extends to the tip according

to the theoretical consideration made previously with the velocity triangle. However, the results show that the shock wave only encompasses a large portion of the blade span beneath the near tip region. This important feature proves that secondary flows developed upstream are dominant and and have consecutively prevented the formation of shock waves in the near tip region.

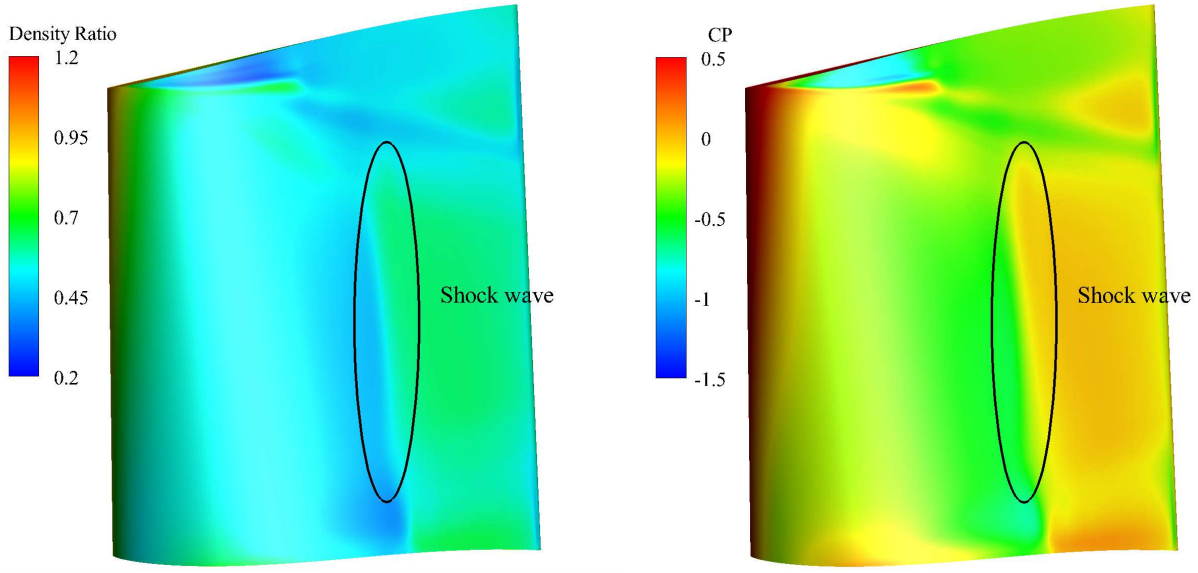

(a) Normalized density. (b) Pressure coefficient.

Figure 38: Side view of the contours on the suction side of the blade.

In the same order of idea, Figure 39 proposes an alternative way to identify the shock wave located in the underlined circle. This area mainly exhibits the thickness of the shock layer and the thickening of the boundary layer caused by the shock. On the other hand, transition from subsonic to supersonic regime before the shock is observed, it implies that the blade to blade passage is chocked during the transition. The chocking area is highlighted by the sonic line and starts at the streamwise mid-chord to end up at the trailing edge of the adjacent blade.

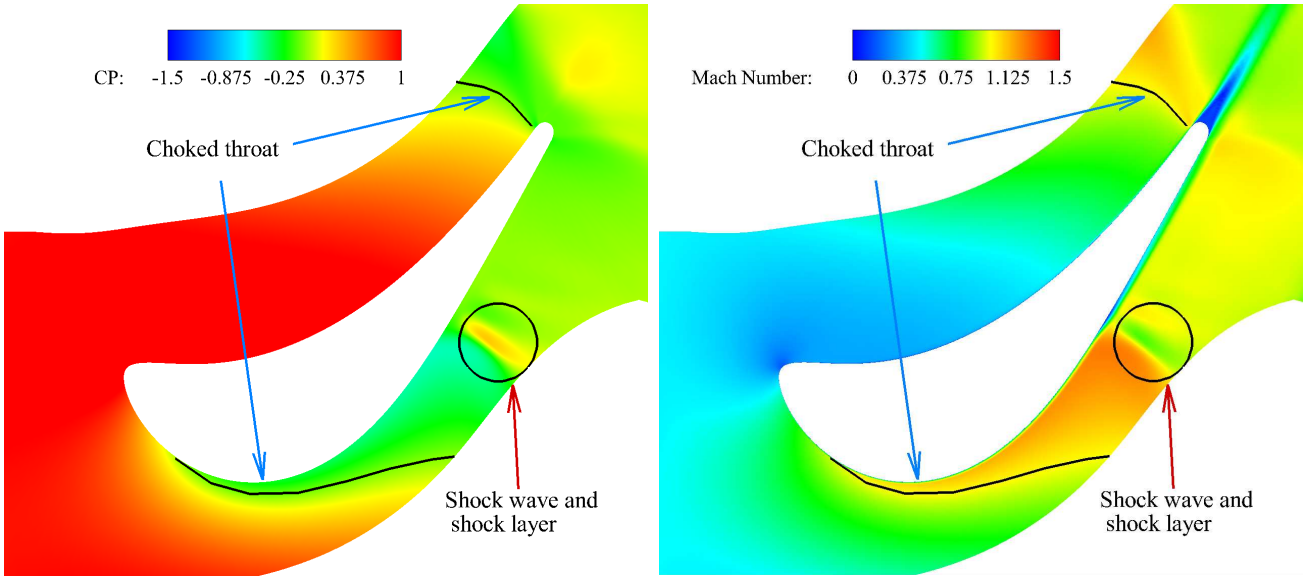

(a) Pressure coefficientwe. (b) Mach number.

Figure 39: Blade-to-blade view of the contours at mid-span of the blade.

Now, it is possible to determine the location of the shock wave by the means of the pressure distribution at different span location as shown in Figure 40a. Evidently, the sudden increase of pressure marks the location of the shock wave at about 70% of the chord in the streamwise direction. Another interesting feature to mention is the variation magnitude that differs for distinct span location. The relatively small jump measured at 70% span proves that the shock is weakened in the near tip region. However, the adiabatic temperature distribution in Figure 40b reports a drastic temperature elevation at the shock position for the same span location. A weakened shock can physically not produce such amount of energy dissipation by itself if one refers to the result at mid-span. Therefore, it can be concluded that secondary flows (already present at 70% span) and possible shock-secondary flow interaction are greatly responsible for energy dissipation in the near tip region.

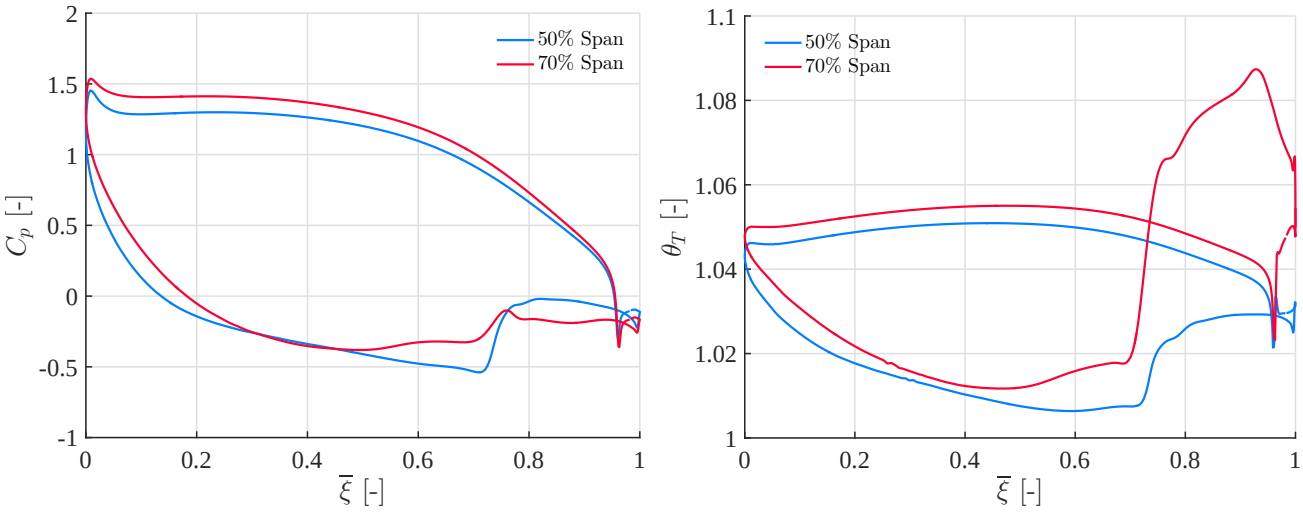

(a) Pressure coefficient distribution.

(b) Normalized Temperature.

Figure 40: Streamwise distribution of the aerothermal properties at 50% and 70% span.

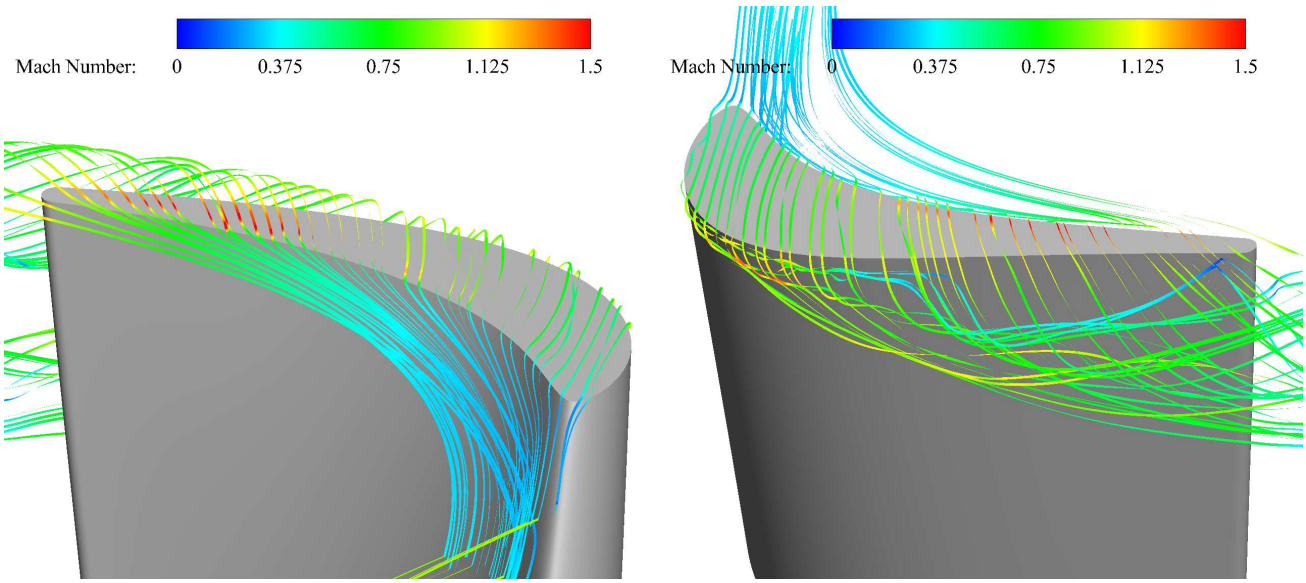

(a) Pressure side view.

(b) Suction side view.

Figure 41: Streamlines and Mach number distribution passing through the tip gap.

The third subject to treat is the aerodynamics of the tip leakage flow. The streamlines present in Figure 41 depict the trajectory of the flow passing through the gap and roll up on the suction side right after crossing the gap exit in order to generate the tip leakage vortex. According to the Mach

number distribution, the incoming flow was initially at low speed before entering the gap. Once inside the gap, the flow undergoes an brief acceleration and can even reach supersonic state in the aft chord region. By the intermediary of the shroud boundary layer, a channel flow within the gap is established soon after. Note that it is possible to distinguish two vortices on the suction side view, there are the tip leakage vortex and the passage vortex located just beneath.

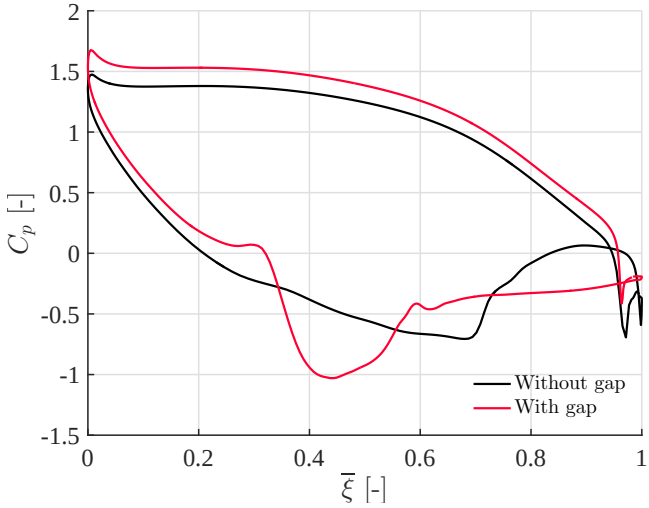

(a) Pressure coefficient with/without gap.

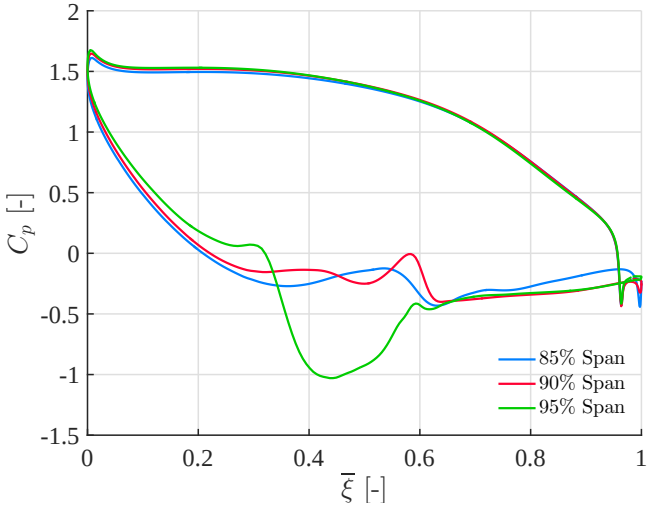

(b) Pressure coefficient in near tip region.

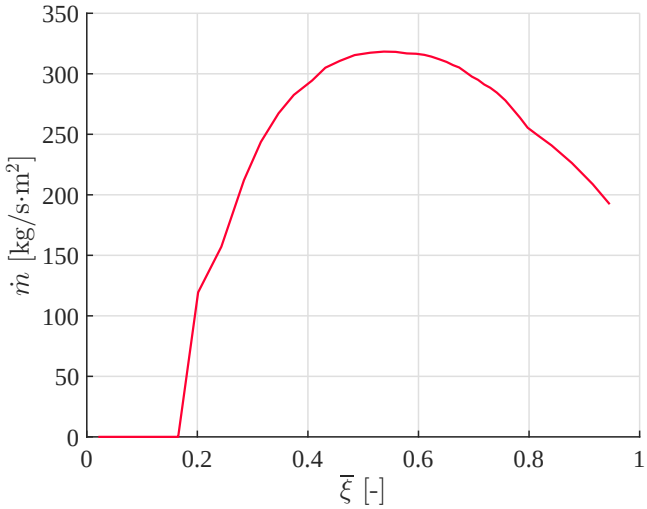

(c) Tip leakage mass flow rate per unit area.

Figure 42: Streamwise distribution of the pressure coefficient and the mass flow rate.

Next comes the analysis of the altercation brought by the presence of the gap on the pressure distribution around the blade. By recalling the consideration about the shock wave made above, the pressure distribution without gap in Figure 42a has proven that the shock wave can indeed extend over the entire span in the absence of secondary flow. Additionally, the results in Figure 42b omit the presence of the shock wave and are fully conditioned by the secondary flow. The rapid pressure drop at 95% span constitutes the very reason that causes a reverse flow right after the gap exit and triggers roll-up of the flow. Whereas, secondary flows only induce small perturbation for other span locations. According to the Figure 42c determined at the suction side of the blade tip, leakage is quasi-absent at the leading edge (0% - 15% streamwise chord) and increases rapidly to reach a peak at streamwise mid-chord. Since mass flow and heat transfer rates are intimately related, this distribution can indicate the region of the tip that undergoes high heat exchange. In this case, high heat transfer is more likely to happen in a region that extends from 30% to 95% streamwise chord. The tip leakage vortex formation mechanism is visualized and detailed by the intermediary of Figure 43.

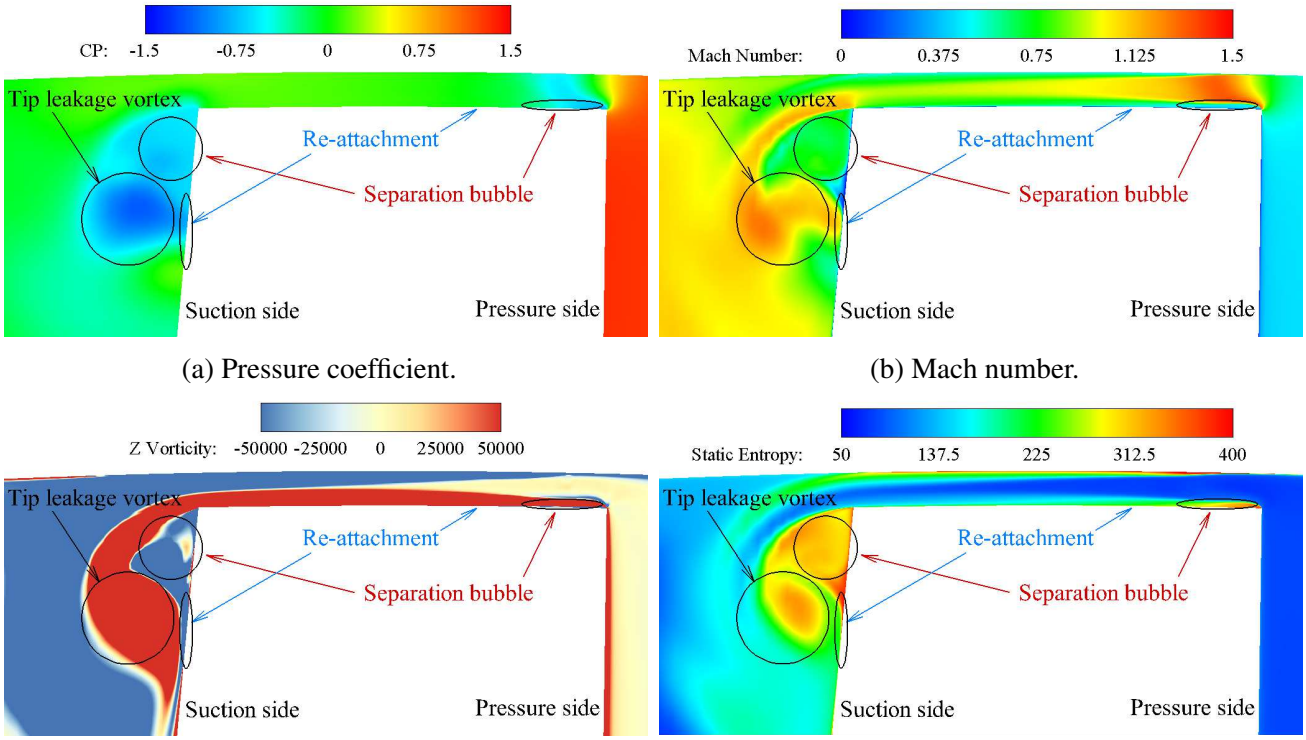

(a) Pressure coefficient.

(b) Mach number.

(c) Axial vorticity.

(d) Static entropy.

Figure 43: Aerodynamic quantity contours at mid-chord .

As mentioned in the previous section, the entry separation bubble is observed and reduces the net entry area of the gap. Consequently, acceleration of the leakage flow is enhanced and supersonic state is briefly attained in the region affected by the separation bubble. Once re-attachment is obtained a bit further downstream, flow velocity is slightly decreased because of the establishment of the channel flow and is consecutively held more or less constant until the gap exit. What follows at the gap exit is in some sense similar to the backward facing step flow except that the "step" corresponds to the long suction side wall. The sudden withdrawal of the tip wall produces two types of secondary flow, namely a mixing layer and a separation bubble next to the suction side wall. The separation bubble is associated to a local low pressure area and prompts reverse flow and impingement on the blade surface. Consecutively, the adjacent mixing layer is entrained by the local adverse pressure gradient, undergoes an acceleration and eventually follows a roll-up pattern. These flow features put altogether constitute the basic mechanism for tip leakage vortex formation.

In a way similar to the representation of the vortices proposed by Wei et al. [19] in Figure 14, the distinct vortices that contribute to aerodynamic losses are identified by the means of multiple cut planes placed at different axial chord location as shown in Figure 44. One of the most striking feature of the tip leakage vortex is its velocity magnitude. The tip leakage vortex advects downstream at relatively low velocity, it can even be compared to stagnant air that may compromise the proper operation of the rotor row. The main tip leakage vortex marked roughly as region C and developed at early stage, is constantly fuelled by the tip leakage flow along the chord until the trailing edge is reached. Simultaneously, mixing and diffusion occur as the vortex is convected by the main flow, resulting in a large region of influence downstream. Meanwhile, the counter-rotating passage vortex marked by region B and located right below, is also observed at early stage, it mixes and diffuses in the same manner as the tip leakage flow. The role assumed by these two main antagonist vortices is to dissipate the mechanical energy contained in the tip leakage flow into heat before mixing and diffusion could occur, the associated loss is depicted by the entropy increase in the neat tip region on the suction side.

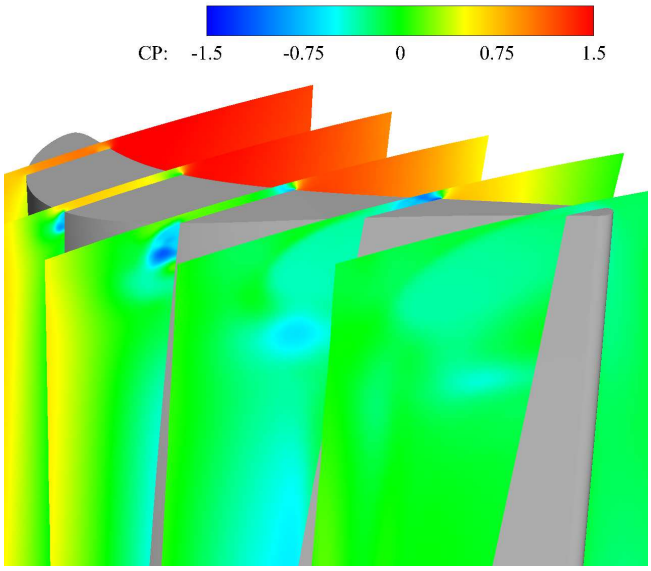

(a) Pressure coefficient.

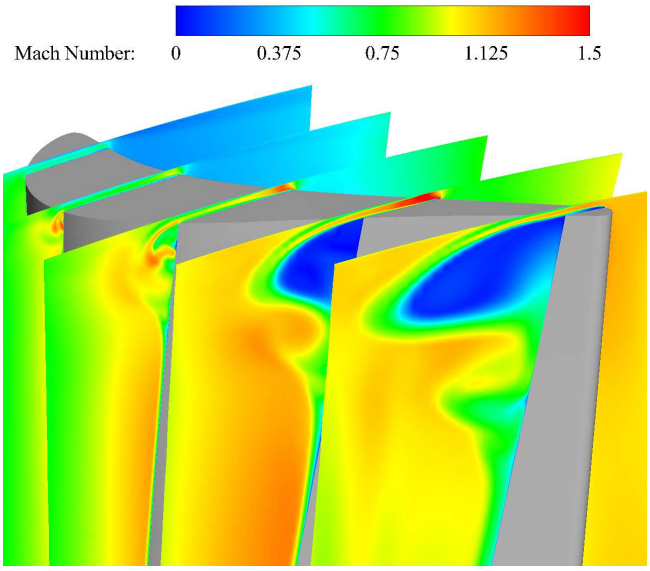

(b) Mach number.

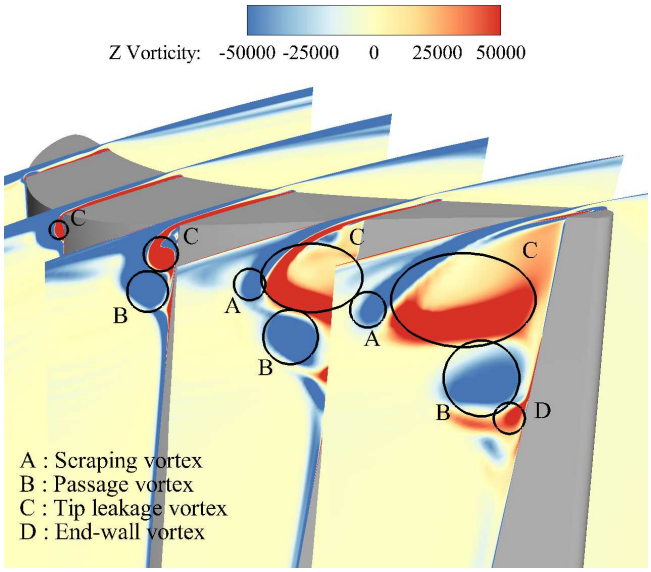

(c) Axial vorticity.

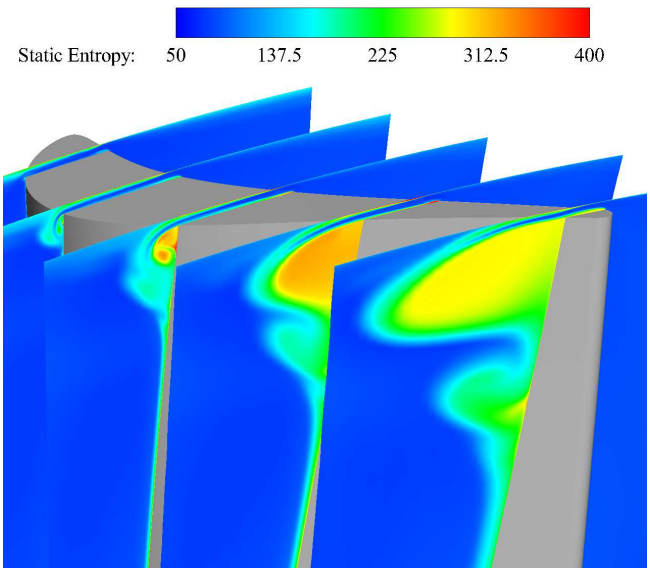

(d) Static entropy.

Figure 44: Contour of the tip leakage flow at different axial chord locations z/c_z = 0.15, 0.35, 0.55, 0.75, 0.95.

The fourth subject to analyse is the heat transfer phenomenon over the rotating blade. There are two main approaches employed by the investigators to quantify the solid/fluid heat transfer, Krishnababu [28] and Han [21] tend to use the heat transfer coefficient, whereas Zhang et al. [41] uses the Nusselt number instead. For completeness, both approaches are exhibited in this part although they are conceptually identical. In Figure 45a, a high heat transfer band that covers approximatively 10% to 50% of the axial chord is visible in the near tip region. It results from a re-attachment of the flow (see Figure 43) since the tip leakage vortex is clung to the wall during its early development stage. Nevertheless, the axial distance dependent Nusselt number depicted in Figure 45b tends to magnify heat transfer due to tip leakage vortex diffusion near the trailing edge unlike its counterpart in Figure 45a. Note that the passage vortex induces low heat transfer and is progressively pushed downward by the tip leakage vortex.

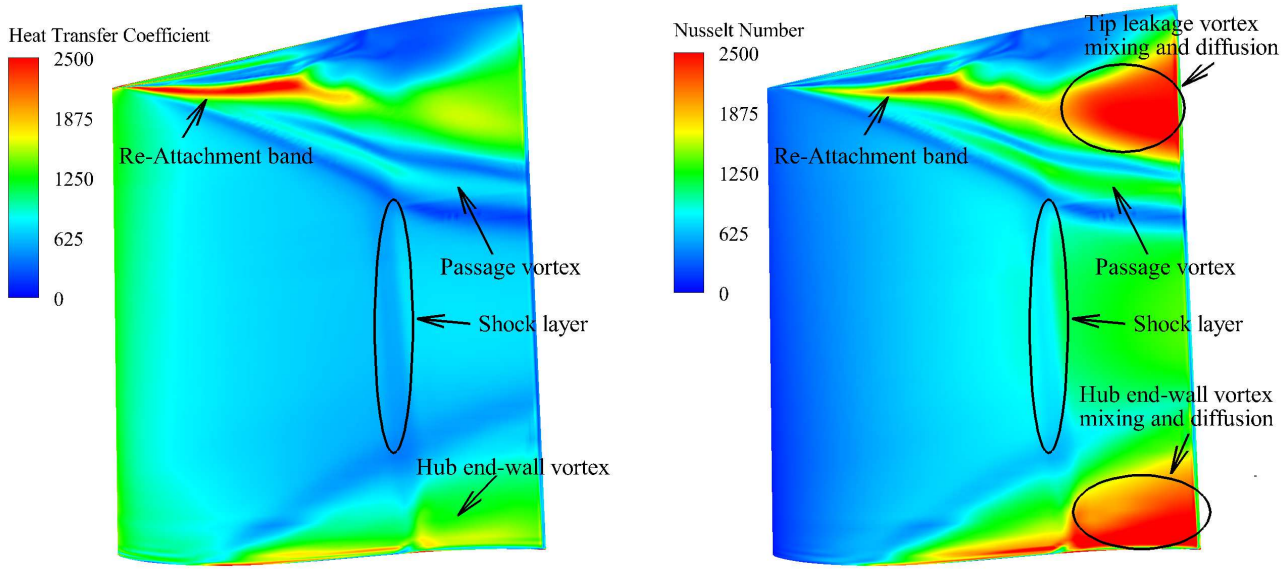

(a) Heat transfer coefficient. (b) Axial Nusselt number.

Figure 45: Side view of the thermal properties contour over suction side of the blade.

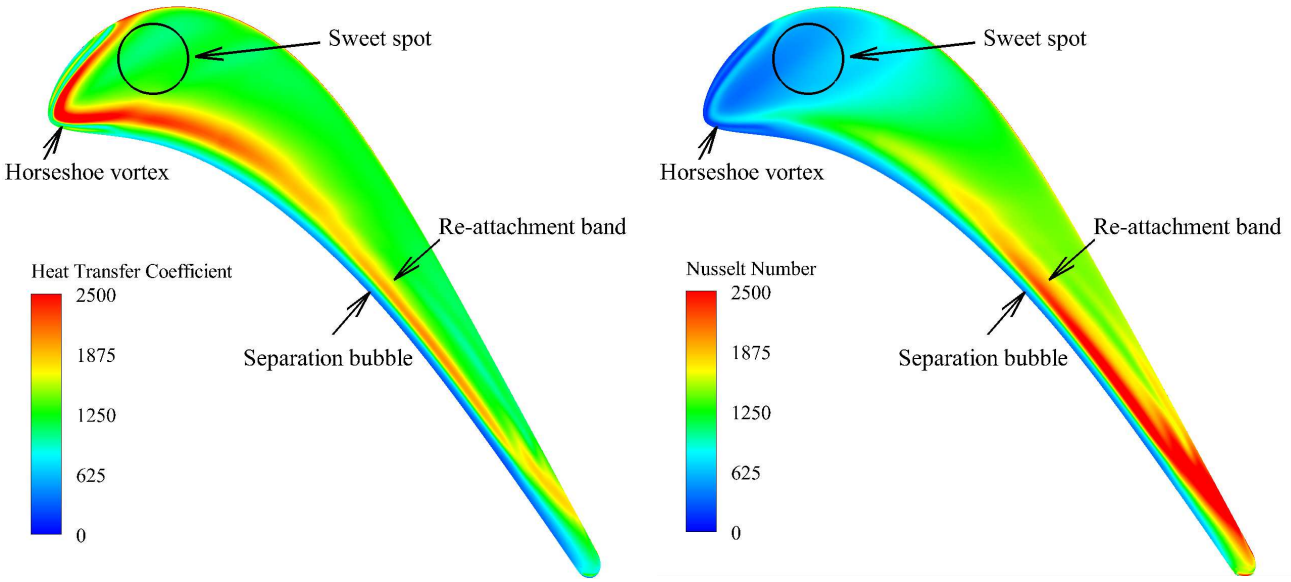

(a) Heat transfer coefficient. (b) Axial Nusselt number.

Figure 46: Thermal properties contour over the tip.

The pattern exhibited by either Figure 46a or 46b concurs qualitatively with the results proposed by Lee et al. [11] and Bunker [15]. The high heat transfer band in Figure 46a is again associated to the re-attachment line in this context and agrees with the tip leakage mass flow distribution exhibited in Figure 42c. Precisely at the entrance of the leading edge, a horseshoe vortex that precedes the re-attachment line, is developed and spreads as two counter-rotating vortices in different direction. The suction side arm vortex moves along the suction side edge and leaves the gap at about 10% axial chord. Meanwhile, the pressure side arm vortex tends to reach the trailing edge by staying close to the pressure side edge. On the other hand, the low heat transfer region located right on the pressure side edge, is characterized by the recirculation region within the entry separation bubble. The absence of mass flow at the leading edge in Figure 42c or the sweet spot present in Figure 19 is visible at the leading edge of Figure 46b and indicates in the same manner a region of low heat transfer. The non-dimensional measure tends to lessen heat exchange at the leading edge whereas

heat transfer is magnified at the rear part of the blade. This feature is obviously linked to the axial distance dependence of the Nusselt number. Nonetheless, both measures agree on the fact that the near trailing edge region of the blade tip is exposed to undesirable high heat load, thus rendering it vulnerable. Overall, the Nusselt number apparently consists of a conservative measure of the heat transfer, but its main advantage lies on the multiple features of flow (e.g. Reynolds number, Prandtl number, etc...) that it is able to take into account. Thereby, because of its "completeness", the Nusselt number is retained for the rest of the study.

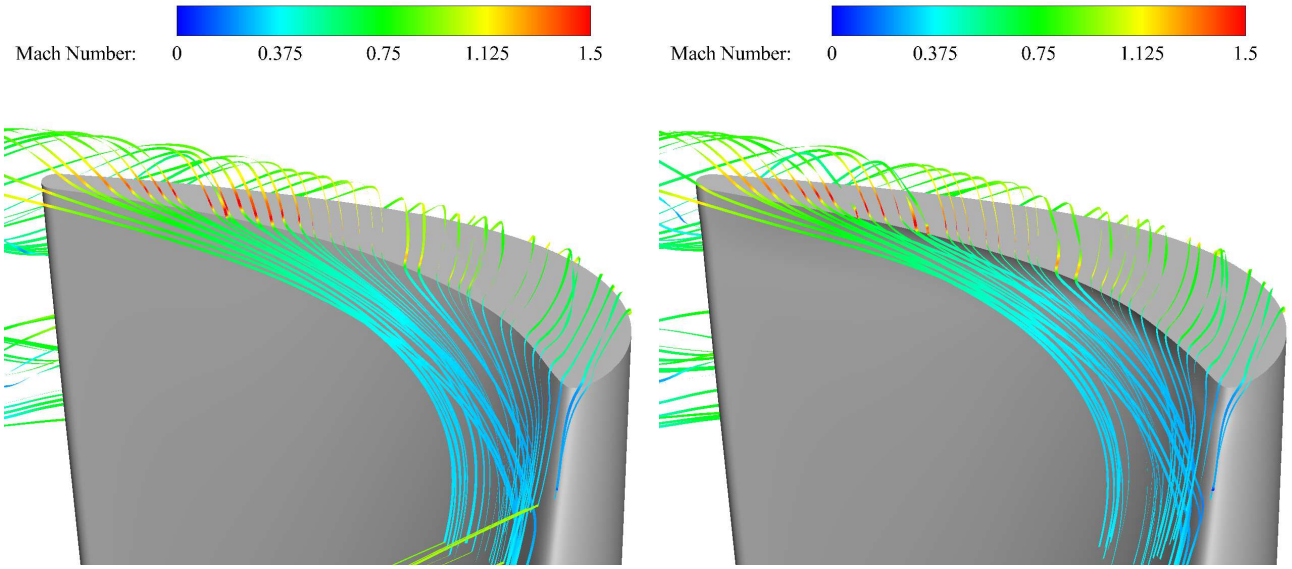

(a) Original profile. (b) Modified profile.

Figure 47: Streamlines and Mach number distribution passing through the tip gap.

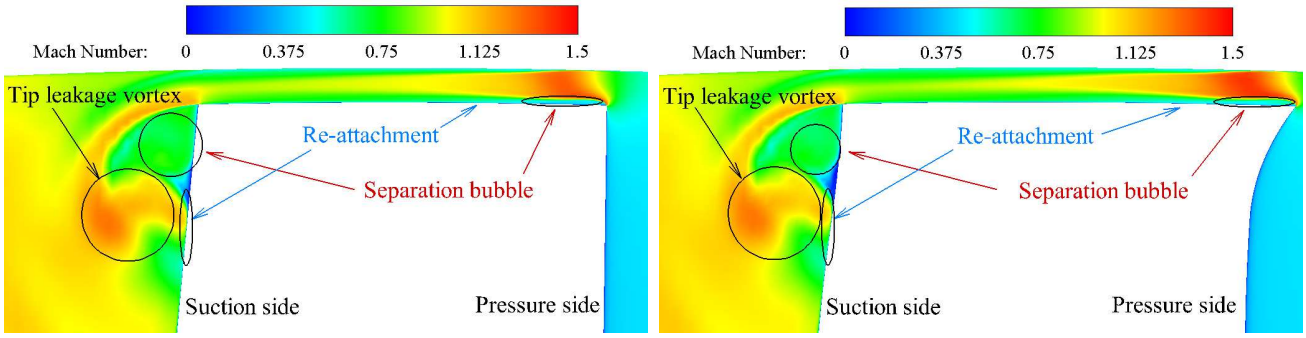

(a) Original profile. (b) Modified profile.

Figure 48: Mach number contour at mid-chord .

Until this step, it has become clear that tip leakage flow is able to cause significant aerodynamic loss and local heat exchange. Hereby intervenes the purpose of this study, modification and possible improvement are proposed in order to regulate the tip leakage flow. The most straightforward and simple alternative is to modify geometrically the blade tip profile as shown in Figure 25 except that cavity is omitted in the first instance. In order to determine the changes due to this input, the analysis procedure defined above is re-employed. According to the streamlines depicted in Figure 47, the concave curvature brought to the pressure side rim tends to slightly deviate the flow downstream. This feature can more or less delay the flow from entering the gap and even prevent tip leakage over a small portion of the trailing edge. However, the Mach number contour of the modified blade in Figure 48 does not provide any remarkable change over the tip leakage flow despite the slightly

stronger acceleration at the gap entrance. As stated earlier, the geometrical modification is able to delay the flow from penetrating into the gap, this is expressed as a small pressure shift depicted in Figure 49a and 49b. Additionally, Figure 49c shows clearly that incident flow deviation and tip leakage flow delay results in a slight decrease of the mass flow rate over a broad region that extends from 40% to 80% streamwise chord at the gap exit. This is evidently beneficial since a part of this mass flow rate is used to fuel the tip leakage vortex. Basing on this feature, slight improvement on the aerodynamic loss can be foreseen.

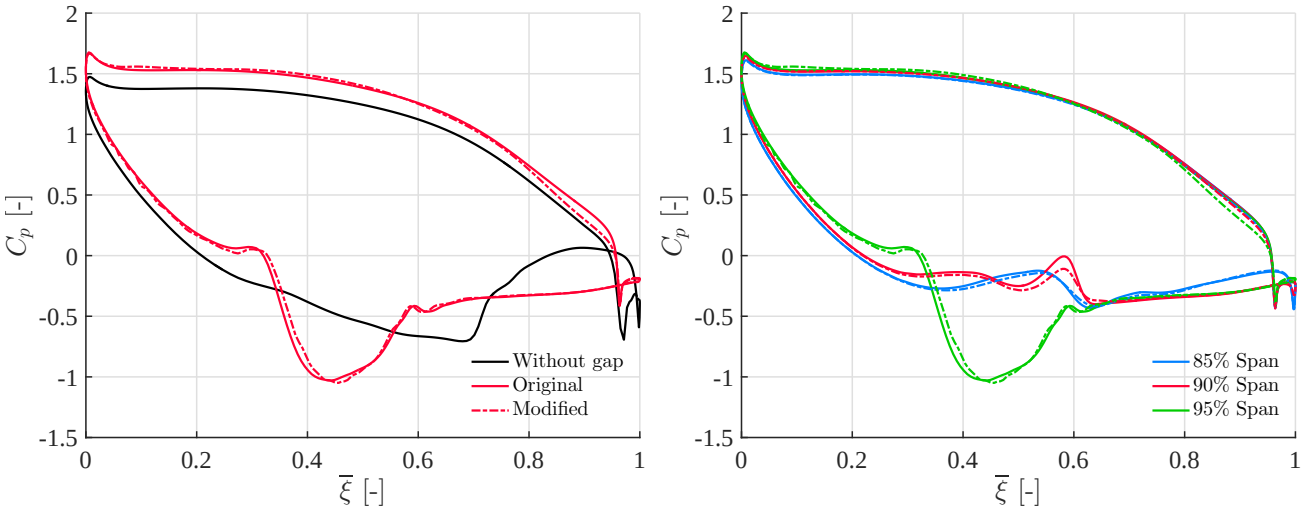

(a) Pressure coefficient with/without gap.

(b) Pressure coefficient in near tip region.

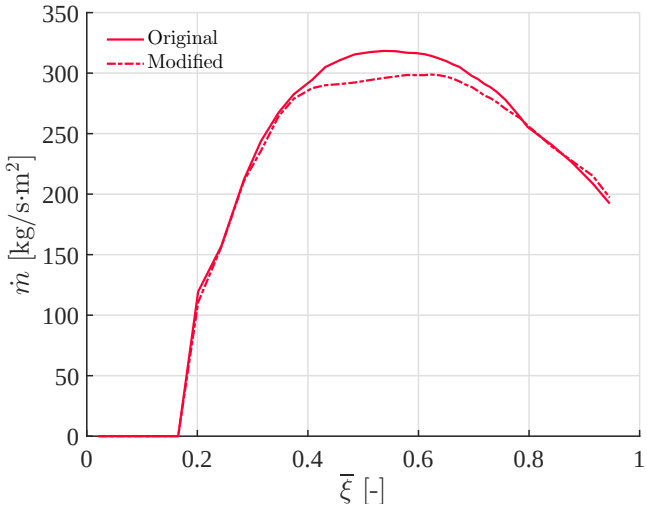

(c) Tip leakage mass flow rate per unit area.

Figure 49: Streamwise distribution of the pressure coefficient and tip leakage mass flow rate for flat blade profiles

In the same order of idea for the heat transfer phenomenon on the blade tip, because of the flow deviation, the high heat transfer band is slightly lowered in the mid-chord region. The rest remains exactly the same as for the original profile. It must be emphasized that the slightly stronger acceleration at the gap entrance may augment the heat transfer at the re-attachment regions located right after.

Nevertheless, the last topic to investigate is the estimation of the energy dissipated by the tip leakage flow. For such aim, one needs to refer to no gap configuration to quantify the loss. Hence,

$$Y_t = \dot{m}_t T_C s_C - \dot{m}_{t,ng} T_{C,ng} s_{C,ng}. \tag{3.35}$$

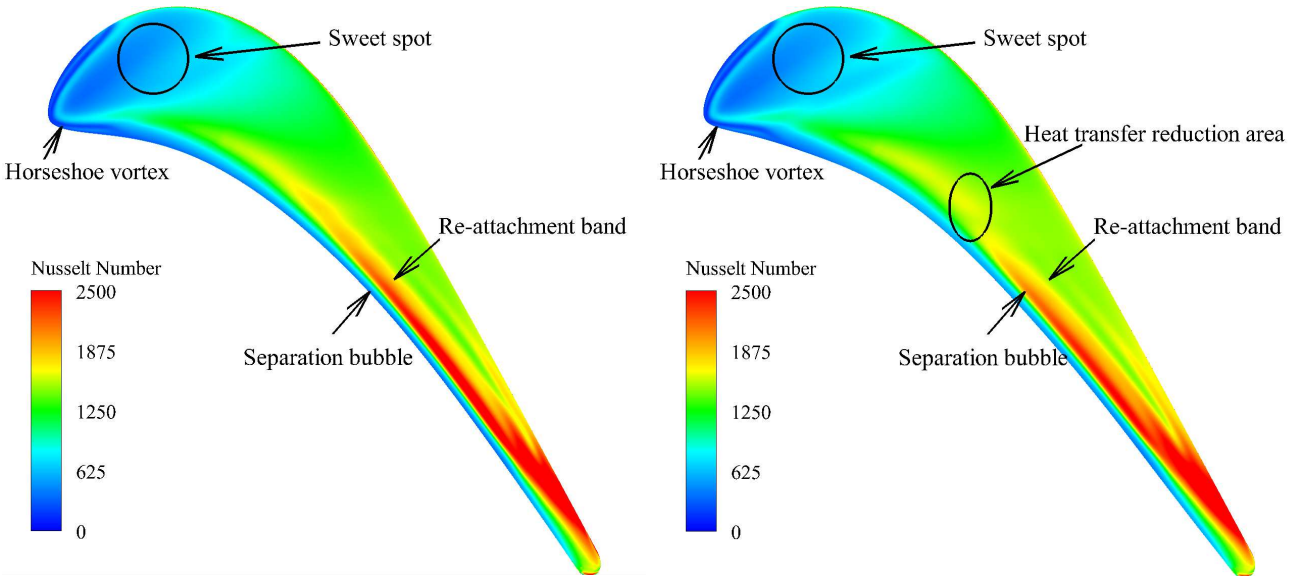

(a) Original profile. (b) Modified profile.

Figure 50: Axial Nusselt number contour over the tip.

The total loss can be split into an internal and external contributions. The internal loss produced within the gap is given by

$$Y_{int} = \dot{m}_l T_{ex} s_{ex}. \tag{3.36}$$

The external loss due to mixing and produced outside of the gap is simply the difference

$$Y_{ext} = Y_t - Y_{int}. \tag{3.37}$$

The non-dimensional Υ_{int} and Υ_{ext} are acquired by division of their respective Y_{int} and Y_{ext} by the total leakage loss of the original flat blade profile taken as a reference in this context, which is

$$Y_{t,ref} = 2.024 \times 10^3 \text{ W}. \tag{3.38}$$

It comes for the application of the performance analysis tools

Blade	Original	Modified
P_w [MW]	1.9	1.901
T_w [kN.m]	1.649	1.65
η_t [%]	93.2	93.2
η_{ts} [%]	85.3	85.3
$T_{t,C}/T_{t,B}$ [-]	0.771	0.772
$p_{t,C}/p_{t,B}$ [-]	0.374	0.374
Υ_{int} [%]	16.1	13.5
Υ_{ext} [%]	83.9	81.3
$h_{c,av}$ [W/m^2.K](10^3)	1.336	1.346

Table 5: Aerothermal performance of the flat blade profiles

Additionally, the degree of reaction, the loading factor and flow factor for this flow are

$$R_c = 24\%, \qquad \psi = 1.54, \qquad \phi = 0.54. \tag{3.39}$$

The performance analysis yields several results :

- The high pressure turbine stage is able to deliver a significant amount of work and operate at high efficiency regardless of the blade profile. This means that this modification of the blade tip does not affect the global performance of the turbine stage. However, the tip area averaged heat transfer has curiously increased. This implies that heat transfer occurring at re-attachment regions is enhanced.
- It is interesting to emphasize the fact that external mixing loss composes a large fraction of the tip leakage loss. This result agrees with the physical flow detailed above where production of entropy mainly occurs in the region exterior to the gap. Nevertheless, the modification was only able to deliver a small improvement on the tip leakage loss though a more significant change is sought. In any case, a more effective solution must be proposed.

3.7 Flow and heat transfer over double squealer tip blade

Basing on the previous point, it has become clear that a geometrical modification of the blade tip provides a local reduction of the loss. In this section, this same idea is re-exploited but this time, it has to deliver a more significant improvement on the aerodynamic performance. For such aim, one can refer to existent tip profiles as suggested by Kwak et al. [24], this latter essentially provides an overview of the geometrical effect on the reduction of tip leakage mass flow rate.

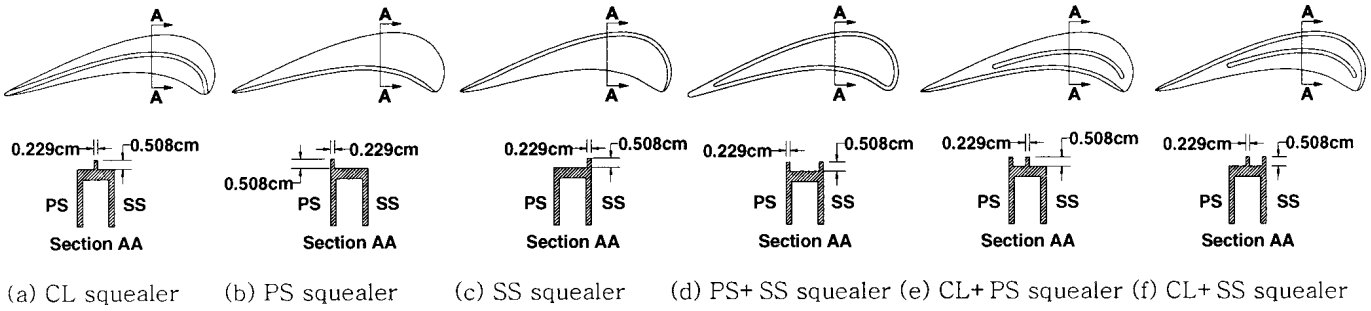

Figure 51: Geometry of squealer tip profiles. Courtesy of Kwak et al. [24].

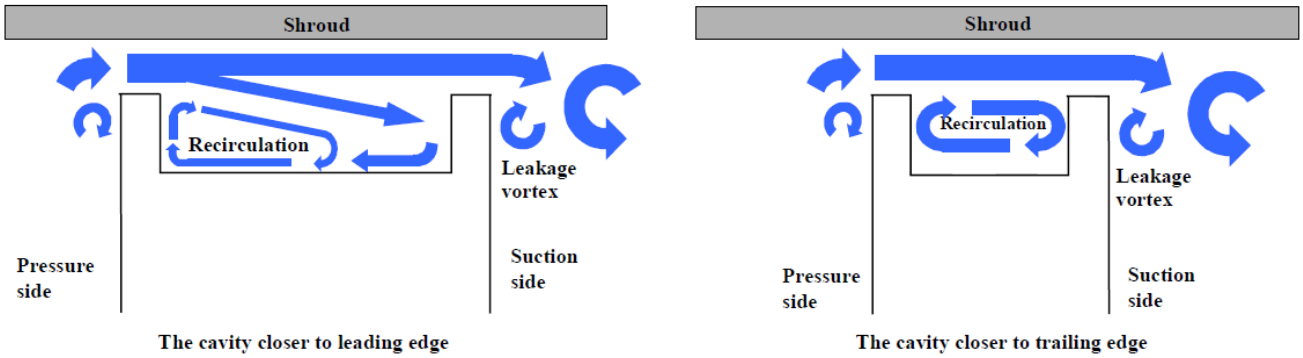

Figure 52: Conceptual view of the flow near the double squealer tip.

The outcome of his work suggests the adoption of the double squealer tip which is able to deliver the most adequate aerodynamic enhancement. As depicted in Figure 52, the adoption of a centered cavity over the blade tip will drastically alter the tip leakage flow mechanism. To visualize and comprehend the latter, the backward step flow analogy can again be re-exploited. The flow entering the gap by the pressure side undergoes a separation as soon as the step is met. Note that a separation bubble is formed on the top of both squealers. Consequently, a mixing layer and a zone of recirculation are simultaneously developed right after the step. Depending on the width of the cavity, the

recirculation are can cover the entire cavity, which is the case near the trailing edge. On the opposite, if the cavity is wide enough, re-attachment follows soon after and recirculation will occur again as soon as the suction side squealer is encountered. Until this step, a channel flow is established, so the leakage flow velocity profile is affected by the presence of the shroud boundary layer and the zones of recirculation. It must be emphasized that the suction side recirculation which draws part of the main leakage flow, forces the flow backward, therefore creating a flow confinement effect that considerably lower the leakage mass flow rate at the gap exit, which in turn could reduce the aerodynamic loss due to tip leakage flow. Unfortunately, the lack of space within the gap at aft chord does not allow a second circulation, thus the mass flow rate is expected to remain larger than other regions of the blade tip.

Moreover, it has been proven that the concave curvature brought to the pressure side rim constitutes an improvement, thereby it is retained and combined together with the double squealer configuration. The adopted dimension for each squealer is depicted in Figure 25. Now, by using the mesh generator AutoGrid5^{TM}, the inclusion of a cavity in the near tip region requires an extra a consideration of about three millions cells in the mesh, which makes 11.2 millions cells in total. The cell arrangement (e.g. spanwise distribution, expansion ratio, etc...) follows the same rule as the original blade, i.e. the finest cells are concentrated in the near tip region to enhance the accuracy of the results.

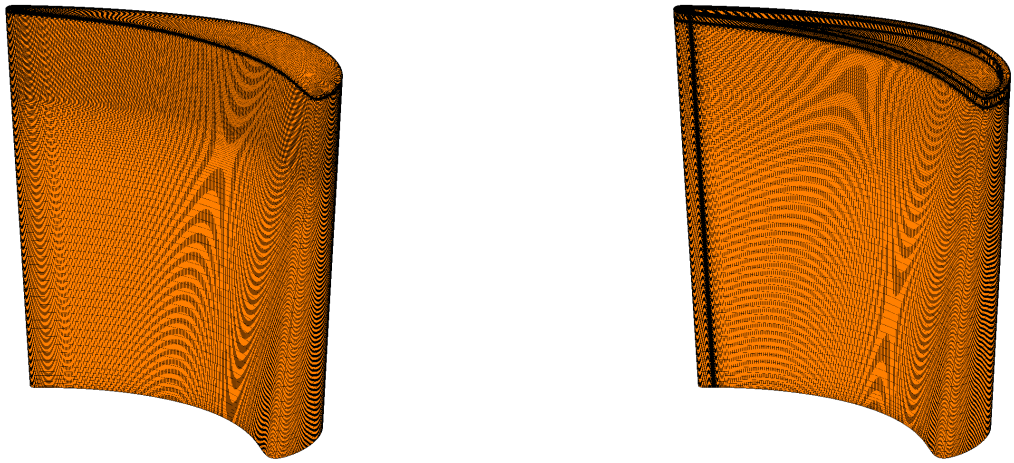

(a) Flat tip of the original blade.

(b) Double squealer tip of the modified blade.

Figure 53: 3D view of the structured mesh generated over the blade surface.

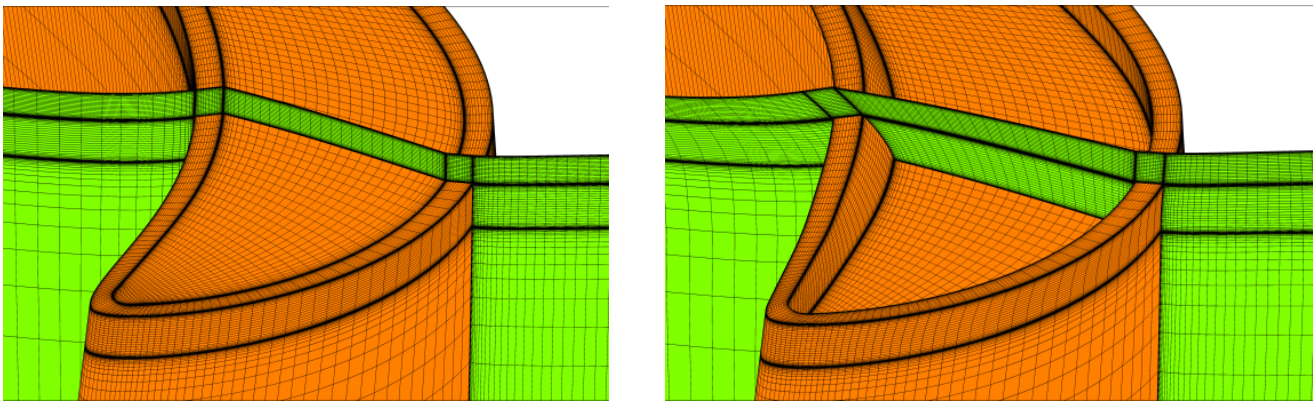

(a) Flat tip of the original blade.

(b) Double squealer tip of the modified blade.

Figure 54: 3D view of the structured mesh generated over the blade surface near the leading edge.

To rectify this inconvenience related to the insufficient cavity width in the aft chord region, it is possible to augment the width of the cavity by cutting by half the squealer width as suggested by Zhou [40], so that a total length of τ is gained. This corresponds to an additional blade tip configuration that is simultaneously considered in the subsequent analysis.

Here again, the same analysis procedure is conducted. The first feature to investigate is the streamline pattern shown in Figure 55. The presence of the cavity drastically reshaped the streamlines, the most striking change is the omission of a brief supersonic flow over the rear blade tip. Unlike the flat tip, there are two horseshoe vortices established at the leading edge, a narrow one on the top of the squealer and a broader one inside the cavity. They both separate into a pair of counter-rotating vortices that spread along the suction and pressure sides. In any case, re-attachment regions are expected. However, the limited space spared by the squealer width does not allow the narrow horseshoe vortex to spread farther inward, its pressure side arm will mix and combine with the pressure arm of the broader cavity horseshoe vortex, whereas its suction side arm will simply replicate the same mechanism but with the suction side arm of the broader cavity horseshoe vortex. The broader horseshoe confined within the gap and formed by the intermediary of the squealer, is much more persistent. Its pressure side arm extends along the pressure side squealer and eventually impinges on the suction side squealer before leaving the gap, whereas its suction side arm leaves the gap at approximatively mid-chord. On the other hand in the mid-chord region, the leakage flow entering from the pressure side are partially confined by the pressure side vortex inside the cavity. In sum, both horseshoes mutually interact and the stronger cavity horseshoe vortex conditions the tip leakage flow.

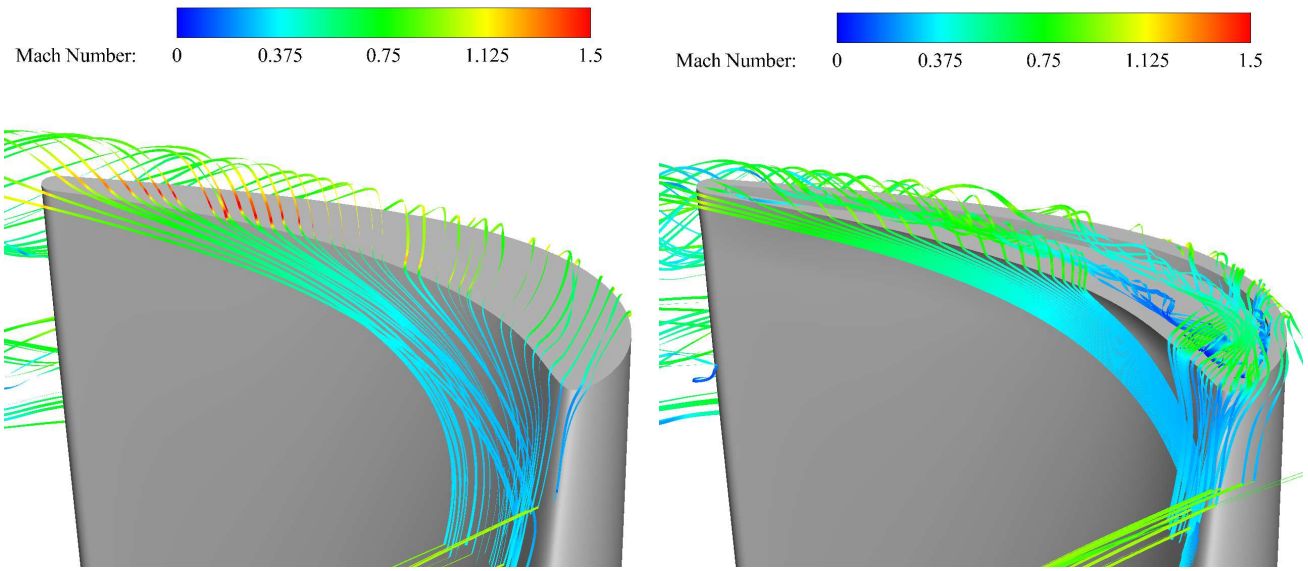

(a) Flat tip profile.

(b) Double squealer tip profile.

Figure 55: Pressure side streamlines and Mach number distribution passing through the tip gap.

Now comes the aerodynamic aspect of the tip leakage flow. The cuts depicted in Figure 56 and 58 clearly exhibits a reduction of the influence of the tip leakage vortex on its surrounding. In fact, the cavity has globally lowered the amount the leakage mass flow rate that fuels the tip leakage vortex and consecutively, weakening of diffusion and mixing is observed near the trailing edge. Consequently, predominance of the tip leakage flow is diminished in the near tip region and the other surrounding vortices are able to develop without too much interference.

The cut at mid-chord shown in Figure 57 and 59 provides a better overview of the flow mechanism within the gap. The consideration of the cavity does not fundamentally alter the tip leakage flow. In fact, the tip leakage flow still rolls up into a vortex that is preceded by a separation right after the gap

exit and is followed by a re-attachment region. However, several separation bubbles and mixing layers have emerged from the adoption of the cavity. Notably, the corner separation bubbles that contain the main cavity vortices of opposite rotating directions. As cited previously, the separation bubbles over the squealers, which reduce the net gap entrance area, contribute together with the corner separation to the early establishment of a channel flow. The expansion of the cavity can actually augment the amount of confined mass flow and consecutively, force a larger reverse flow as shown in Figure 52.

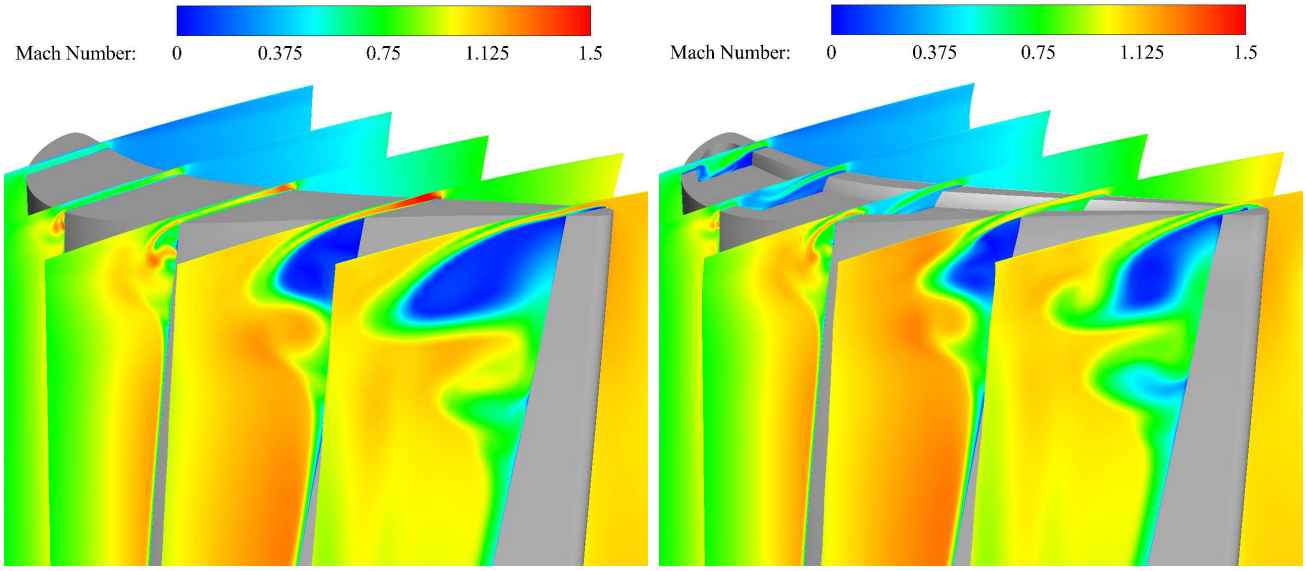

(a) Flat tip. (b) Double squealer tip.

Figure 56: Mach number contour of the tip leakage flow at different axial chord locations $z/c_z = 0.15$, 0.35, 0.55, 0.75, 0.95.

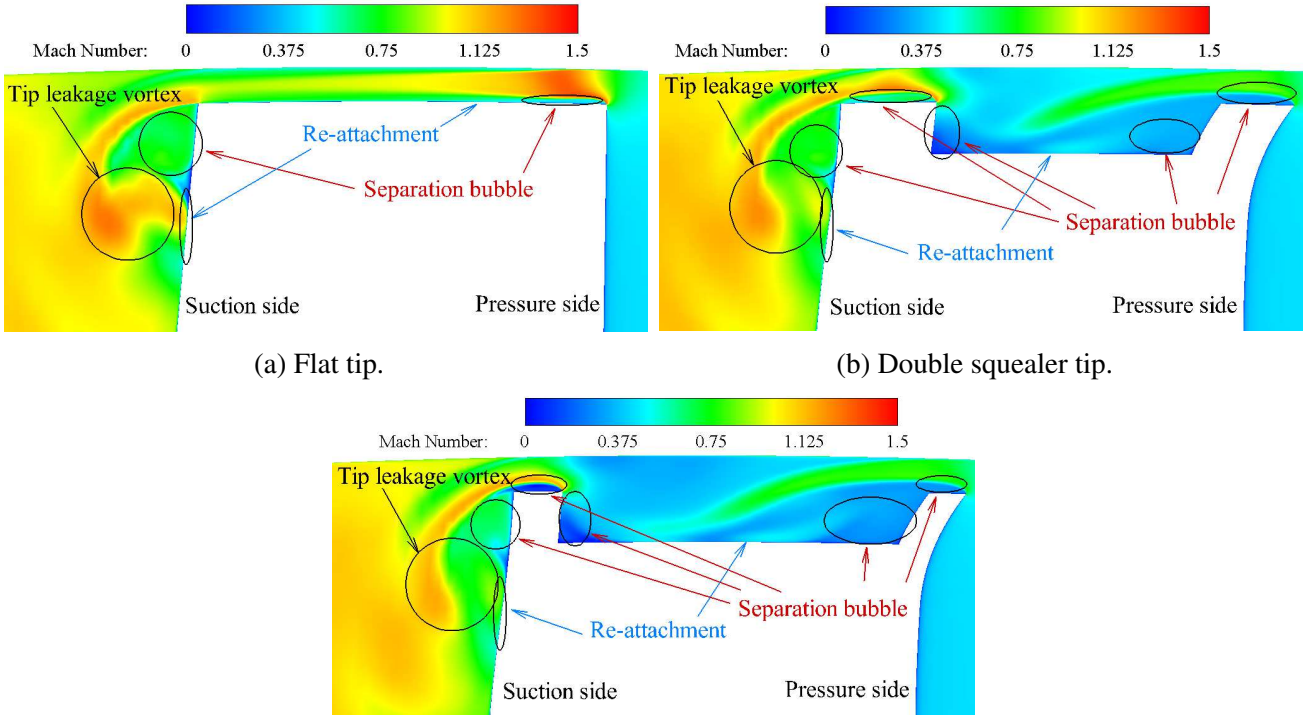

(a) Flat tip. (b) Double squealer tip.

(c) Double thin squealer tip.

Figure 57: Mach number contour at mid-chord for different tip profiles.

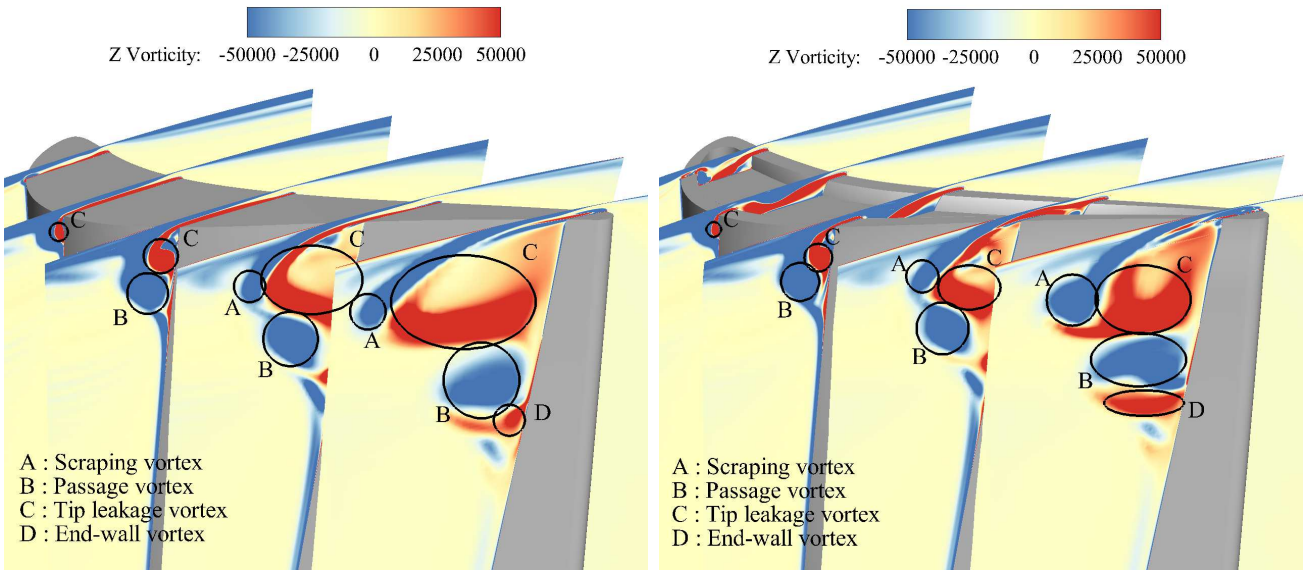

(a) Flat tip. (b) Double squealer tip.

Figure 58: Axial vorticity contour of the tip leakage flow at different axial chord locations z/c_z = 0.15, 0.35, 0.55, 0.75, 0.95.

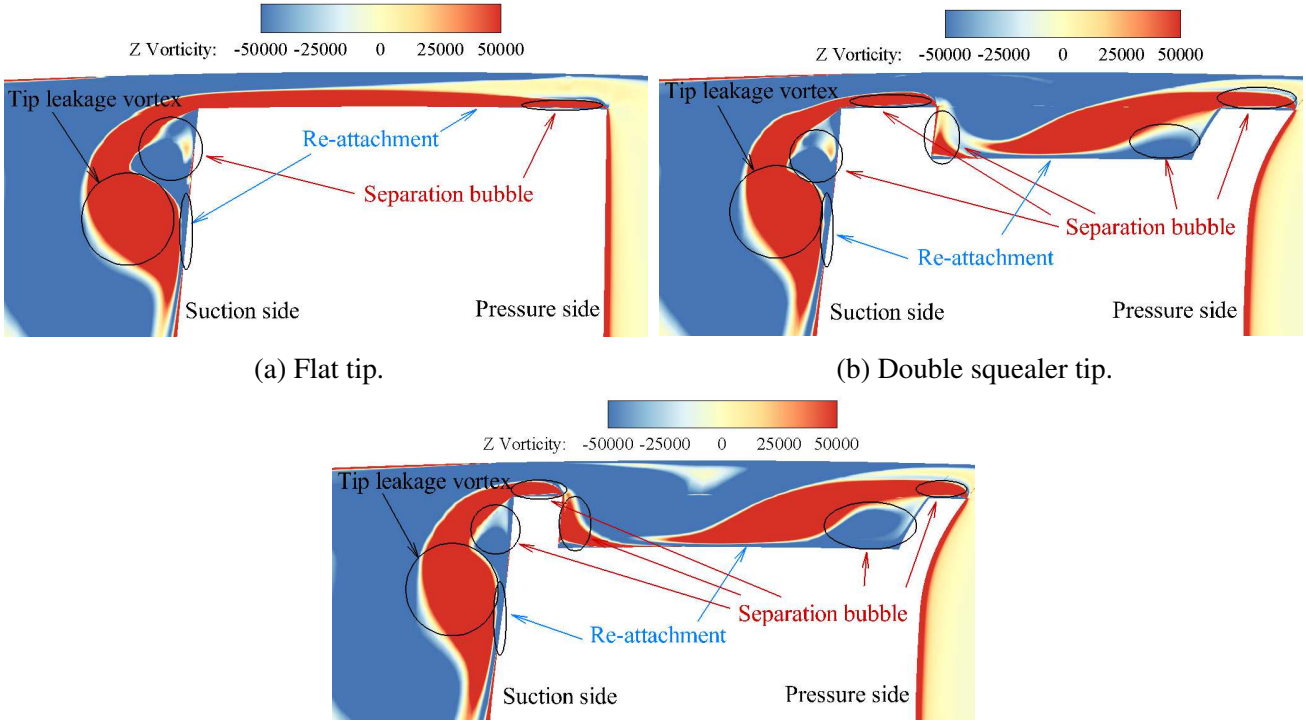

(a) Flat tip. (b) Double squealer tip.

(c) Double thin squealer tip.

Figure 59: Axial vorticity contour at mid-chord for different tip profiles.

Next, it is possible to determine the effect of the cavity on the streamwise pressure distribution and the tip leakage mass flow rate in the near tip region as depicted in Figure 60. The suction side pressure distribution in Figure 60a is slightly shifted towards the trailing edge, the tip leakage vortex formation is delayed and the pressure drop is lightly attenuated. Thereby, the blade loading is lowered for the double squealer profile, which in turn implies a reduction of the tip leakage mass flow rate since the former is the main driver of the flow. This feature is clearly depicted in the Figure 60d where high leakage over a wide region is reduced (e.g. 30% to 70% of the blade in the streamwise direction)

under the blockage effect brought by the squealer. By recalling the evidence of Lee et al. [11], re-attachment regions are associated to maximum mass flow rate. The local peaks found for the double squealer tips are necessarily linked to re-attachment regions but located on the suction side squealer close to the exit. The low mass flow rate range that separates the peaks, represents the area affected by the cavity suction side arm vortex that forces its way out of the gap despite the presence of the squealer. Note that the low mass flow rate range is much broader for the thin squealer tip. Overall, the Figure 60b and 60c highlights an important feature. The double squealer tip tends to regularize and smooth the pressure distribution. This implies that the interaction between the tip leakage vortex and the suction side wall did not vary much, even though the decrease of tip leakage mass flow rate produces a weaker tip leakage vortex that remains closer to blade than that of the flat tip. Thus, the tip configuration does not constitute a crucial factor that can significantly alter the pressure distribution in the near tip region.

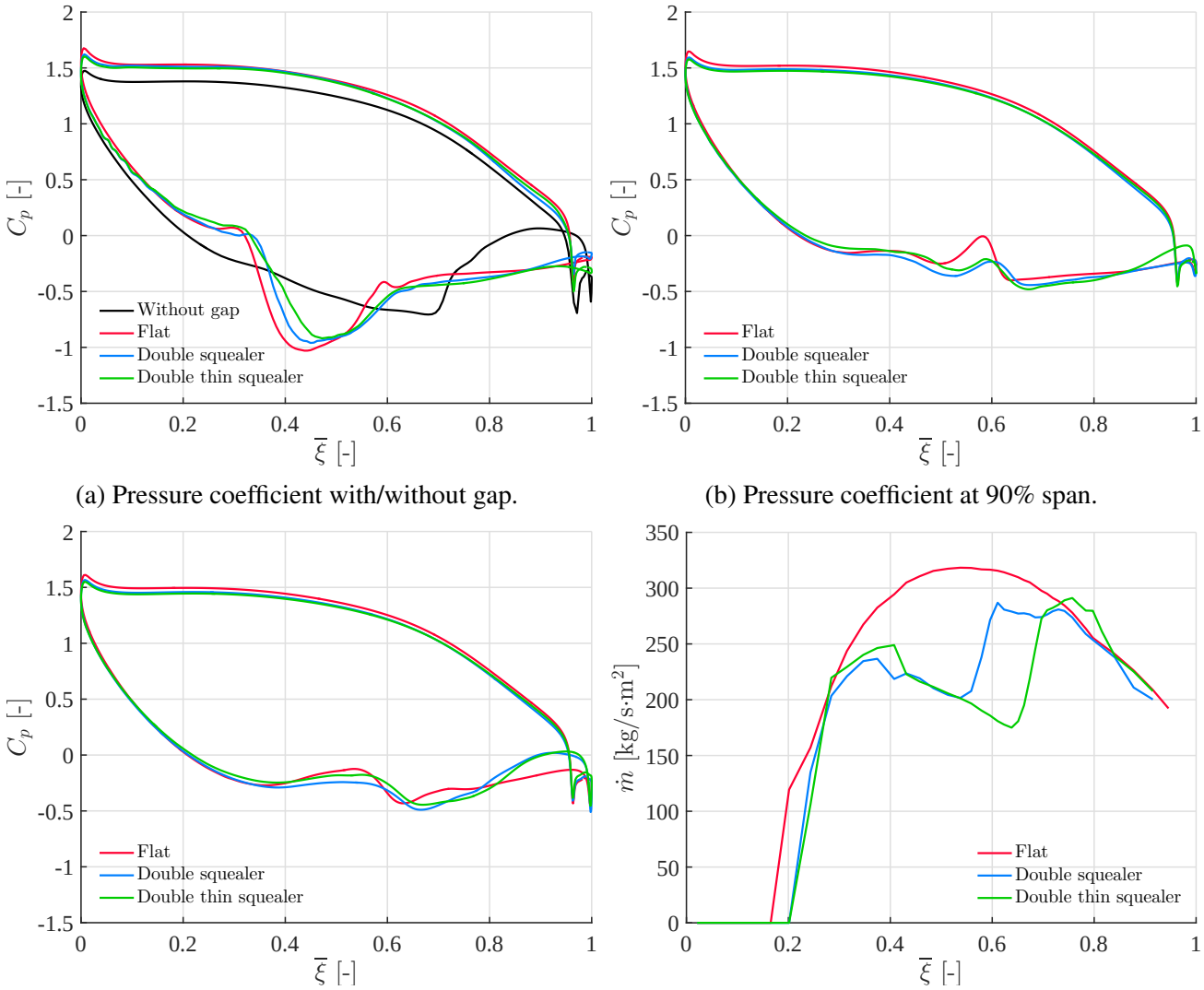

(a) Pressure coefficient with/without gap.

(b) Pressure coefficient at 90% span.

(c) Pressure coefficient at 85% span.

(d) Tip leakage mass flow rate per unit area.

Figure 60: Streamwise distribution of the pressure coefficient and tip leakage mass flow rate for different tip profiles

Lastly, heat transfer phenomenon is investigated by the means of Figure 61 and 62. Again, the adoption of the cavity has got rid of the long re-attachment band of the flat tip, that extends to the trailing edge, although other high heat exchange regions have emerged. The pattern of the squealer horseshoe vortex is still visible and both of its arms spread inward to mix with the cavity vortices. On the other hand, the less evident cavity horseshoe vortex and its arms are determined by the in-

termediary of low heat transfer regions which are simultaneously regions of low velocity magnitude or corner separation bubbles. Unlike the sweet spot observed over the flat tip, a relatively high heat transfer region (entry flow impingement region in Figure 61) is spotted right after cavity horseshoe vortex position. It represents the first significant re-attachment zone near the leading edge. Then, the suction side arm vortex spreads along the suction side edge before reaching the gap exit (area marked by low heat transfer) at approximatively 55% streamwise chord. In the same vein, the pressure side arm vortex spreads along the pressure side edge before reaching the gap exit (again area marked by low heat transfer) at approximatively 90% streamwise chord. Their presence causes re-attachment of the flow over the cavity floor (along the camber line), on the suction and pressure squealers. Note that the thin squealer tip has been able to lower considerably the high heat exchange areas over the squealers and has consecutively deviated the exit position of the cavity vortices by a bit.

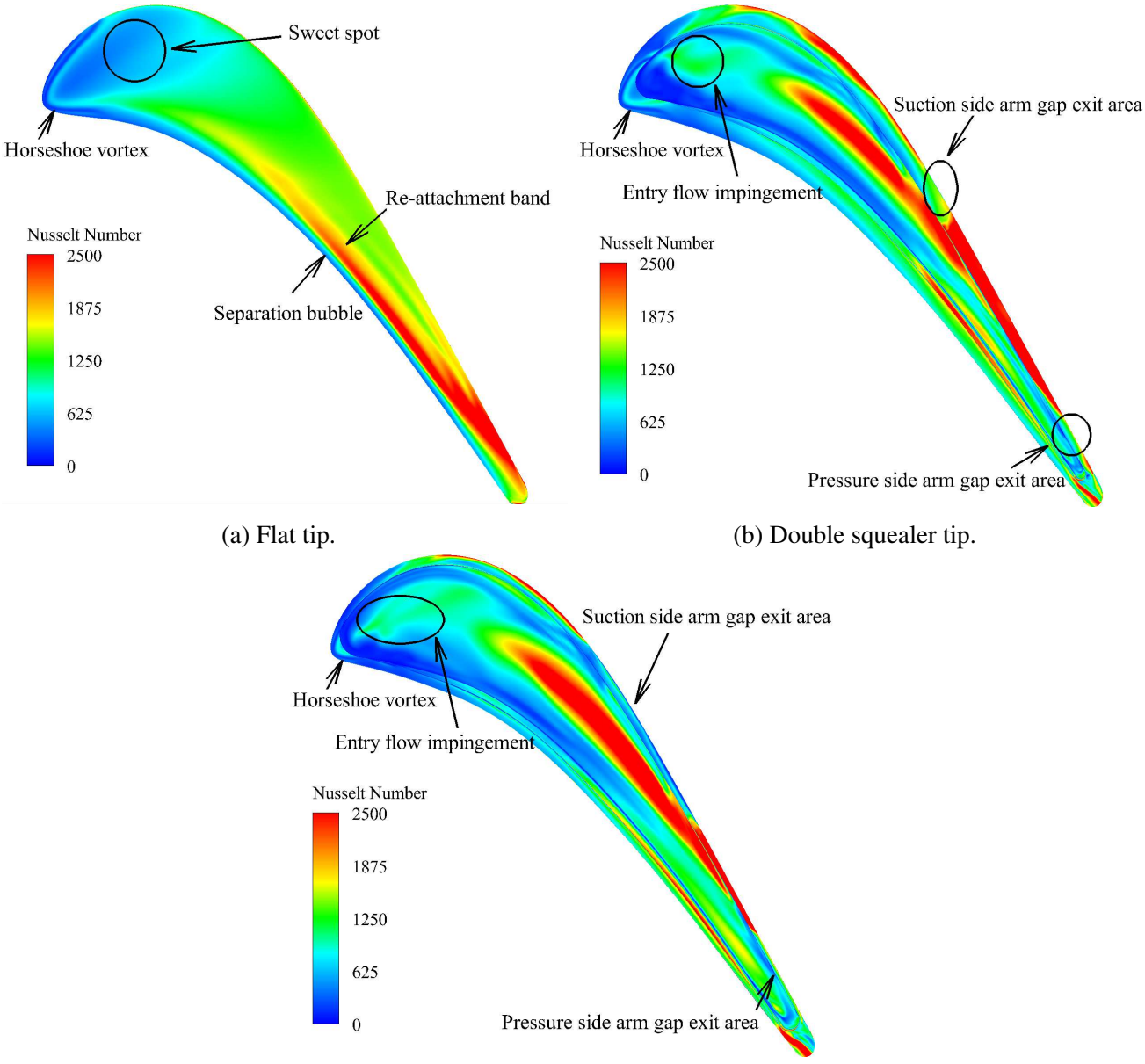

(a) Flat tip.

(b) Double squealer tip.

(c) Double thin squealer tip.

Figure 61: Axial Nusselt number contour over the tip.

Figure 62 reports a reduction of the re-attachment band width on the suction side of the blade in the near tip region. Again, this is due to the weakening of the tip leakage vortex. In the same way, the heat exchange caused by the diffusion and mixing near the trailing edge is also lowered. Note that despite the attenuation of the tip leakage flow, secondary flows in the near tip region remain dominant,

therefore the shock wave is still not able spread upward to the tip. Overall, the results exposed hereby agree with the streamwise distributions of Figure 60, especially the mass flow rate distribution plot which exhibits agreement between the locations of respectively, the re-attachment zone and the mass flow rate peak.

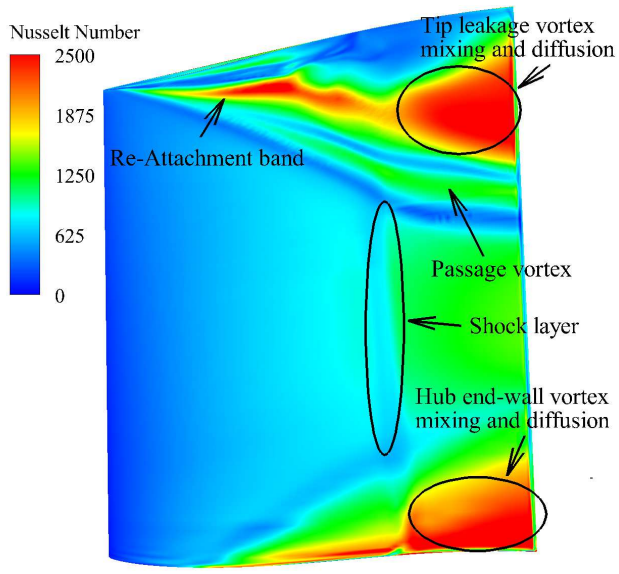

(a) Flat tip.

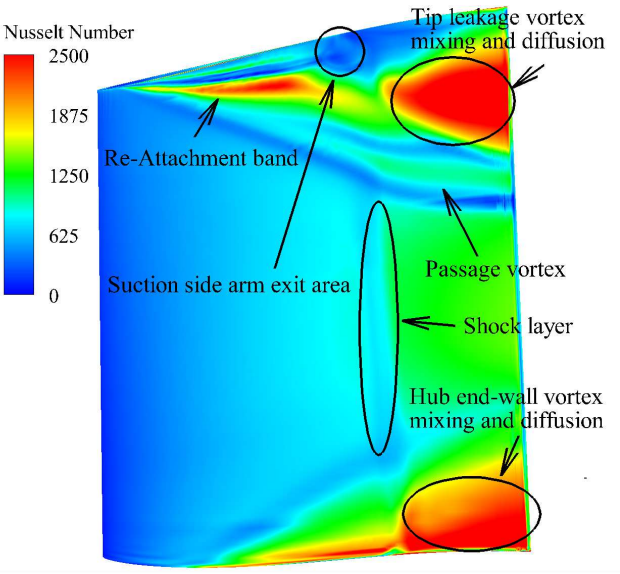

(b) Double squealer tip.

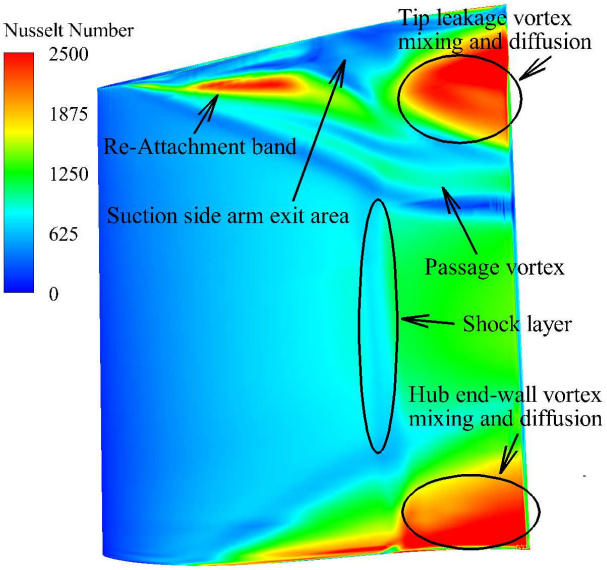

(c) Double thin squealer tip.

Figure 62: Axial Nusselt number contour over suction side of the blade.

To conclude this study, estimation of the tip leakage loss is carried out by the means of Equation 3.35 and the other remaining parameters are gathered in Table 6.

Again, several conclusions can be drawn from this performance analysis :

- Unlike the previous modified blade profile which did not made any difference on the efficiency and increased the average heat transfer. The local enhancement brought to the tip is able to slightly improve the global performance of the turbine stage and considerably reduce the global tip heat transfer.
- Taking into account the considerations made previously about the flow mechanism within the gap, reduction of tip leakage flow is made possible by partially confining the flow inside the

cavity. That is the reason why internal loss has increased whereas external mixing loss has decreased as shown in Table 6. Moreover, halving the squealer thickness in this context is proven to be beneficial since losses and global tip heat transfer were lowered.

Blade	Flat tip	Double squealer tip	Double thin squealer tip
P_w [MW]	1.9	1.917	1.916
T_w [kN.m]	1.649	1.664	1.664
η_t [%]	93.2	93.9	93.9
η_{ts} [%]	85.3	86	86
$T_{t,C}/T_{t,B}$ [-]	0.771	0.769	0.769
$p_{t,C}/p_{t,B}$ [-]	0.374	0.373	0.373
Υ_{int} [%]	16.1	24.2	22.6
Υ_{ext} [%]	83.9	55	50.4
$h_{c,av}$ [W/m^2.K](10^3)	1.336	1.319	1.315

Table 6: Aerothermal performance of the different blade profiles

4 Conclusion

As a conclusion of this study, many important aspects encountered in this work is highlighted and they will serve as guidelines for further possible amelioration.

- Assumptions : It is the most important aspect in this numerical investigation. First, to carry out the global performance analysis of the turbine stage, one has applied a simplified 1D approach to acquire the quantity of interest. The evident complex nature of the turbomachinery flow may render this approach invalid and insufficient if a refined result is sought. Second, the steady solution may not be able to completely reproduce all the features of the flow. This is due to the natural unsteadiness of secondary flows generated by the means of fluid/solid interaction. In general, transient simulation requires much more computational resources, which makes it unaffordable in most cases even though it is highly recommended for the turbomachinery flows. Last, the turbulence models have always subject to debates among many researches. It is true that modelled flow is actually able to predict flows that agree with the real physical flow. However, the lack of experimental results in this context remains problematic since there is no other proof that can justify the reliability of the numerical results.
- Aerothermal enhancement : It has been proven that the adoption of a tip cavity is beneficial for the near tip aerothermal performance since the tip leakage loss and heat transfer have significantly been lowered. Therefore, geometrical modification of the tip profile can clearly influence the features of the tip leakage flow. Until this step, this work has only included four tip geometries for a constant clearance. Other tip profiles depicted in Figure 51 can yet be tested as well. Different clearances can also be defined to assess their impact on this flow. The ultimate improvement that can be brought in the blade design is the inclusion of a cooling system. In the same idea as the tip geometry, many configurations of the cooling holes distributed over the tip, are available. Each of them delivers different effect on the flow, consecutively different performances.

8.4 TTM-Stage blading

8.4.1 TTM-Stage guide vane

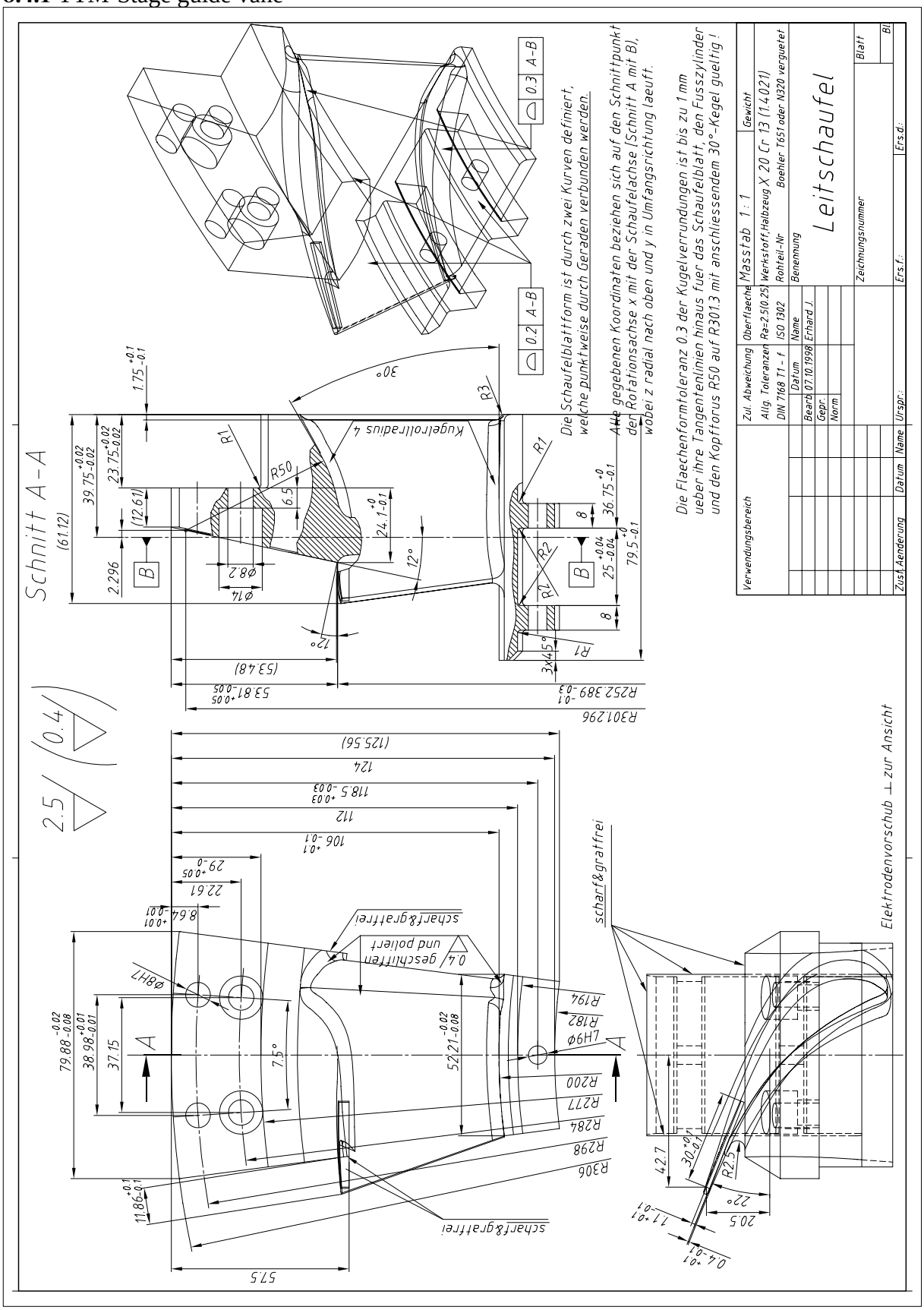

TTM-Stage Vane Sections

Hub	200.000	0.000	Mean	229.000	0.000	Tip	258.000	0.000
pitch =	52.360					pitch =	67.500	
x_inlet =	-58.000					x_inlet =	-58.000	
x_outlet =	34.500					x_outlet =	34.500	
n =	82.000					n =	82.000	
i	x	y				i	x	y
					Midspan			
0	-0.038000	-0.018500		-0.038000	-0.020050		-0.038000	-0.021600
1	-0.037967	-0.018973		-0.037984	-0.020687		-0.038000	-0.022400
2	-0.037478	-0.019946		-0.037439	-0.021973		-0.037400	-0.024000
3	-0.036684	-0.020757		-0.036592	-0.023078		-0.036500	-0.025400
4	-0.035631	-0.021479		-0.035465	-0.024039		-0.035300	-0.026600
5	-0.034097	-0.022433		-0.033798	-0.025316		-0.033500	-0.028200
6	-0.032326	-0.023278		-0.031913	-0.026439		-0.031500	-0.029600
7	-0.030767	-0.023719		-0.030233	-0.027060		-0.029700	-0.030400
8	-0.028969	-0.024064		-0.028284	-0.027532		-0.027600	-0.031000
9	-0.027435	-0.024253		-0.026668	-0.027827		-0.025900	-0.031400
10	-0.025639	-0.024305		-0.024719	-0.027902		-0.023800	-0.031500
11	-0.024105	-0.024242		-0.023052	-0.027871		-0.022000	-0.031500
12	-0.022354	-0.024076		-0.021177	-0.027688		-0.020000	-0.031300
13	-0.020511	-0.023710		-0.019205	-0.027255		-0.017900	-0.030800
14	-0.018644	-0.023151		-0.017222	-0.026575		-0.015800	-0.030000
15	-0.017042	-0.022508		-0.015471	-0.025804		-0.013900	-0.029100
16	-0.015200	-0.021591		-0.013500	-0.024646		-0.011800	-0.027700
17	-0.013619	-0.020639		-0.011809	-0.023419		-0.010000	-0.026200
18	-0.011776	-0.019310		-0.009843	-0.021755		-0.007910	-0.024200
19	-0.009763	-0.017579		-0.007671	-0.019590		-0.005580	-0.021600
20	-0.007919	-0.015756		-0.005694	-0.017278		-0.003470	-0.018800
21	-0.006122	-0.013736		-0.003761	-0.014668		-0.001400	-0.015600
22	-0.004280	-0.011417		-0.001788	-0.011759		0.000703	-0.012100
23	-0.002482	-0.008866		0.000144	-0.008488		0.002770	-0.008110
24	-0.000639	-0.005959		0.002121	-0.004789		0.004880	-0.003620
25	0.000940	-0.003190		0.003810	-0.001262		0.006680	0.000665
26	0.002737	0.000250		0.005744	0.003130		0.008750	0.006010
27	0.004352	0.003467		0.007476	0.007233		0.010600	0.011000
28	0.005726	0.006389		0.008913	0.010894		0.012100	0.015400
29	0.007306	0.009931		0.010603	0.015416		0.013900	0.020900
30	0.008886	0.013613		0.012293	0.020107		0.015700	0.026600
31	0.010297	0.016867		0.013798	0.024184		0.017300	0.031500
32	0.011874	0.020575		0.015487	0.028888		0.019100	0.037200
33	0.013237	0.023755		0.016968	0.032928		0.020700	0.042100
34	0.013379	0.024078		0.017140	0.033339		0.020900	0.042600
35	0.013521	0.024401		0.017261	0.033801		0.021000	0.043200
36	0.013664	0.024724		0.017432	0.034212		0.021200	0.043700
37	0.013806	0.025047		0.017603	0.034623		0.021400	0.044200
38	0.013948	0.025370		0.017774	0.035085		0.021600	0.044800
39	0.014090	0.025693		0.017895	0.035496		0.021700	0.045300
40	0.014032	0.026241		0.017816	0.036120		0.021600	0.046000
41	0.013756	0.026497		0.017428	0.036399		0.021100	0.046300
42	0.013283	0.026480		0.016992	0.036340		0.020700	0.046200
43	0.012824	0.026254		0.016512	0.036077		0.020200	0.045900
44	0.012629	0.025946		0.016315	0.035673		0.020000	0.045400
45	0.012435	0.025638		0.016117	0.035269		0.019800	0.044900
46	0.012240	0.025330		0.015870	0.034915		0.019500	0.044500
47	0.012045	0.025022		0.015673	0.034511		0.019300	0.044000
48	0.011851	0.024714		0.015475	0.034107		0.019100	0.043500
49	0.011656	0.024406		0.015278	0.033703		0.018900	0.043000
50	0.010096	0.021748		0.013598	0.030374		0.017100	0.039000
51	0.008471	0.018965		0.011835	0.026832		0.015200	0.034700
52	0.006714	0.016059		0.010007	0.023180		0.013300	0.030300
53	0.005133	0.013561		0.008316	0.019981		0.011500	0.026400

54	0.003553	0.011239		0.006601	0.017020	0.009650	0.022800
55	0.001993	0.009120		0.004942	0.014310	0.007890	0.019500
56	0.000171	0.006835		0.002996	0.011367	0.005820	0.015900
57	-0.001430	0.004944		0.001275	0.008922	0.003980	0.012900
58	-0.003009	0.003233		-0.000420	0.006716	0.002170	0.010200
59	-0.004852	0.001390		-0.002394	0.004375	0.000064	0.007360
60	-0.006450	-0.000098		-0.004115	0.002456	-0.001780	0.005010
61	-0.008294	-0.001672		-0.006092	0.000444	-0.003890	0.002560
62	-0.009894	-0.002948		-0.007812	-0.001194	-0.005730	0.000560
63	-0.011736	-0.004309		-0.009783	-0.002925	-0.007830	-0.001540
64	-0.013356	-0.005433		-0.011533	-0.004366	-0.009710	-0.003300
65	-0.015200	-0.006623		-0.013500	-0.005866	-0.011800	-0.005110
66	-0.016780	-0.007584		-0.015190	-0.007067	-0.013600	-0.006550
67	-0.018622	-0.008649		-0.017161	-0.008400	-0.015700	-0.008150
68	-0.020320	-0.009596		-0.019010	-0.009568	-0.017700	-0.009540
69	-0.022289	-0.010651		-0.021094	-0.010876	-0.019900	-0.011100
70	-0.024131	-0.011576		-0.023066	-0.011988	-0.022000	-0.012400
71	-0.025487	-0.012213		-0.024543	-0.012756	-0.023600	-0.013300
72	-0.026824	-0.012829		-0.025962	-0.013515	-0.025100	-0.014200
73	-0.028423	-0.013547		-0.027712	-0.014373	-0.027000	-0.015200
74	-0.029759	-0.014122		-0.029129	-0.015061	-0.028500	-0.016000
75	-0.031359	-0.014796		-0.030879	-0.015848	-0.030400	-0.016900
76	-0.032833	-0.015407		-0.032467	-0.016553	-0.032100	-0.017700
77	-0.034294	-0.015962		-0.033997	-0.017181	-0.033700	-0.018400
78	-0.035631	-0.016454		-0.035465	-0.017727	-0.035300	-0.019000
79	-0.036684	-0.016924		-0.036592	-0.018262	-0.036500	-0.019600
80	-0.037497	-0.017481		-0.037449	-0.018891	-0.037400	-0.020300
81	-0.037913	-0.018182		-0.037907	-0.019691	-0.037900	-0.021200
82	-0.038000	-0.018500		-0.038000	-0.020050	-0.038000	-0.021600

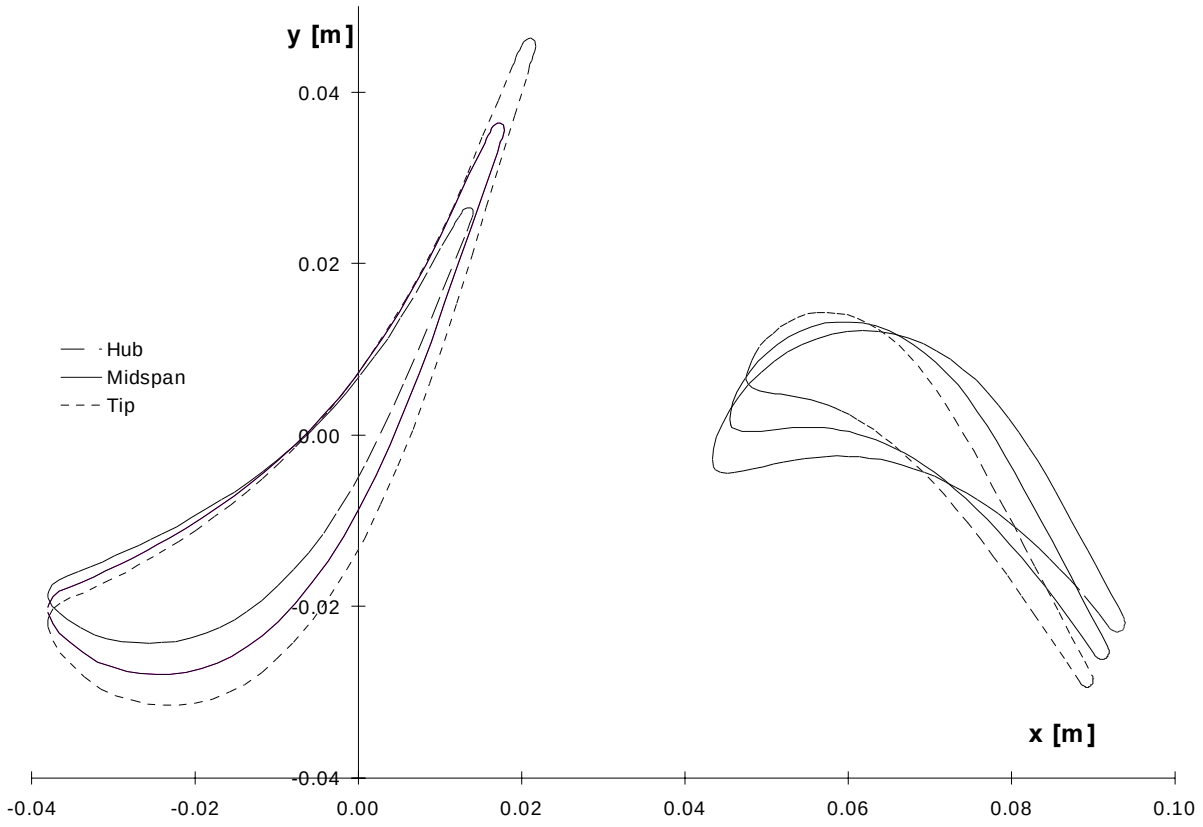

8.4.2 TTM-Stage rotor blade

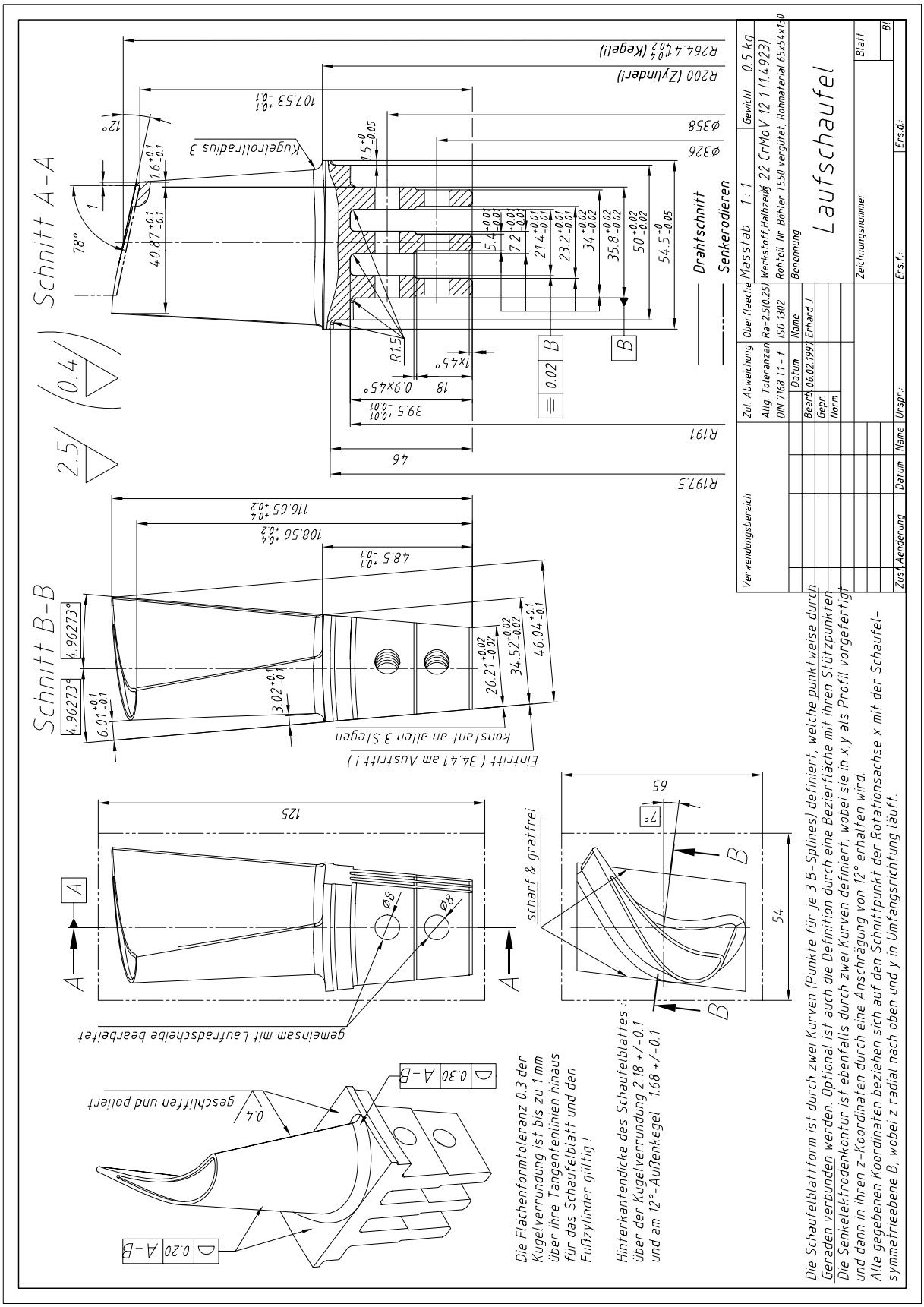

TTM-Stage Blade Sections

Hub	200.000	67.000	Mean	232.789	67.000	Tip	265.577	67.000
pitch =	34.907					pitch =	46.400	
x_inlet =	-32.500					x_inlet =	-32.500	
x_outlet =	55.000					x_outlet =	55.000	
n =	207.000					n =	207.000	
i	x	y Hub			Midspan	i	x	y Tip
0	0.043523	-0.003727		0.045612	0.001141		0.047700	0.006010
2	0.043324	-0.002851		0.045412	0.001819		0.047500	0.006490
4	0.043457	-0.001639		0.045528	0.002736		0.047600	0.007110
6	0.043882	-0.000213		0.045841	0.003819		0.047800	0.007850
8	0.044565	0.001330		0.046382	0.004995		0.048200	0.008660
10	0.045476	0.002911		0.047038	0.006206		0.048600	0.009500
12	0.046586	0.004469		0.047893	0.007435		0.049200	0.010400
14	0.047872	0.005956		0.048936	0.008578		0.050000	0.011200
16	0.049308	0.007333		0.050054	0.009616		0.050800	0.011900
18	0.050873	0.008570		0.051287	0.010585		0.051700	0.012600
20	0.052544	0.009646		0.052622	0.011423		0.052700	0.013200
22	0.054301	0.010543		0.054050	0.012121		0.053800	0.013700
24	0.056122	0.011250		0.055561	0.012675		0.055000	0.014100
26	0.057989	0.011759		0.057095	0.013030		0.056200	0.014300
28	0.059882	0.012067		0.058636	0.013184		0.057390	0.014300
30	0.061782	0.012172		0.060211	0.013186		0.058640	0.014200
32	0.063673	0.012076		0.061792	0.013038		0.059910	0.014000
34	0.065540	0.011782		0.063360	0.012691		0.061180	0.013600
36	0.067369	0.011297		0.064909	0.012149		0.062450	0.013000
38	0.069147	0.010629		0.066423	0.011465		0.063700	0.012300
40	0.070866	0.009789		0.067903	0.010595		0.064940	0.011400
42	0.072517	0.008789		0.069338	0.009594		0.066158	0.010400
44	0.074097	0.007641		0.070726	0.008481		0.067354	0.009320
46	0.075603	0.006363		0.072067	0.007212		0.068530	0.008060
48	0.077035	0.004970		0.073357	0.005825		0.069680	0.006680
50	0.078394	0.003480		0.074612	0.004330		0.070830	0.005180
52	0.079685	0.001909		0.075823	0.002740		0.071960	0.003570
54	0.080913	0.000276		0.076997	0.001068		0.073080	0.001860
56	0.082085	-0.001403		0.078148	-0.000681		0.074210	0.000042
58	0.083208	-0.003112		0.079279	-0.002496		0.075350	-0.001880
60	0.084288	-0.004839		0.080399	-0.004365		0.076510	-0.003890
62	0.085335	-0.006573		0.081517	-0.006287		0.077700	-0.006000
64	0.086354	-0.008305		0.082627	-0.008258		0.078900	-0.008210
66	0.087351	-0.010030		0.083775	-0.010265		0.080200	-0.010500
68	0.088332	-0.011745		0.084916	-0.012323		0.081500	-0.012900
70	0.089301	-0.013450		0.086050	-0.014425		0.082800	-0.015400
72	0.090261	-0.015145		0.087280	-0.016573		0.084300	-0.018000
74	0.091216	-0.016833		0.088508	-0.018767		0.085800	-0.020700
76	0.092167	-0.018516		0.089734	-0.021008		0.087300	-0.023500
78	0.093118	-0.020196		0.091009	-0.023298		0.088900	-0.026400
80	0.093646	-0.021132		0.091723	-0.024566		0.089800	-0.028000
82	0.093734	-0.021324		0.091817	-0.024712		0.089900	-0.028100
84	0.093799	-0.021509		0.091849	-0.024905		0.089900	-0.028300
86	0.093841	-0.021687		0.091871	-0.025044		0.089900	-0.028400
88	0.093863	-0.021857		0.091882	-0.025179		0.089900	-0.028500
90	0.093866	-0.022018		0.091883	-0.025309		0.089900	-0.028600
92	0.093850	-0.022170		0.091875	-0.025485		0.089900	-0.028800
94	0.093817	-0.022310		0.091858	-0.025605		0.089900	-0.028900
96	0.093768	-0.022440		0.091834	-0.025720		0.089900	-0.029000
98	0.093704	-0.022557		0.091752	-0.025828		0.089800	-0.029100
100	0.093626	-0.022661		0.091663	-0.025880		0.089700	-0.029100
102	0.093536	-0.022751		0.091618	-0.025975		0.089700	-0.029200
104	0.093435	-0.022826		0.091518	-0.026063		0.089600	-0.029300
106	0.093324	-0.022886		0.091412	-0.026093		0.089500	-0.029300

108	0.093204	-0.022929		0.091302	-0.026165	0.089400	-0.029400
110	0.093076	-0.022955		0.091188	-0.026178	0.089300	-0.029400
112	0.092942	-0.022963		0.091071	-0.026182	0.089200	-0.029400
114	0.092803	-0.022953		0.090951	-0.026176	0.089100	-0.029400
116	0.092660	-0.022922		0.090830	-0.026111	0.089000	-0.029300
118	0.092513	-0.022871		0.090707	-0.026086	0.088900	-0.029300
120	0.092365	-0.022799		0.090583	-0.025999	0.088800	-0.029200
122	0.092217	-0.022704		0.090458	-0.025952	0.088700	-0.029200
124	0.092069	-0.022587		0.090335	-0.025843	0.088600	-0.029100
126	0.091924	-0.022445		0.090162	-0.025723	0.088400	-0.029000
128	0.091781	-0.022279		0.090040	-0.025540	0.088300	-0.028800
130	0.090627	-0.020850		0.088514	-0.023475	0.086400	-0.026100
134	0.088271	-0.018122		0.085535	-0.019561	0.082800	-0.021000
136	0.087070	-0.016827		0.084085	-0.017714	0.081100	-0.018600
138	0.085856	-0.015580		0.082628	-0.015940	0.079400	-0.016300
140	0.084630	-0.014383		0.081215	-0.014292	0.077800	-0.014200
142	0.083393	-0.013238		0.079807	-0.012719	0.076220	-0.012200
144	0.082146	-0.012145		0.078423	-0.011223	0.074700	-0.010300
146	0.080890	-0.011106		0.077055	-0.009863	0.073220	-0.008620
148	0.079625	-0.010122		0.075707	-0.008576	0.071790	-0.007030
150	0.078352	-0.009195		0.074376	-0.007382	0.070400	-0.005570
152	0.077071	-0.008324		0.073066	-0.006282	0.069060	-0.004240
154	0.075785	-0.007511		0.071772	-0.005275	0.067760	-0.003040
156	0.074492	-0.006756		0.070500	-0.004353	0.066508	-0.001950
158	0.073193	-0.006061		0.069246	-0.003524	0.065300	-0.000988
160	0.071889	-0.005425		0.068019	-0.002778	0.064150	-0.000131
162	0.070580	-0.004850		0.066815	-0.002113	0.063050	0.000624
164	0.069267	-0.004336		0.065634	-0.001528	0.062000	0.001280
166	0.067950	-0.003884		0.064480	-0.001012	0.061010	0.001860
168	0.066630	-0.003493		0.063350	-0.000566	0.060070	0.002360
170	0.065306	-0.003164		0.062243	-0.000192	0.059180	0.002780
172	0.063979	-0.002897		0.061159	0.000121	0.058340	0.003140
174	0.062650	-0.002693		0.060100	0.000379	0.057550	0.003450
176	0.061318	-0.002550		0.059059	0.000580	0.056800	0.003710
178	0.059986	-0.002469		0.058043	0.000730	0.056100	0.003930
180	0.058654	-0.002449		0.057027	0.000831	0.055400	0.004110
182	0.057322	-0.002487		0.056061	0.000886	0.054800	0.004260
184	0.055995	-0.002582		0.055047	0.000904	0.054100	0.004390
186	0.054673	-0.002729		0.054086	0.000881	0.053500	0.004490
188	0.053360	-0.002923		0.053130	0.000829	0.052900	0.004580
190	0.052063	-0.003156		0.052181	0.000752	0.052300	0.004660
192	0.050786	-0.003417		0.051243	0.000656	0.051700	0.004730
194	0.049541	-0.003693		0.050271	0.000558	0.051000	0.004810
196	0.048339	-0.003964		0.049369	0.000463	0.050400	0.004890
198	0.047196	-0.004204		0.048498	0.000393	0.049800	0.004990
200	0.046134	-0.004379		0.047667	0.000371	0.049200	0.005120
202	0.045179	-0.004446		0.046940	0.000427	0.048700	0.005300
204	0.044369	-0.004347		0.046284	0.000591	0.048200	0.005530
206	0.043746	-0.004012		0.045773	0.000909	0.047800	0.005830
207	0.043523	-0.003727		0.045612	0.001141	0.047700	0.006010

References

[1] C. Hirsch, *Numerical Computation of Internal & External Flows Vol. 1 : Fundamentals of Computational Fluid Dynamics*, Butterworth-Heinemann, 2nd Edition, 2007.

[2] Y.A. Cengel & J.M. Cimbala, *Fluid Mechanics : Fundamentals and Applications*, McGraw-Hill, 3rd Edition, 2014.

[3] J.N. Reddy & D.K. Gartling, *The Finite Element Method in Heat Transfer and Fluid Dynamics*, CRC Press, 3rd Edition, 2010.

[4] P.A. Durbin & B.A. Pettersson-Reif, *Statistical Theory and Modelling for Turbulent Flow*, Wiley, 2nd Edition, 2011.

[5] E.A. Baskharone, *Principles of Turbomachinery in Air-Breathing Engines*, Cambridge University Press, 1st Edition, 2006.

[6] A.A. Townsend, *The Structure of Turbulent Shear Flow*, Cambridge University Press, 1976.

[7] S.A. Korpela, *Principles of Turbomachinery*, Wiley, 1st Edition, 2011.

[8] B. Lakshminarayana, *Fluid Dynamics and Heat Transfer of Turbomachinery*, Wiley, 1st Edition, 1996.

[9] F. Montomoli, M. Carnevale, A. D'Ammaro, M. Massini & S. Salvadori, *Uncertainty Quantification in Computational Fluid Dynamics and Aircraft Engines*, Springer, 1st Edition, 2015.

[10] J. Erhard, *Design, Construction and Commissioning of a Transonic Test-Turbine Facility* , Ph.D. Thesis, Graz University of Technology, Austria, 2000.

[11] S.W. Lee, H.S. Moon & S.E. Lee, *Tip Gap Height Effects on Flow Structure and Heat/Mass Transfer over Plane Tip of a High-Turning Turbine Rotor Blade* , International Journal of Heat and Fluid Flow Vol. 30, p. 198-210, 2009.

[12] R.S. Bunker, *A Review of Turbine Blade Tip Heat Transfer* , General Electric Corporate Research & Development Center, U.S.A., 2000.

[13] R.S. Bunker, *Axial Turbine Blade Tips: Function, Design and Durability* , Journal of Propulsion and Power Vol. 22, p. 271-285, 2006.

[14] R.S. Bunker, G.A. Ledezma & J. Allen, *An Experimental and Numerical Investigation into the Effects of Squealer Blade Tip Modifications on Aerodynamic Performance*, General Electric Corporate Research & Development Center, U.S.A., 2013.

[15] R.S. Bunker, *Blade Tip Aerodynamics and Heat Transfer*, General Electric Corporate Research & AIAA, U.S.A., 2014.

[16] R.S. Bunker & J.C. Bailey, *Blade Tip Heat Transfer and Flow with Chordwise Sealing Strips*, Pacific Center of Thermal Fluids Engineering, U.S.A., 2000.

[17] J.P. Bindon, *Pressure Distributions in the Tip Clearance Region of an Unshrouded Axial Turbine as Affecting the Problem of Tip Burnout*, International Gas Turbine Conference ASME, U.S.A., 1987.

[18] T.C. Booth, *Tip Clearance Effects in Axial Turbomachines: Importance of Tip Clearance Flows in Turbine Design*, Von Karman Inst. Lecture Series,, Belgium., 1985.

[19] Z. Wei, W. Qiao & P. Shi. *Tip-Leakage Flow Loss Reduction in a Two-stage Turbine using Axisymmetric-Casing Contouring*, Chinese Journal of Aeronautics Vol. 27, p. 1111-1121, 2014.

[20] J.D. Denton, *Loss Mechanisms in Turbomachines*, Journal of Turbomachinery Vol. 115, 1993.

[21] J.S. Kwak & J.C. Han, *Heat Transfer Coefficient on the Squealer Tip and near Squealer Tip Regions of a Gas Turbine Blade*, Turbine Heat Transfer Laboratory, Texas A&M University, U.S.A., 2002.

[22] Gm.S. Azad & J.C. Han, *Heat Transfer and Flow on Squealer Tip of a Gas Turbine Blade*, Turbine Heat Transfer Laboratory, Texas A&M University, U.S.A., 2000.

[23] H. Yang, H.C. Chen & J.C. Han, *Turbine Rotor with Various Tip Configurations Flow and Heat Transfer Prediction*, Journal of Thermophysics and Heat Transfer, Vol. 20, p. 80-91, 2006.

[24] J.S. Kwak, J.C. Han et al., *Heat Transfer Coefficients on the Squealer Tip and Near-Tip Regions of a Gas Turbine Blade With Single or Double Squealer*, Journal of Turbomachinery, Vol. 125, 2003.

[25] P. Bradshaw, *Turbulence Modelling with Application to Turbomachinery*, Progress Aerospace Sciences Vol. 32, p. 575-624 1996.

[26] B. Diskin, J.L. Thomas, C.L. Rumsey & A. Schwoppe, *Grid Convergence for Turbulent Flows*, NASA Langley Research Center, American Institute of Aeronautics and Astronautics, U.S.A., 2014.

[27] F.R. Menter, *Two-equation eddy-viscosity turbulence models for engineering applications*, AIAA Journal, Vol. 32, p. 269-289 1994.

[28] S.K. Krishnababu, *Aerothermal Investigations of Tip Leakage Flow in Axial Flow Turbines—Part 1 : Effect of Tip Geometry and Tip Clearance Gap*, Journal of Turbomachinery, Vol. 131, 2009.

[29] S.K. Krishnababu & H.P. Hodson, *Aerothermal Investigations of Tip Leakage Flow in a Film Cooled Industrial Turbine Rotor*, Journal of Turbomachinery, Vol. 132, 2010.

[30] S. Lavagnoli, *Analysis of the Heat Transfer Driving Parameters in Tight Rotor Blade Tip Clearances*, Journal of Heat Transfer, Vol. 138, 2016.

[31] P.J. Roache & K. Ghia and F. White, *Editorial Policy Statement on the Control of Numerical Accuracy*, ASME Journal of Fluids Engineering, Vol. 108, 1986.

[32] D.G. Wilcox, *Turbulence Modelling for CFD*, DCW Industries, Inc., 1993.

[33] S.J. Kline, B.J. Cantwell & G.M. Lilley, *Complex Turbulent Flows Vol. 1, Vol. 2, Vol. 3*, Standford University Press, 1982.

[34] J.G. Marvin, *Turbulence Modelling for Computational Aerodynamics*, AIAA Journal, Vol. 21, p. 941, 1983.

[35] B. Lakshminarayana, *Turbulence Modelling for Complex Shear Flows*, AIAA Journal, Vol. 24, p. 1900-1917, 1986.

[36] W. Rodi, *Examples of Turbulence Models for Incompressible Flows*, AIAA Journal, Vol. 20, p. 872, 1982.

[37] F.R. Menter, *Two-Equation Eddy-Viscosity Turbulence Models for Engineering Applications*, AIAA Journal, Vol. 32, p. 1598-1605, 1994.

[38] F.R. Menter, *Zonal Two Equation k-omega Turbulence Models for Aerodynamic Flows*, AIAA Paper 93-2906, 1993.

[39] D. Yang, X. Yu & Z. Feng, *Investigation of Leakage Flow and Heat Transfer in a Gas Turbine Blade Tip with Emphasis on the Effect on Rotation*, Journal of Turbomachinery, Vol. 132, 2010.

[40] C. Zhou & H. Hodson, *Squealer Geometry Effects on Aerothermal Performance of Tip-Leakage Flow of Cavity Tips*, Journal of Propulsion and Power, Vol. 28 2012.

[41] Q. Zhang et al., *Transonic Turbine Blade Tip Aerothermal Performance With Different Tip Gaps—Part I: Tip Heat Transfer*, Journal of Turbomachinery , Vol. 133 2011.

[42] F. Mumic et al., *On Prediction of Tip Leakage Flow and Heat Transfer in Gas Turbines* ASME Paper No. 2004-GT-53448, 2004.